Ionization-induced fragmentation dynamics of isolated complex biomolecules

Gonzalez Magana, Olmo

Citation for published version (APA):
Gonzalez Magana, O. (2013). Ionization-induced fragmentation dynamics of isolated complex biomolecules. [S.l.]: [S.n.].

Ionization-induced fragmentation dynamics of isolated complex biomolecules

Olmo González Magaña

Front cover: *Synchrotron light produced by BESSY II undulator U49.*
Photo: Olmo González Magaña.
Back cover: *Photographic collage by Olmo González Magaña.*

Syncrotron radiation was provided by the Helmholtz-Zentrum Berlin - Electron storage ring BESSY II (Berlin, Germany) and Max-Lab (Lund Sweden). The research has received additional support from the European Community's Seventh Framework Programme (FP7) and the COST Action MP1002 (Nano-IBCT).

PRINTED BY: *Ipskamp Drukkers*, Enschede, November 2013

RIJKSUNIVERSITEIT GRONINGEN

Ionization-induced fragmentation dynamics of isolated complex biomolecules

Proefschrift

ter verkrijging van het doctoraat in de
Wiskunde en Natuurwetenschappen
aan de Rijksuniversiteit Groningen
op gezag van de
Rector Magnificus, dr. E. Sterken,
in het openbaar te verdedigen op
vrijdag 29 november 2013
om 12.45 uur

door

Olmo González Magaña

geboren op 26 mei 1981
te Guadalajara, Mexico

Promotor: Prof. dr. ir. R. Hoekstra

Copromotor: Dr. T. Schlathölter

Beoordelingscommissie: Prof. dr. S. Brøndsted Nielsen
Prof. dr. A.M. van Oijen
Prof. dr. W.M.G. Ubachs

ISBN: 978-90-367-6582-4 Printed version
ISBN: 978-90-367-6583-1 Electronic version

Contents

Chapter 1

Introduction

It is nowadays well established that the bulk of biological radiation damage can be attributed to DNA damage. As a consequence, intense research has focused on this subject, coming from all possible angles [1]. On the most complex side, radiobiological *in vivo* and *in vitro* experiments are performed to investigate the response of life upon DNA damage. Conclusions from such studies can often be employed in a straightforward way to answer questions from radiotherapy or radiation protection. From such studies it remains difficult, if not impossible, to obtain detailed information on the underlying physicochemical processes occurring on the molecular level and on femtosecond timescales.

To some extent, such questions can be tackled by investigation of radiation action on mesoscopic model systems, such as for instance plasmid DNA in aqueous solution. From such experiments it is known that there are two general types of interactions that cause DNA damage: Direct damage is caused by interactions of particles with the DNA molecule itself whereas indirect damaged is produced by radiation induced radicals in the environment of DNA [2, 3]. After diffusion, these radicals, for instance from water radiolysis, chemically damage the DNA.

About 10 years ago, a third field of research focusing on the molecular mechanisms underlying biological radiation damage started to flourish. Originally, the focus of this research was the interaction of ionizing radiation and its secondary particles such as low energy electrons, with isolated gas-phase molecules of biological interest. Such studies can clarify fundamental questions on radiation action upon biomolecules because the whole arsenal of atomic and molecular physics experimental techniques and theory can be applied. Studies of biomolecules in the gas phase are also suitable to bring information regarding the intrinsically properties of the molecules. For example, electron densities, ionization energies, electron affinities, dipole moments, bond strengths, internal vibrational redistribution, fragmentation cross sections and others. However, the field is sometimes criticized for being of limited relevance for the understanding of realistic radiobiological processes. Gas-phase studies of/on isolated biomolecular systems e.g. lack the effect of an aqueous medium. To bridge the gap between gas-phase studies and radiobiology, currently many groups make efforts to move towards the investigation of biologically more realistic systems in the gas phase.

The work presented in this thesis represents an experimental step towards such more realistic systems, because instead of the smallest building blocks of DNA, oligonucleotides as well as peptides and proteins will be investigated. In particular, studies on the action of energetic photons and keV ions will be reported.

1.1 Biological radiation damage

The study of radiation action on biological tissue started at the end of the 19th century, with the discovery of X-rays by Röntgen in 1895 [4]. In the following year, Becquerel observed a similar type of radiation emitted from uranium ores [5] and in 1898, the Curies discovered the elements polonium and radium and coined the term “radioactivity" [6, 7]. They share the Nobel Prize in Physics 1903 [8, 9]. Immediately, the medical community recognized the therapeutic power of this new type of radiation, as well as its health hazards. Already in 1896, Despeignes administered X-ray treatment to a patient suffering from stomach cancer [10] while e.g. Stevens reported on injurious skin effects of X-rays [11].

Relatively soon the immediate effects of high doses of ionizing radiation upon mammalian bodies were well studied. The dose regimes, in which bone marrow, gastrointestinal and neurovascular syndromes are observed, respectively, range from less than 1 Gy for the first, up to more than 30 Gy for the last. These syndromes become manifest hours after irradiation and often have a high mortality rate on the next days to weeks [12]. Note, that even for incidents such as disasters at nuclear power plants, accumulation of the highest doses is exceptional. Low doses, on the other hand, are known to potentially cause medical conditions with long latency, such as cancer or organ failure, and can have severe hereditary effects. Because of the stochastic nature of the radiation effect and the long latency before a biological affect becomes noticeable, the low dose regime is notoriously difficult to investigate.

The rapidly increasing application of ionizing radiation in medicine, industry and research triggered the development of the field of radiation protection and risk assessment.

1.1.1 Ionizing radiation

The Earth biosphere is exposed to ionizing radiation from natural sources such as cosmic rays or nuclear decays, and for artificial sources such as medical or industrial facilities. As the name suggests, the term ionizing radiation embraces those types of radiation which can potentially transfer the necessary amount of energy to remove one or more electrons from an atomic or molecular system. There are two classes of radiation to be mentioned in this context: a) particles, such as electrons, positrons, protons, neutrons, alpha–particles, heavy ions, and others and b) electromagnetic radiation, ranging from the ultraviolet, via X-rays to hard gammas.

Within a biological tissue, the removal of electrons triggers a complex sequence of events, both on the molecular and cellular level, that can lead to permanent damage of the biological functions of the cell, inhibit its ability to reproduce or even result in the death of the cell [1]. Live on earth has developed in the presence of ionizing radiation from natural sources and biological cells have therefore developed efficient repair mechanisms, to cope with radiation induced damage. Most dangerous in the low-dose regime are neither irreparable damages, leading to cell death, nor successfully repaired damages. The biggest risk rather comes from mutation of the DNA sequence, often after an unsuccessful repair, which can lead to the development of cancer cells. The actual amount of damage inflicted to an organism depends on several factors, such as the specific type of cells that constitute the irradiated tissue and the absorbed dose. Furthermore, the damage strongly depends on the type of ionizing radiation. For this reason, the equivalent dose, measured in units of Sievert (Sv), has been introduced and is used to estimate the health risk of radiation exposure.

Because of the time that is needed it for the repair mechanisms to act, there is a clear difference in cellular survival and fitness when the dose is received at once or over a longer period of time (either continuously distributed or in many fractions). In the first case, a short exposure to relative high dose leads to radiation poison symptoms, which can already set in at an estimated value of 400 mSv. On the other hand, a total dose of 1 Sv per year merely increases the cancer risk by 5.5% [13].

In general, the amount of equivalent dose that the average population receives per year is much lower and mainly due to natural sources. For the Netherlands, with a total dose of 2.4 mSv/y and a natural component of 1.6 mSv/y, particularly low values are observed [14]. In comparison the lowest equivalent dose shown to increase cancer risk is 100 mSv. The equivalent dose limit due to occupational activities in the Netherlands is regulated by law to a maximal value of 20 mSv/year for exposed workers and 1 mSv/year for general members of the public.

1.1.2 Radiotherapy

The aim of radiotherapy treatment is to inflict maximum damage to the tumour tissue with the ultimated goal of eradication of all malignous cells. The maximum dose that can be administered, however, is limited by the undesired effect on surrounding healthy tissue. The ratio between therapeutic effect on the tumours and accompanying negative effects on the healthy tissue is known as therapeutic index or therapeutic ratio and clearly needs to be maximized. Fig. 1.1 depicts the amount of deposited dose as function of travel distance through water for different types of ionizing radiation. Energetic photons are sparsely ionizing and therefore, water is relatively transparent. The dose distribution curve is flat and the dose is thus deposited almost evenly distributed along the track through the medium. At present, radiotherapy most often relies on the use of energetic photons. MeV electrons are a heavily used alternat-

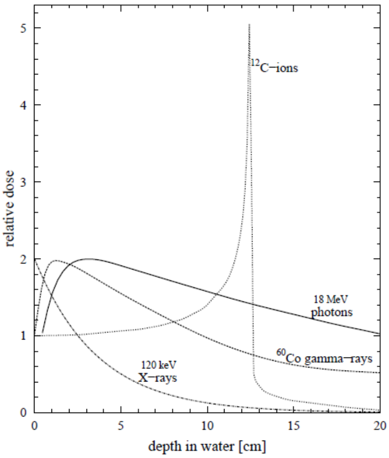

Figure 1.1: *Deposited dose along a water target. Courtesy of D. Schardt, GSI.*

ive, but only suited for relatively shallow seated tumors. Swift heavy ions, on the other hand, are densely ionizing. They are rapidly slowed down in the medium and the dose deposited along the track stays relatively constant over the entire so-called plateau-region. When the ions are slowed down to velocities comparable to molecular valence electron velocities, the interaction strength and thus the energy transfer increases until the ions are stopped. At a certain primary kinetic energy dependent depth, the deposited dose increases sharply into a localized and narrow peak, which is called the Bragg peak. Beyond the Bragg peak, the dose is virtually zero. This dose distribution allows for a much better dose localization in the tumor tissue and leads to a superior therapeutic ratio. Radiotherapy with heavy ions, such protons or carbon ions, is now a reality, and an increasing number of facilities is available for patients in Europe and all over the world (an updated list is available in Ref. [15]).

This thesis focuses on two very relevant types of ionizing radiation, namely energetic photons and heavy ions. The employed photon energies and the heavy ion kinetic energies, though, are markedly lower than those applied in therapy. The reasons are on the one hand practical: the fact that hard X-rays or γ-rays are sparsely ionizing already implies very small interaction cross sections with biomolecules which would render experiments with the currently available experimental techniques extremely challenging. The cross-sections are much larger for the soft X-ray and vacuum ultraviolet (VUV) regime. In heavy ion therapy, initial kinetic energies of hundreds of MeV up to GeV are used. However, the interactions most relevant for tumor therapy occur in the Bragg peak region, where ion kinetic energies are already in the MeV range and below. The keV range, investigated in this thesis, correspond to interactions occurring at the very end of the Bragg peak.

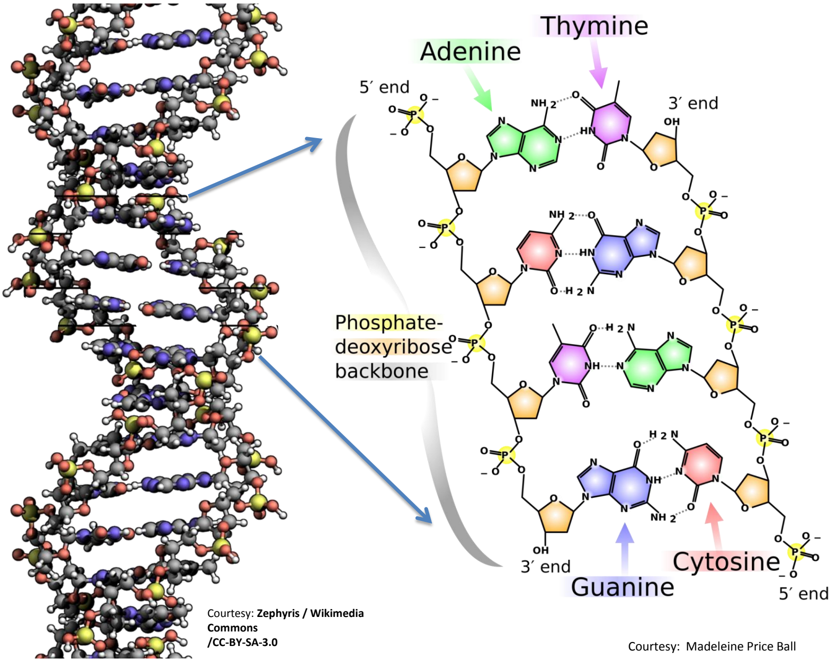

Courtesy: **Zephyris / Wikimedia Commons /CC-BY-SA-3.0**

Courtesy: Madeleine Price Ball

Figure 1.2: *The double strand helix structure of the DNA. Inset: the chemical structure*

1.1.3 DNA

The deoxyribonucleic acid (DNA) is a macromolecule that carries the genetic information of all known living organisms in earth. DNA was first isolated in 1869 by Friedrich Miescher, who named it “nuclein" [16]. In the later 1870s and 1880s, the individual nucleobases of DNA were first isolated by Albrecht Kossel [17]. The term “nucleic acid" was introduced 1889 by Richard Altmann. However, only in 1943 a milestone in biology took place with the discovery that DNA, and not proteins, carries the information of inheritance [18]. In 1953, the double helical structure of the DNA molecule was suggested by Watson and Crick [19]. The double helix model was backed up by high quality X-ray diffraction images taken by Rosalind Franklin and Raymond Gosling, who also described key structural features of DNA [20] and on the results of Maurice Wilkins [21].

DNA consists of two long strands of nucleotides, each coiled around the same axis in an anti-parallel helical structure as shown in Fig. 1.2. The nucleotides are composed of a phosphate group, a sugar molecule (deoxyribose), and one of the four nucleobases adenine (A), cytosine (C), guanine (G) or thymine (T). The bases are on the inside of the helix and the phosphates on the outsides. The sugar and the phosphate groups form the backbone of the strand. The nucleobases are placed perpendicular to the fibre axis of the helix [19]. They are linked in pairs by hydrogen bonds, with a single base from one strand bonded to a single base from the other strand. The pairs are called Watson-Crick and can only be formed by hydrogen bonds between adenine and thymine or between guanine and cytosine. As a consequence, the sequence of bases on one strand is complementary to the other one. Furthermore, the restrictive pairing rules allow for a straightforward duplication process. When the hydrogen bonds are broken and the strands are separated, a reconstructed new partner strand will automatically follow the sequence of the old strand, resulting in two identically new DNA molecules.

Because it is well established, that DNA damage is the most common reason for long term radiation effects on living organisms, gas-phase studies on biomolecular radiation damage have most often focused on DNA building blocks such as nucleobases or deoxyribose. In this thesis, radiation action upon the much larger oligonucleotide GCAT will be investigated in the gas phase for the first time, as a proof of principle study. This study will help to answer some urging questions in the field: *In how far is it possible to approximate photon and ion induced damage to DNA by the respective damage to DNA building blocks? What is the role of genuine chemical effects such as proton migration and charge migration?*

1.2 Peptides

Even though DNA damage is crucial for radiation effect on living organisms, proteins play an important role. Not only are proteins responsible for almost all metabolic processes occurring in living cells. Proteins for instance play crucial role in the cell nucleus where DNA is wound tightly around protein spools, the so-called histones, which are also involved in gene-regulation. It is the action of histones, that brings DNA into the compact supercoiled form it has in the cell-nucleus. Histones and other proteins play an important role in biological radiation damage, because they can protect DNA against indirect [2] and to a smaller extent even direct radiation damage [22].

Protein are long chains of L-α amino acids (also referred as residues), joined by peptide bonds. By convention, a chain under 40 residues is often identified as a peptide, rather than a protein. Fig. 1.3 shows the formation of a dipeptide from two amino acids.

To date, experimental studies radiation damage studies on gas-phase systems have focused on free amino acids or on very small peptides. In this thesis radiation action on the small pentapeptide leucine enkephalin (5 residues) and on the much larger protein ubiquitin (76 residues) is studied experimentally, as a first step towards the different slightly larger histones. It is envisioned that the experimental investigations presented in this thesis will pave the way towards investigation of even more realistic systems such as histones, histone complexes and possibly even models for nucleosome core particles consisting of histones and DNA.

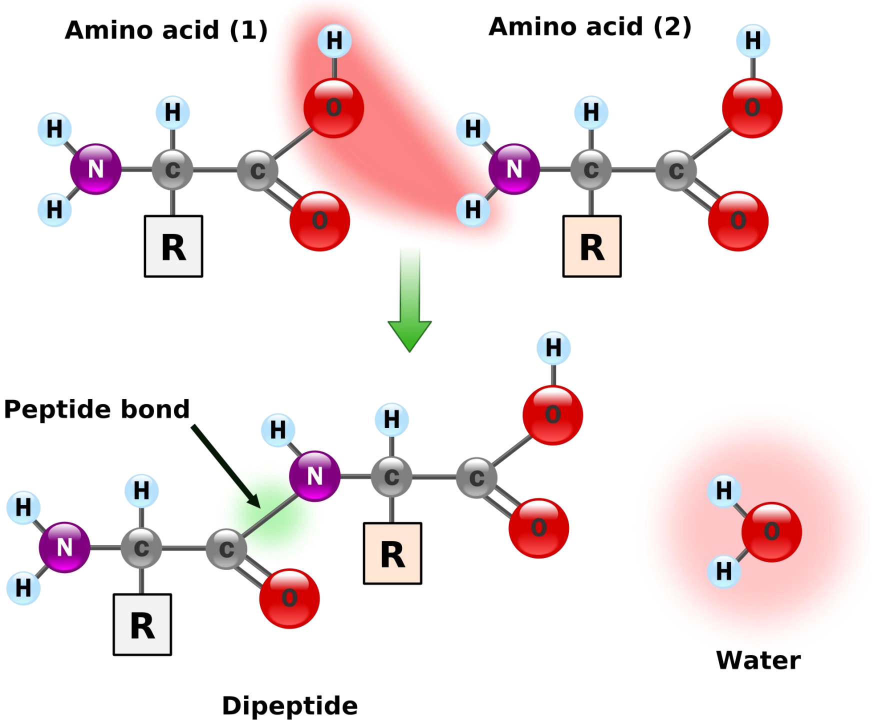

Figure 1.3: *Schematic for the formation of a dipeptide. Each amino acid has an amine- and a carboxylic acids group terminal. A water molecule is released during formation of a peptide bond between two amino acids.*

In order to perform their biological function, proteins fold into one or more specific spatial conformations. Determination of protein three-dimensional structure is therefore of paramount importance.

The structure of proteins involves four levels, which are referred to as primary, secondary, tertiary, and quaternary structures as shown in Fig. 1.4. The primary structure is simply the amino acid sequence which gives rise to a secondary (spatial) structure, for instance into well defined classes of sheets and helices. These substructures in turn fold into the actual protein three dimensional (or tertiary) structure. Complexes of two or more proteins are referred to as quaternary structures. Due to the mass-spectrometric approach employed, throughout this thesis, the term structure will be used synonymous to primary structure or sequence. At present, the most straightforward technique to identify the primary structure of a protein is using mass spectroscopy techniques. The protein is split into smaller peptides, transfered to the gas phase and ionized (e.g. by electrospray ionization) and dissociated. The sequence can be inferred from the specific fingerprint of its fragments in the mass spectrum [23].

In this thesis, we used the common nomenclature of peptide fragmentation that is depicted in Fig. 1.5. Depending on the location of the initial charge after the bond scission, an N-terminal fragment (indicated by the letters a, b, or c) or a C-terminal fragment (indicated by the letters x, y or z) is formed [24]. The numbering indicates which peptide bond is cleaved counting from the N-and C-terminus respectively, and is thus equal to the number of amino acid residues in the fragment ion. Internal fragments, which involve two or more broken bonds are usually formed from b–type and y–type cleavages. An immonium ion is a particular and common case of an internal ion, where a combination of an a–type and y–type cleavages takes place. The notation used for label internal fragments and immonium ions are their one-letter amino acid code.

A usual way to fragment the (de)protonated peptide is by collision–induced dissociation (CID), where the peptide is heated by multiple collisions with gas atoms or molecules until bond fission occurs. Most common fragments in low energetic CID are b and y-ions produced by the cleavage of the peptide bond. Because the maximal amount of internal energy deposited may be insufficient to cause dissociation, low energy CID results in a limited number of fragment ions, specially in large biomolecules. Therefore, a entire field of competing experimental techniques has been introduced [25]. For example, well established fragmentation techniques are: blackbody infrared radiative dissociation (BIRD) [26], electron-capture dissociation (ECD) [27], electron-transfer dissociation (ETD) [28], electron-detachment dissociation (EDD) [29, 30], high-energy collisional dissociation (HCD) [31], infrared multiphoton dissociation (IRMPD) [32, 33], negative electron-transfer dissociation (NETD) [34], or surface-induced dissociation (SID) [35].

However, it was the advent of ion traps in the field of mass spectrometry, that enabled the access to activation techniques which are associated with relatively low interaction cross sections. Ion traps allow for accumulation of sufficiently large numbers of sample biomolecular ions as well as for storing of these ions for many seconds. In this thesis, radiofrequency (RF) ion trapping is used. It has already been shown that this approach allows to study keV ion–induced ionization and dissociation (KID) [36] of protonated peptides. KeV ion collisions feature fs–interaction times and much higher excitation energies that cannot be reached by CID. Furthermore, mass spectrometry based on RF ion traps has recently successfully been combined with synchrotron radiation sources for investigation of VUV and soft X-rays photofragmentation of previously unaccessible peptide and protein ions [37–39].

For instance, it was previously shown that upon VUV photoionization, the protonated pentapeptide leucine enkephalin is subject to fragmentation mainly into ions stemming from the sidechains of aromatic residues [37]. Charge migration and ultrafast fragmentation was tentatively invoked to explain the fragmentation pattern. In this thesis, the migration of photoinduced charges will be studied in a set of synthetic peptides of variable length, always featuring aromatic residues on the two terminal positions. Urging questions to be answered are *i) What are the contributions of the peptide components (sidechains, backbone, terminii)*

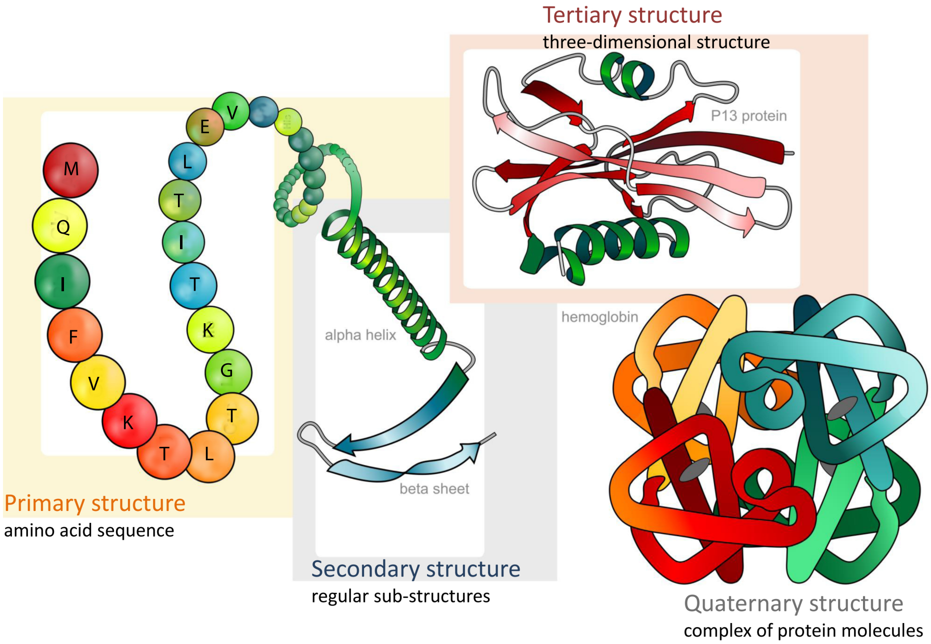

Figure 1.4: *Main protein structures levels.*

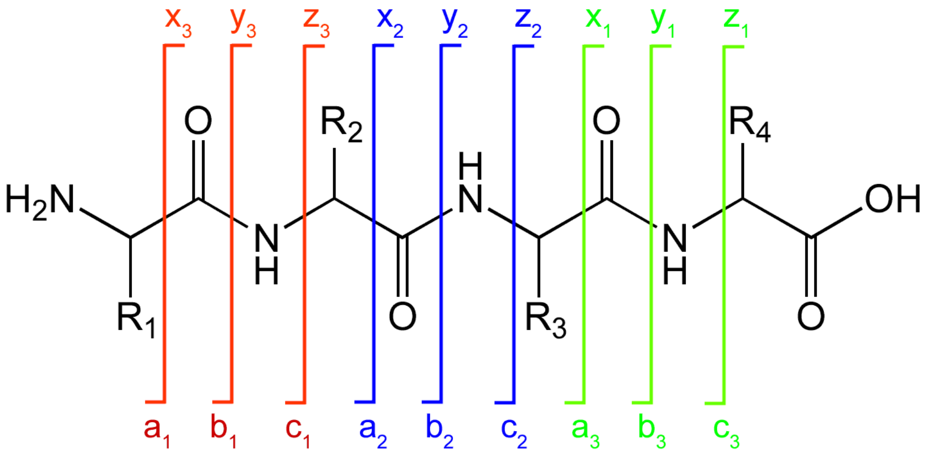

Figure 1.5: *Peptide fragmentation notation.*

to the VUV photoabsorption cross section? ii) Can the charge migration driven ultrafast fragmentation be quenched by increasing the peptide size?

Milosavljevic *et al.*, on the other hand, did a pioneering study on soft X-ray absorption of trapped gas-phase multiply protonated proteins and found non-dissociative single and double photoionization to be dominant [40]. In this thesis, similar experiments on the much smaller pentapeptide leucine enkephalin will be presented. In contrast to VUV absorption, soft X-ray absorption close to C K-edge allows for controlled localized core excitation of the protonated peptide. In particular, the following questions will be answered: *What is the relative importance of non-dissociative processes as compared to fragmentation for the case of smaller peptides? Is it possible to link photoabsorption sites to fragmentation channels? Do the aromatic sidechains play a similarly special role as for the case of VUV photoionization?*

Eventually, it will be experimentally investigated if charge migration followed by ultrafast fragmentation invoked for small protonated peptides, is a possible photofragmentation channel also in much larger multiply protonated proteins. To this end, the transition from single photon absorption to massive multiphoton absorption in ultrashort XUV pulses will be studied. As an ideal source of intense and ultrashort pulses of energetic photons, the free electron laser FLASH in Hamburg was used.

1.3 Thesis outline

This thesis is organized as follows:

- Chapter 2 introduces the main features of the experimental techniques used in this work. The tandem mass spectrometer “Paultje” will be described in detail. Also, a brief description of the used synchrotron facilities BESSY II and MAXlab and of the free electron laser FLASH will be given.
- Chapter 3 deals with ion and photon induced fragmentation of the oligonucleotide GCAT. The role of initial protonation sites will be discussed, fragmentation pathways will be identified and the formation of protonated and non-protonated fragment ions will be discussed.
- Chapter 4 focuses on VUV photofragmentation of synthetic protonated peptides. The influence of peptide length on fragmentation is be discussed in the framework of fast charge migration. Photoionization cross sections are determined.
- Chapter 5 presents a pioneering Near Edge X-ray Absorption Mass Spectrometry (NEXAMS) study for protonated leucine enkephalin at the carbon K-edge.
- Chapter 6 deals with the ionization and fragmentation of the protonated protein ubiquitin upon (multi) photon absorption.

Chapter 3 is based on the corresponding publication in Physical Review A. Chapter 4 to 5 are copies of the corresponding papers in Physical Chemistry Chemical Physics and Journal of Physical Chemistry A. All of them are here reproduced under permission of the journal editors.

BIBLIOGRAPHY

[1] García Gómez-Tejedor, G. and Fuss, M. C., editors, *Radiation Damage in Biomolecular Systems*, Springer (2012).

[2] von Sonntag, C., *The chemical basis for radiation biology*, Taylor and Francis, London (1987).

[3] Brändas, E. and Sabin, J. R., Advances in Quantum Chemistry, **vol 52**, Academic Press (2007).

[4] Röntgen, W. C., Nature, **53**, 274 (1896).

[5] Becquerel, H., Comptes Rendus, **122**, 501 (1896).

[6] Curie, P. and Curie, M., Comptes Rendus, **127**, 175 (1898).

[7] Curie, P., Curie, M., and Bémont, G., Comptes Rendus, **127**, 1215 (1898).

[8] Becquerel, H., Nobel Lecture: On Radioactivity, a New Property of Matter (1903).

[9] Curie, P., Nobel Lecture: Radioactive Substances, Especially Radium (1903).

[10] Despeignes, V., Lyon Med. J., **82**, 428 (1896).

[11] Stevens, L., Br. Med. J., **1**, 998 (1896).

[12] Nias, A., *An Introduction to Radiobiology*, Wiley (1998).

[13] ICRP, *The 2007 Recommendations of the International Commission on Radiological Protection.*, volume 37 (2-4) (2007).

[14] National Institute for Public Health and the Environment (The Netherlands), http://-www.rivm.nl (2013).

[15] PTCOG: Particle Therapy Co-Operative Group, http://ptcog.web.psi.ch/ (2013).

[16] Miescher, F., Medicinisch-chemische Untersuchungen, **4**, 441 (1871).

[17] Kossel, A., Nobel Lecture: The Chemical Composition of the Cell Nucleus (1910).

[18] Avery, O. T., MacLeod, C. M., and McCarty, M., J. Exp. Med., **79**, 137 (1944).

[19] Watson, J. D. and Crick, F. H. C., Nature, **171**, 737 (1953).

[20] Franklin, R. E. and Gosling, R. G., Nature, **172**, 156 (1953).

[21] Wilkins, M. H. F., Stokes, A. R., and Wilson, H. R., Nature, **171**, 738 (1953).

[22] Roginskaya, M., Bernhard, W. A., and Razskazovskiy, Y., Radiat. Res., **166**, 9 (2006).

[23] Steen, H. and Mann, M., Nat. Rev. Mol. Cell Biol., **5**, 699 (2004).

[24] Roepstorff, P. and Fohlman, J., Biol. Mass Spectrom., **11**, 601 (1984).

[25] Sleno, L. and Volmer, D. A., J. Mass Spectrom., **39**, 1091 (2004).

[26] Dunbar, R. C., Mass Spectrom. Rev., **23**, 127 (2004).

[27] Cooper, H. J., Håkansson, K., and Marshall, A. G., Mass Spectrom. Rev., **24**, 201 (2005).

[28] McLuckey, S. A. and Stephenson, J. L., Mass Spectrom. Rev., **17**, 369 (1998).

[29] Budnik, B. A., Haselmann, K. F., and Zubarev, R. A., Chem. Phys. Lett., **342**, 299 (2001).

[30] Kinet, C., Gabelica, V., Balbeur, D., and De Pauw, E., Int. J. Mass Spectrom., **283**, 206 (2009).

[31] Olsen, J. V., Macek, B., Lange, O., Makarov, A., Horning, S., and Mann, M., Nat. Meth., **4**, 709 (2007).

[32] Little, D. P., Speir, J. P., Senko, M. W., O'Connor, P. B., and McLafferty, F. W., Anal. Chem., **66**, 2809 (1994).

[33] Laskin, J. and Futrell, J. H., Mass Spectrom. Rev., **24**, 135 (2005).

[34] Coon, J., Shabanowitz, J., Hunt, D., and Syka, J., J. Am. Soc. Mass Spectrom., **16**, 880 (2005).

[35] Mabud, M., Dekrey, M. J., and Cooks, R. G., Int.. J. Mass Spectrom., **67**, 285 (1985).

[36] Bari, S., Hoekstra, R., and Schlathölter, T., Phys. Chem. Chem. Phys., **12**, 3360 (2010).

[37] Bari, S., González-Magaña, O., Reitsma, G., Hoekstra, R., Werner, J., Schippers, S., and Schlathölter, T., J. Chem. Phys., **134**, 024314 (2011).

[38] Milosavljević, A. R., Nicolas, C., Gil, J. F., Canon, F., Réfrégiers, M., L, N., and Giuliani, A., J. Synchrotron Radiat., **2**, 174 (2012).

[39] Brunet, C., Antoine, R., Dugourd, P., Canon, F., Giuliani, A., and Nahon, L., J. Am. Soc. Mass Spectrom., **23**, 274 (2012).

[40] Milosavljević, A. R., Canon, F., Nicolas, C., Miron, C., Nahon, L., and Giuliani, A., J. Phys. Chem. Lett., **3**, 1191 (2012).

Chapter 2

Experiment

The experimental data in this thesis was obtained using our home-built setup called Paultje, whose name honors Nobel laureate Wolfgang Paul, the inventor of the radiofrequency ion trap, nowadays often referred to as Paul-trap [1]. Paultje is the Dutch word for "little Paul". The setup was commissioned in 2009 to perform radiation damage studies on medium-sized biomolecules in the gas phase. Paultje allows for the study of gas-phase ionic biomolecules too fragile for standard techniques such as evaporation in an oven. Paulje is portable and can thus be interfaced with external ionizing radiation sources. In the course of this thesis, Paultje has been interfaced with high brilliance VUV and soft X-rays photon beamlines located at the 3rd generation synchrotron facilities BESSY II (HZB, Berlin, Germany) and MAX–Lab (Lund, Sweden), the free electron laser facility FLASH (DESY, Hamburg, Germany), and last but not least, our ECR ion source for keV highly charged ions at the KVI (Groningen, The Netherlands). The use of all these radiation sources makes it possible to obtain detailed information on ionization-induced fragmentation dynamics in biomolecular systems.

In this chapter, the main features of the experimental setup used for production, mass selection, trapping, and irradiation of protonated biomolecules as well as the detection of the ionic fragments are discussed. As a complement, a brief description of the used keV ion and synchrotron light sources and their properties is given.

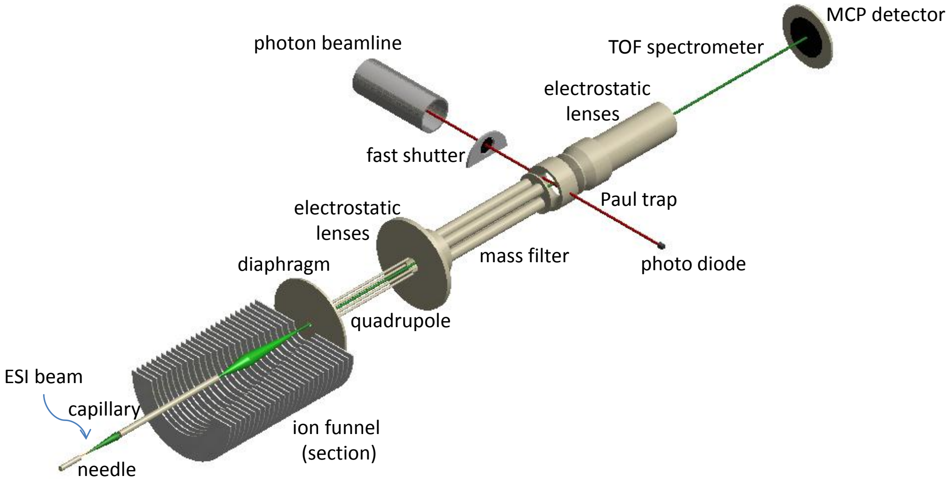

Figure 2.1: *Sketch of the setup. The green line represents the trajectories of the biomolecular ions. The red line is the path of the ionizing radiation, i.e. energetic photons or ions.*

2.1 Paultje setup

The main purpose of Paultje is the study of dynamics in protonated gas–phase (bio)molecular ions produced by an electrospray ionization source (ESI) and stored in an ion trap. As shown in Fig. 2.1, the electrosprayed ions enter the first vacuum section of the setup through a small capillary tube. After being transported and phase-space compressed by means of an ion funnel and a RF–only quadrupole ion guide, only the ions with a selected m/z ratio (where m and z are the mass in a.m.u. and the charge state of the ions) are transported through a quadrupole mass filter. The mass–filtered ions reach the entrance of a 3D RF ion trap via an electrostatic lens system (not shown in the figure). Trapping these ions requires that their kinetic energy does not exceed the depth of the trap potential. To enhance the trapping efficiency collisional cooling during the trap loading is applied. To achieve the cooling a helium buffer gas is introduced into the trap through a pulsed valve.

The trap is loaded until the number of ions is high enough to reach a sufficient signal–to–noise ratio in the experiment. Typical loading times range from 50 to 3000 ms depending on the size and protonation state of the molecule sprayed. The number of ions that can been stored depends on several factors, such as the maximal charge density of the ion cloud, the m and z values of the ions, and the RF amplitude and frequency. For the protonated peptide leucine-enkephalin the number of trapped ions was estimated to be at least 2000 ions [2]. Now the trap content can be irradiated by keV ions or energetic photons. A photograph of the setup connected to the synchrotron BESSY II is displayed in Fig. 2.2.

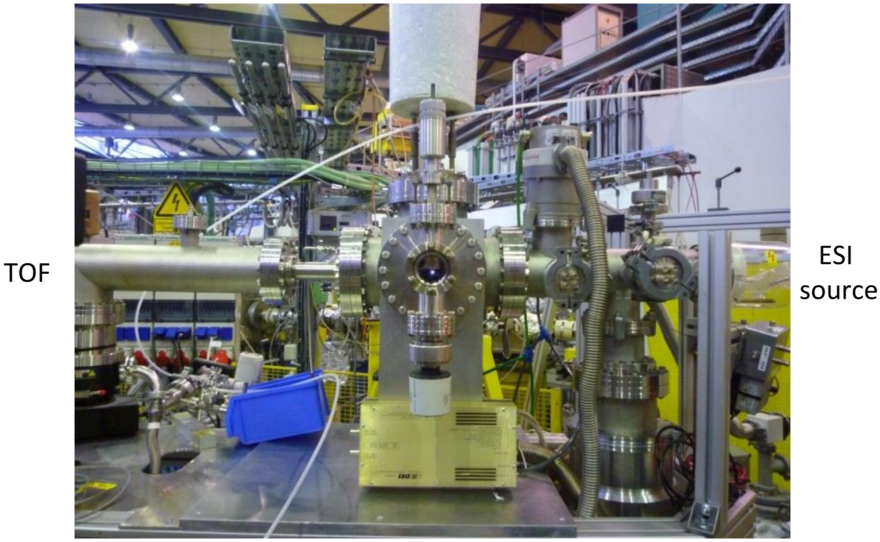

Figure 2.2: *The Paultje setup interfaced to the U125 10m NIM beamline at the synchrotron facility BESSY II. Note at the center of the picture the synchrotron light coming out of the setup after crossing the Paul trap.*

After irradiation, a second He buffer gas pulse is applied which collisionally cools down the fragment ions and dissipates the kinetic energy release resulting from the fragmentation process. The content of the trap is then extracted into a mass spectrometer where the ion times–of–flight (TOF) are recorded after detection on a multi channel plate (MCP) detector. For each extraction we obtain a TOF spectrum that contains many peaks. Not all of the measured peaks or all of their intensity stems from the interaction of trapped ions with the photon or ion beam. There are spectral contributions from other sources leading to unwanted background. Therefore, in addition two types of reference TOF spectra are acquired, namely 1) trapped ions only, no radiation, and 2) radiation only, no trapped ions. This 3 stage measurement cycle typically takes between 1 and 3 seconds For sufficient statistics and a good signal-to-noise ratio, it is typically necessary to average the spectra from several hundred acquisition cycles.

2.2 Electrospray ionization

Electrospray ionization (ESI) is a technique that gently transfers ions, present in solution, into the gas phase. ESI is based on electro-hydrodynamic atomization of a solution containing electrolyte ions at concentrations greater than 10^{-6} mol/L or μM. The ESI source can produce negative or positive molecular beams from a wide variety of molecular compounds M (for instance proteins, oligonucleotides and polymers), using almost any solute organic molecule. The ESI beam can consist of deprotonated ($[M - H]^-$) or protonated molecules ($[M + H]^+$). Multiple (de)protonation $[M \pm nH]^{n\pm}$ is commonly found. The gentleness of an ion-transfer method is understood as the degree to which fragmentation of the ions is avoided. ESI forms intact ions and overcomes the fragmentation tendency for large biomolecules that are produced using other methods such as, for example, an effusive oven working at high temperature.

Modern electrospray mass spectrometry (ESMS) was first presented by Fenn and Yamashita in 1984 [3, 4], but its foundation was laid a long time before. To summarize this long history briefly (see reference [5]), in 1882 the maximum amount of charge that a liquid droplet can carry was estimated by Lord Rayleigh. This maximum charge for which Coulomb repulsion and surface tension are in equilibrium is known as the Rayleigh limit. Already in 1914, John Zeleny studied the behavior of fluid droplets at the end of glass capillaries and presented the first time-lapse images of the dynamics of a liquid meniscus. Many years later in the 1960s, Sir Geoffrey Taylor established the principles of electrospraying with his study of electrostatic dispersion of a liquid into charged droplets [6]. It is important to note here that he described the formation of what is now called the Taylor cone; the conical shape that is assumed by a liquid surface under application of an intense electric field. Based on Zeleny's techniques, in 1967, Malcom Dole proposed dispersing a dilute solution containing macromolecules as a fine spray of charged droplets into a bath gas at atmospheric pressure and allow this spray to enter a mass analyzer system in vacuum [7]. Unfortunately, to perform the mass analysis, he used a retarding potential method that limited the study to only heavy macromolecules like polymers. Finally, in the 1980s, John B. Fenn's group resumed Dole's experiments but they interfaced the ESI source with a small quadrupole mass analyzer and a time-of-flight spectrometer. Fenn could then electrospray and analyze intact gas-phase biomolecules up to ≈ m/z 1500. In 2002, John. B. Fenn was awarded the Nobel prize in chemistry "for their development of soft desorption ionisation methods for mass spectrometric analyses of biological macromolecules".

The fundamental concepts of ESI are depicted in Fig. 2.3. Briefly, the solution that contains the ions is pumped through the tip of a hollow needle, forming a liquid meniscus at atmospheric pressure. We use a needle made of 304ss stainless steel (Vita Needle, Needham,USA) with a length of (50.8±0.5) mm, an external diameter of (228.6±12.7) μm and an internal orifice diameter of (101.6 +25.4/-12.7) μm. A long capillary tube is installed in front of the needle, at a distance of ≈ 5 mm. Stainless steel capillaries of 20 cm length, outer diameter of 1.5875 mm (1/16 inch) and inner diameters from 0.005 (127 μm) to 0.02" (508 μm) were tested and used in the course of this thesis. A positive high voltage (typically 3 to 5 kV) applied to the needle produces a strong electric field between needle and its capillary counter electrode. The electric field lines penetrate into the solution, separating the positive and negative charges. The positive ions concentrate close to the surface of the

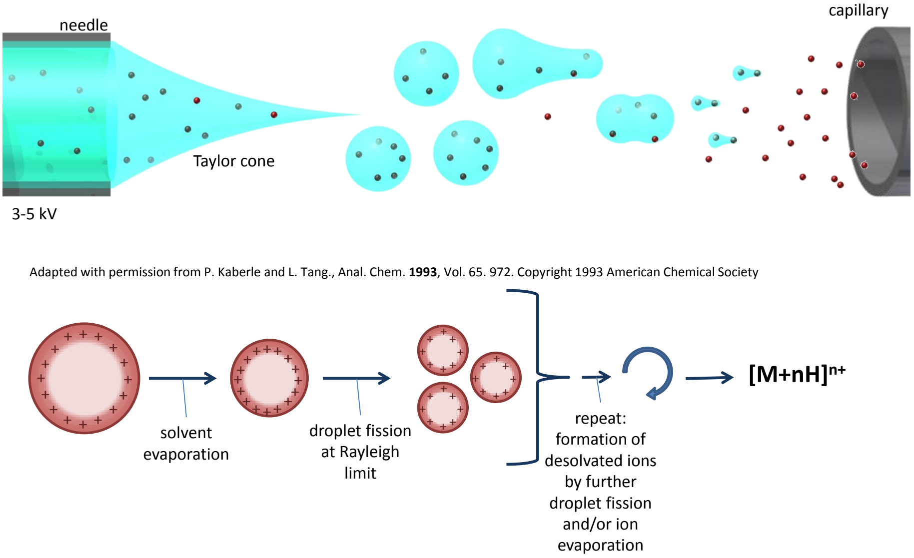

Adapted with permission from P. Kaberle and L. Tang., Anal. Chem. **1993**, Vol. 65. 972. Copyright 1993 American Chemical Society

Adapted with permission from Simon J. Gasket, J. Mass Spectrom. Vol. 32, 677 (1997) Copyright 1997 John Wiley & Sons, Ltd.

Figure 2.3: *Schematic of electrospray processes. Top: Application of a positive high voltage to the needle confines positive electrolyte ions towards the liquid surface. A high charge density in the meniscus leads to the formation of a Taylor cone and emission of a jet of highly charged droplets. Bottom: Charged droplets shrink by solvent evaporation and increase in charge density. Droplets split into smaller droplets when the Rayleigh limit is reached. Final formation of gas-phase ions is explained by Ion Evaporation (IEM) and Charge Residue (CRM) models (see text).*

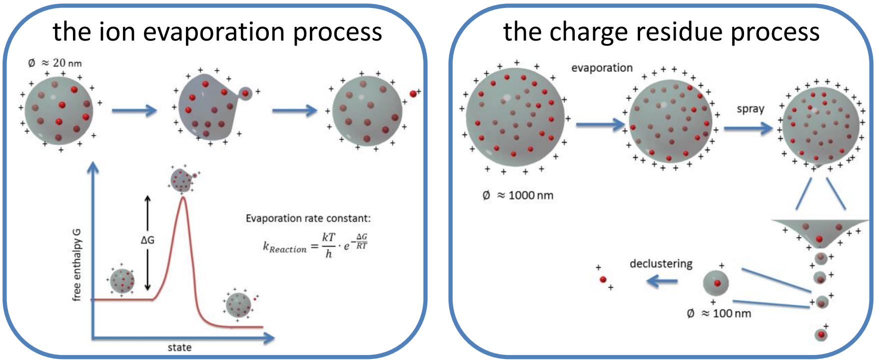
the ion evaporation process

the charge residue process

Adapted with permission from Matthias Wilm, Molecular & Cellular Proteomics. 10, M111,009407 (2011)
© the American Society for Biochemistry and Molecular Biology

Figure 2.4: *Ion evaporation (left panel) and charge residue (right panel) models for electrospray ionization (see text).*

meniscus whereas the negative charges are pushed towards the needle surface. This charge separation eventually leads to formation of positively charged droplets in a process that is described below. Note that negatively charged droplets can be produced if the polarity of the high voltage is reversed.

The formation of the meniscus is generally dominated by two concurring forces, namely surface tension and Coulombic force. The electrostatic attraction pulls the liquid from the needle towards the capillary whereas the surface tension pulls the solution back to the needle to minimize the energetically unfavorable surface area. At equilibrium the meniscus assumes the shape of a pointed "Taylor" cone. The cone has an opening angle of 49.3 ° [6]. In higher electric fields, the liquid at the tip of the Taylor Cone starts to spray small charged droplets whose diameters are of the order of up to several μm. The only question that remains in the context of the ESI process is how single molecular ions are formed from relatively large droplets?

The transition from a static tailor cone to a jet of droplets occurs because the charged surface at the tip of the Taylor Cone avoids turning into an infinitesimally sharp tip that constitutes an electric field singularity [8]. The produced droplets are generally close to their Rayleigh limit, i.e. they have almost the maximum amount of charge that they can carry. The charged droplets are dragged towards the capillary by the electrostatic force. During this process, solvent molecules start to evaporate in neutral form and the droplets accordingly shrink. The charge density of the droplets increases. The surface tension of the droplet will balance the Coulomb force up to reaching the Rayleigh limit. Now, two processes can occur: i) the electrostatic repulsion leads to a Coulomb explosion of the entire droplet into smaller droplets (see bottom of Fig. 2.3) [9, 10] or ii) a new Taylor cone appears on a localized point on the droplet, ejecting a jet of smaller highly charged droplets of about 1/10th of the original droplet size [8, 11]. Both processes are repeated until the Rayleigh limit cannot be reached any more due to the limited evaporation rate of the solvent. Gomez and Tang have studied the charging and fission of droplets in ESI and found that the larger the droplets the closer they are to the Rayleigh limit [11]. The final droplets can reach sizes of the order of 200 nm or less [8].

There are two models to explain the final formation of gas-phase ions from these final droplets: the Ion Evaporation Model (IEM) [12, 13] and the Charge Residue Model (CRM) [7, 14] (see Fig. 2.4). The IEM assumes that ions can be evaporated directly from the droplet surface when a strong electric field is present at the surface of the solvent. The solvation energy is around 3 to 6 eV for a typical ion, depending of its charge and size. This implies that we can rule out the evaporation of ions at room temperature. At room temperature the thermal energy is approximately 25 meV implying that the Boltzman factor ($e^{-\frac{\Delta E}{kT}}$) even for an ΔE of 3 eV is already on the order of 10^{-51}. However, the situation changes for small droplets with diameters of about 20 nm in the presence of an intense electrical field [13]. In this case the potential energy of the ions near to the liquid surface can overcome the barrier and accordingly ions can leave the droplet. Alternatively, the CRM assumes that droplets containing only one ion can be produced and that further evaporation of the solvent can occur until a free ion is formed. In fact, for a solution with a pmol/μl analyte concentration, a droplet of around 200 nm contains on average less that one analyte molecule [8]. The general consensus is that large molecular ion formation is more accurately described by CRM whereas for smaller ions IEM governs the process.

2.3 Transport and trapping of ions

The experiment has to be performed under high-vacuum conditions at which ions can be controlled and trapped. It is thus necessary to transport the electrosprayed ions through a set of differential pumping stages which reduce the pressure from atmospheric to the operational high vacuum of the ion trap (10^{-9} mbar).

The capillary is the first component of the system and serves as an entrance for the ESI ions. It also provides a low vacuum conductance interface towards the first vacuum chamber where, depending on the inner diameter of the capillary, a high pumping speed (270 m^3/h) roots–blower keeps the pressure between 0.1 to 1 mbar. Neutral gas particles and ions leaving the capillary exit undergo a sonic expansion due to the pressure difference between both ends of the capillary. A low ion transmission efficiency is found in this high pressure region, the ion current that is transmitted towards the quadrupole is around two orders of magnitude lower than the total current produced by the ESI source (roughly 100 to 200 nA).

In the first version of the Paultje setup [2], we used an aluminium skimmer (1 mm diameter) in front of the capillary that separated the region between capillary and first quadrupole chamber. This way, the operational pressure in the quadrupole chamber was $\approx 3\text{x}10^{-4}$ mbar.

In the course of this thesis, the skimmer was replaced by an RF ion funnel device that improves significantly the transmission of the ions in the capillary chamber. The ion funnel collects the expanding ions from the capillary and focuses them towards a diaphragm with a 2 mm aperture. The diaphragm acts as a simple electrostatic lens when it is biased with a positive voltage (typically less than +14 V). An RF quadrupole installed behind the diaphragm guides the ions towards the mass filter chamber where the operational pressure is below 10^{-7} mbar. A set of electrostatics lenses (typically biased with < 5V) is installed between first quadrupole and mass filter chamber. Ions leaving the mass filter finally enter the collision chamber where they are focused into the 3D RF ion trap (Paul trap). Under operational conditions the pressure in this chamber is below 10^{-8} mbar.

Inherently to the ion transport is the necessity of slowing the ions down while at the same time focusing the ions sufficiently for maximum transport between the sections. The theorem of Liouville states that the phase space volume of a system of non–interacting particles is conserved. This implies that decreasing the ion momenta will worsen the beam emittance.

This problem can be overcome by operation of RF funnel and RF quadrupole at pressures in the range between 1 mbar and of $\approx 10^{-2}$ mbar and exploiting the collisional damping of the ion trajectories, which confines ions to the center of the guides [15]. The effect is insignificant in (ultra)high vacuum and disperses the beam at too high a pressure. For masses up to at least 17000 u collisional focusing increases with the mass of the ion (not the mass-to-charge ratio) and it is accompanied by significant lowering of the axial kinetic energy [15]. It is thus beneficial to maintain a relatively high operational pressure in the ion funnel and first quadrupole chamber, for achieving a high transmission of ions towards the mass filter.

2.3.1 Ion funnel

In a study on ion mobility, Smith et al. [17] found that analyte protein compounds can account for more than 50% of the total current produced by an ESI source. However only 1 in every 10^5 ions gets transferred through the system into vacuum [17]. This low transmission efficiency is a general characteristic for ion beams produced by high pressure sources, such as ESI, and is mainly due to multiple collisions with residual gas molecules in the expansion region behind the capillary.

The reduction of ion loss in an atmospheric source such as an ESI is not trivial. As already mentioned earlier, in the old version of our setup (see Ref. [2]), a skimmer with a small orifice of 1 mm was used. The skimmer was biased with a few volts (typically +6 V) and installed a couple of millimeters from the capillary. The electrical field between capillary and skimmer ensured sufficient acceleration of the ions between collisions with residual gas molecules. However a skimmer merely cuts out a small fraction of the expanding ion cloud and creates a major sensitivity bottleneck for mass spectroscopy [18]. Furthermore, collision induced dissociation is more likely to occur if the voltage in the expansion region is too high.

Shaffer et al. presented an electrodynamic ion funnel device to improve transmission. Their device is operational at pressure regions of the order of mbar and leads to a transmission increase of at least one order of magnitude as compared to a capillary - skimmer configuration [19]. Briefly, the ion funnel is a stack of thin cylindrical ring electrodes with decreasing internal diameters. An RF voltage is applied to the funnel electrodes in a way that neighboring electrodes are phase-shifted by 180° thereby creating an effective potential which confines ions radially, whereas a DC axial electric field gradient pushes the ions towards the exit electrode [20]. A sketch of our ion funnel is shown in Figs. 2.5 and 2.6.

Our ion funnel [21] is based on the design by Julian et al. [16]. It consists of a stack of 26 ring electrodes with a separation of 5.1 mm. The first ten rings are made of copper and have a constant inner diameter of 38.1 mm. The remaining 16 electrodes are made of stainless steel with inner diameters decreasing linearly from 36.3 to 7.9 mm on the exit electrode. The RF peak-to-peak voltage amplitudes are of the order of 100 to 140 V at frequencies typically

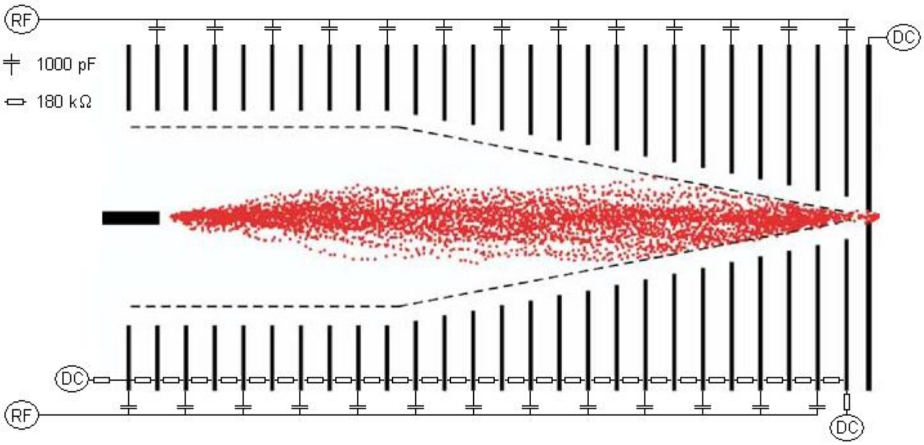

Figure 2.5: *Sketch of the ion funnel. Ions leaving the capillary (left) are funneled towards the exit of the funnel where they enter the quadrupole guide. Adapted from Ref. [16].*

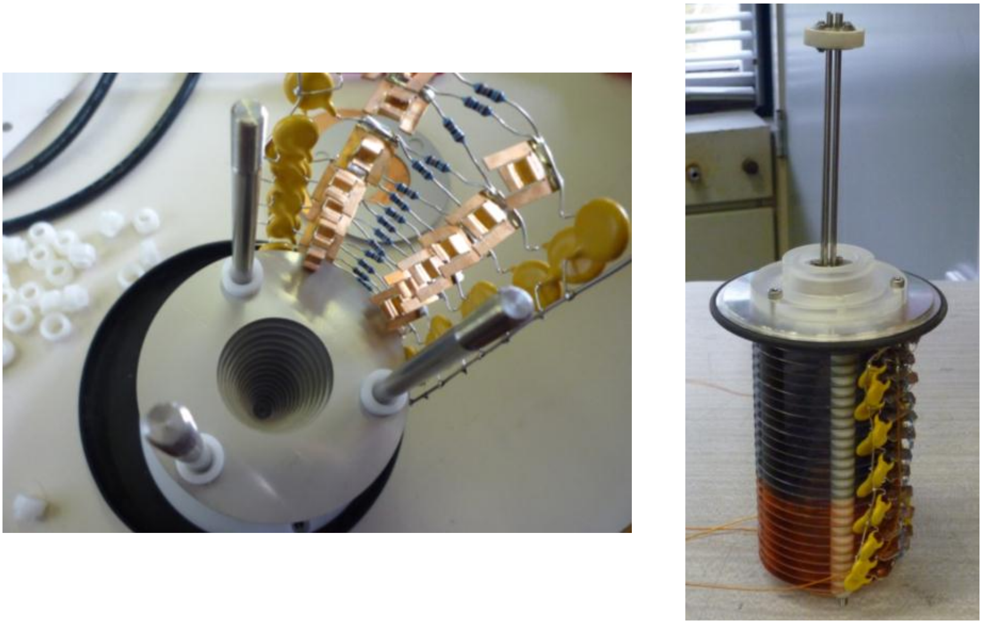

Figure 2.6: *left: Building of the ion funnel. Right: Ion funnel ready to be installed. On top of the RF ion funnel the first quadrupole guide is shown.*

somewhere between 150 to 900 kHz.

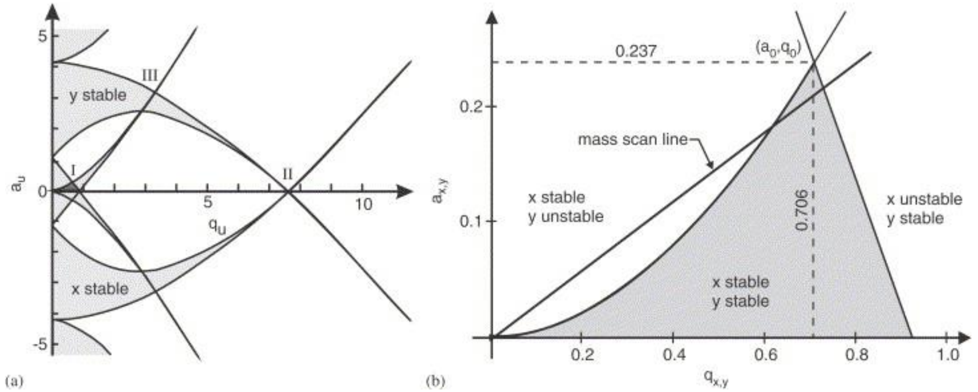

Reprinted from Physics Report, Vol. 425, Issue 1, Klaus Blaum, High-accuracy mass spectrometry with stored ions, 1, Copyright 2006, with permission from Elsevier

Figure 2.7: *(a) Stability regions (gray shaded) of the quadrupole mass filter. (b) zoom of stability region I (dark grey area in left panel).*

2.3.2 Quadrupole operational principle: the Mathieu equations

The Mathieu equations describe the dynamics of a charged particle (mass m and charge e) in a quadrupole potential and therefore they help to optimize parameter settings of RF quadrupole and ion trap devices. The movement of the ion in a potential is described by the equation

$$m\frac{d^2\vec{r}}{dt^2} = -e\nabla\Phi \tag{2.1}$$

with the quadrupole potential Φ expressed as

$$\Phi = \frac{\Phi_0}{r_0^2}(\lambda x^2 + \sigma y^2 + \gamma z^2) \tag{2.2}$$

where Φ_0 is the applied potential (an RF potential either alone or in combination with a DC voltage), λ, σ and γ are weighting constants for the x, y and z coordinates respectively, and r_0 is a constant related to the size of the system which is defined separately depending on whether the device is an ion trap or a linear quadrupole (see discussion below). Note that the potential increases quadratically with the coordinates x, y and z. Therefore, an ion in a quadrupole field experiences a restoring force that drives the ion back towards the center. In an electrical field without external charge it is mandatory to satisfy the Laplace condition ($\nabla^2\Phi = 0$) which ensures that the field is linear. This results in the condition:

$$\lambda + \sigma + \gamma = 0 \tag{2.3}$$

that can be satisfied in many ways. Most relevant conditions for this discussion are: $\lambda = \sigma = 1$ and $\gamma = -2$, and $\lambda = 1, \sigma = -1$ and $\gamma = 0$. The first one corresponds to a 3D ion trap geometry and the later one to a 2D linear quadrupole.

We start with the conditions for a linear quadrupole ($\lambda = 1, \sigma = -1$ and $\gamma = 0$), for which the motion in the axial direction (z axis) is independent of the x and y directions. The applied potential to the electrodes is $\Phi_0 = \pm U \mp V\cos(\Omega t)$. Where $\Omega = 2\pi f$ is the angular frequency of the RF voltage, U is the applied DC voltage while V is the RF amplitude.

We can then derive the equation of motion in one direction,

$$m\frac{d^2x}{dt^2} = \frac{-e}{r_0^2}\Big(U + V\cos(\Omega t)\Big)x \tag{2.4}$$

Using the coordinate $u = x$ or y and introducing dimensionless parameters ξ, a_u and q_u one obtains the canonical form of the Mathieu equation (for details see reference [22])

$$m\frac{d^2u}{dt^2} = \frac{-m\Omega^2}{4}\Big(a_u - 2q_u\cos(\Omega t)\Big)u \tag{2.5}$$

$$\frac{d^2u}{d\xi^2} + \Big(a_u - 2q_u\cos(2\xi)\Big)u = 0 \tag{2.6}$$

where

$$\xi = \frac{\Omega t}{2},\ a_u = \frac{8eU}{mr_0^2\Omega^2} \text{ and } q_u = \frac{4eV}{mr_0^2\Omega^2}$$

With this equation one can determine whether ions with a specific m/z value will go through the quadrupole or not. Therefore, we need to find the set of values for a_u and q_u for which the ions can have stable trajectories.

A practical way to visualize the families of Matthieu-equation solutions with stable trajectories, is displaying the stability regions in a 2D graph. Fig. 2.7 shows the region of stability as a function of the parameters a_u and q_u, where u represent the coordinates x or y. Note that there are several stability regions in x and y which overlap. The implications here will be discussed in the next section.

2.3.3 RF quadrupole ion guiding and mass filtering

One of our quadrupoles is depicted in Fig. 2.8. Briefly, the quadrupole makes use of RF and DC voltages applied to four mutually parallel electrodes oriented such that their centers coincide with the corners of an imaginary square [22]. Ions with a given mass m and charge z, are guided along the quadrupole only for a set of suitable RF frequencies and DC and RF amplitudes. Ions traveling along unstable trajectories leave the quadrupole radially or hit the electrodes. Note that the stability of an ion trajectory is defined by the Mathieu parameters (see Fig. 2.7) and that if the frequency is constant the a_u parameter depends only on the DC voltage and q_u only on the RF amplitude. The quadrupole operates in the first stability region (I) where a_u and q_u are relatively small, and therefore it requires lower DC and RF amplitudes.

There are two operational modes that determine the behavior of the quadrupole as either an ion guide or a mass filter. The ion guide mode works using a constant RF amplitude and RF frequency. For a low DC voltage ($a_u \approx 0$) there is a large set of stable q_u values. Therefore, a large set of m/z ions can be transmitted through the quadrupole. On the other hand, the mass filter mode requires to follow a mass scan line like the one shown in the right panel of Fig. 2.7 until it reaches the values a_0 and q_0 in the apex of the stability plot.

Our home-built quadrupole ion guide has cylindrical rods of 2 mm diameter, a length of 117 mm and an effective radius, $r_0 = 2.8$ mm. Operational pressure is about 2 x 10^{-4} mbar. Typical operation frequencies range from 400 to 800 kHz with a peak–to–peak voltage of up to 280 V. To supply the RF peak–to–peak voltage we used a broadband power amplifier (ENI, model 3100L) connected to a Direct Digital Synthesis (DDS) frequency source which is equipped with a stable quartz-crystal oscillator that allows precise frequency tuning. The RF power amplifier is connected to a home-built broadband balun that provides two balanced output lines with a 180 degrees phase shift which are connected to the quadrupoles electrodes. The balun specifications are described elsewhere [2].

The mass filter has a length of 308 mm and the rods with $d = 9$ mm inscribe a circle with $r_0 = 3.92$ mm. The RF voltage is provided by a commercial quadrupole power supply (QPS-105, Ardara) which can supply a maximum RF peak–to–peak voltage of 2000 V at $\approx$ 800 kHz and a DC voltage range from -200 to +200 V.

2.3.4 RF ion trap

A commercial RF ion trap set which includes entrance and exit ion lenses is used to trap the mass-selected ions (Jordan TOF Products, USA). Its Mathieu stability diagram is analogous to the linear quadrupole if x and y in Fig. 2.7 are replaced by the cylindrical coordinates r and z which describe the geometry of the trap.

The trap consists of a central hyperbolic ring electrode enclosed by two hyperbolic end cap electrodes, as shown in Fig. 2.9. The internal radius of the ring electrode is $r_0 = 10$ mm

Figure 2.8: *Picture of one of our home–built mass filter quadrupoles.*

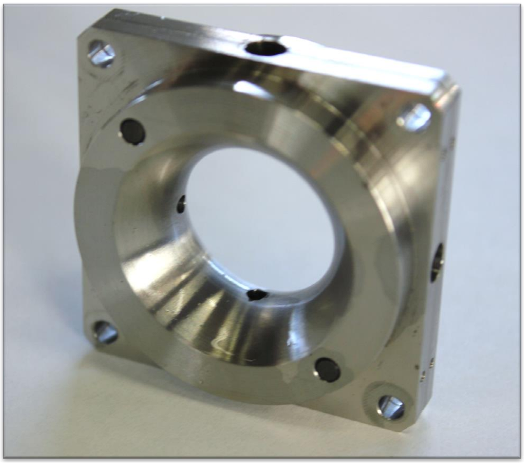

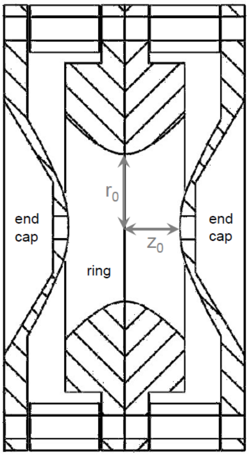

Figure 2.9: *Left: Picture of the Paul trap electrode ring. Rigth: Schematic cross section view of the ion trap, with* $r_0 = 10$ *mm and* $z_0 = 7$ *mm. The holes in the end caps are* $\phi = 3$ *mm*

whereas the distance from the center to the end caps is $z_0 = 7.07$ mm. These values satisfy the condition for an ideal quadrupole field given by the relation $r_0^2 = 2z_0^2$ [22]. The size of the entrance and exit holes in the ring (not visible in Fig. 2.9) and end caps have diameters of 2.4 mm and 3 mm respectively. The end cap holes are aligned on to the central axis from the ESI source to TOF spectrometer, whereas the central ring holes are aligned perpendicular to this axis on to the ion or photon beam. The base pressure inside the trap chamber is $\approx 1 \times 10^9$ mbar.

To get a broad m/z range for trapping, the experiments are performed in a RF–only mode, i.e. without applying a DC voltage. The end cap electrodes are then grounded and the RF voltage is applied to the ring electrode using a D-1230 model power supply (Jordan TOF Products) which can delivery up to 2500 Vpp. The typical RF peak–to–peak voltage applied to the ring electrode was 2100 Vpp at 1 MHz.

Two sets of electrostatic ion lenses are installed close to the trap, one between the mass filter and the entrance of the trap and the second between the exit of the Paul trap and the TOF tube. Mass selected ions that leave the mass filter are focused into the trap by the first electrostatic lens system that is biased to a potential of 4 to 6 V DC. Ions that enter the grounded electrode still have a kinetic energy of a few eV that has to be dissipated. This can be done using helium buffer gas pulses up to a pressure of $\approx 10^{-3}$ mbar. The use of the buffer gas increases the ion trapping efficiency and also decreases the size of the ion cloud in the trap, improving the final extraction through the end cap hole.

After several hundreds of ms for loading the trap, the ESI beam is deflected stopping the entrance of ions into the trap. The content of the trap then is exposed to the ion or photon beam. To avoid multiple collisions of the projectile beam with the same trapped molecule, the irradiation time was chosen to dissociate only about 10% of the content of the trap. Typical exposure times were about several hundreds of ms. A second buffer gas pulse is applied to cool down energetic dissociation products.

2.3.5 TOF mass spectrometer

In order to perform mass spectrometry of the content of the trap, the ions are extracted from the trap and accelerated towards a time–of–fligth (TOF) tube (length: 82 cm, $m/\Delta m = 200$) by means of a pulsed extraction voltage applied to the end caps of the trap. The extraction process is activated by a TTL signal provided to the D-1230 RF power supply. The rising edge of the TTL signal triggers the RF shutoff to the trap. The RF voltage is turned off only after the next zero voltage crossing into the positive polarity of the RF sinusoidal signal. A 500 μs time delay is introduced to allow the RF to decay. In this way the effective potential of the trap is close to zero before extraction. The extraction pulse is ± 200 V and lasts 3.5 ms.

The detector is a silhouette type micro–channel–plate detector (MCP, chevron configuration, diameter: 50 mm) with the front plate biased to -5 kV and the anode kept at ground

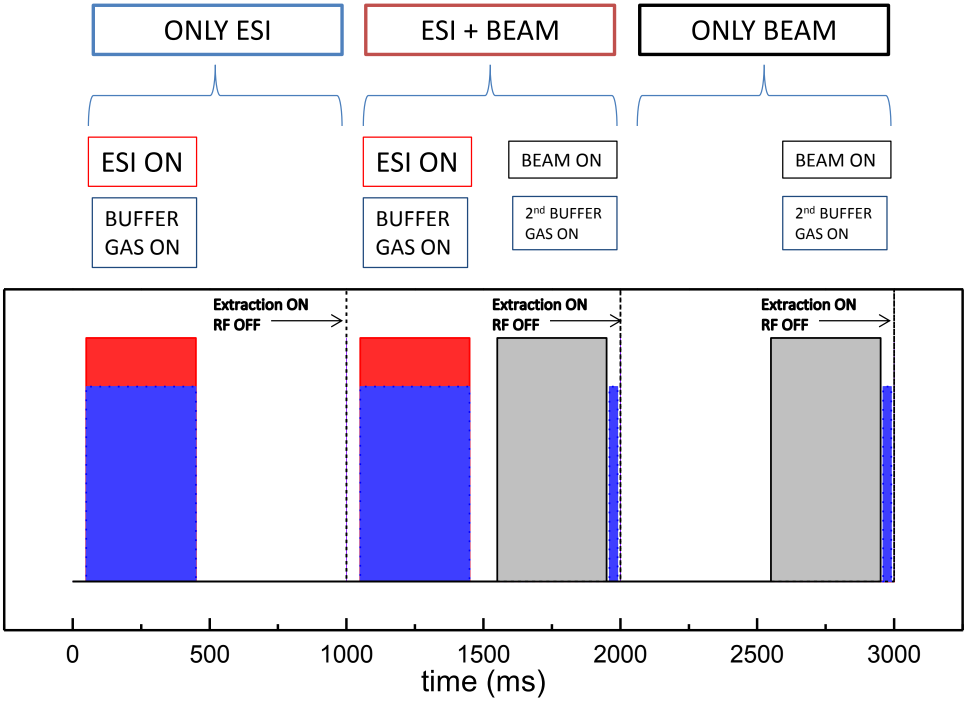

Figure 2.10: *Timing scheme for data acquisition. Three scans are performed, namely ONLY ESI (no irradiation beam), ESI + BEAM, and finally ONLY BEAM (see text).*

potential. The signal is stored by a 1 GHz digitizer (Ztec) for further analysis. When the extraction is completed, the RF of the ring electrode is switched on again and the DC voltage on the end caps is set to zero.

The m/z value of the ions can be derived from their time–of–flight (t_{TOF}) to the detector with the equation $m/z = (\frac{t_{TOF}-b}{a})^2$, where a and b are constants.

2.4 Data acquisition and analysis

The experiment is running in cycles of three as shown in Fig. 2.10. The pulses were provided by a digital pulse/delay generator (model 565, Berkeley nucleonics) which was controlled by a home–built LabVIEW application.

The initially empty trap is loaded with biomolecular ions for a time interval (ESI ON) typically between 50 ms and 1500 ms (shown in figure 2.10 for a loading time of 400 ms). A He–buffer gas pulse is simultaneously applied to collisionally cool the ions and allow for trapping. Ions remain in the trap until the extraction pulse is applied to the end cups, a couple

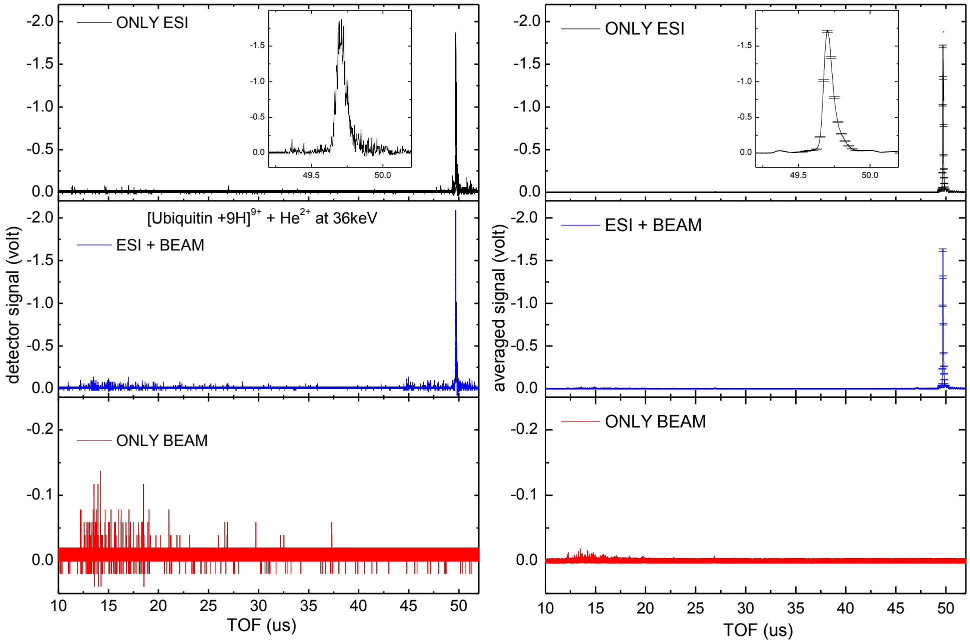

Figure 2.11: *Left: Example of time-of-flight data for a single acquisition cycle. Inset: zoom in the peak. Right: Average after 820 cycles.*

of μs after switching off the RF. The ionic trap content is then extracted towards the MS-TOF system for mass analysis and detection. The resulting (first) mass scan is labeled as ONLY ESI and is used to determine the initial number of ions in the trap.

For the second mass scan, the trap is again loaded using identical setting as before. Here, however, the content of the trap is irradiated by the ion or photon beam. A 100 ms delay between the end of the loading period and the beginning of the irradiation period allows for a reduction of the He pressure. Typical irradiation times depend strongly on the photon or ion flux and can range from 100 ms to few s. In case of photon or ion induced fragmentation, energetic fragment ions can be formed. These are collisionally cooled by a second (50 ms short) He-buffer pulse, applied a few tens of ms after the end of the exposure period. The ions are extracted from the trap and a second mass scan is recorded (ESI + BEAM).

Finally, for the third mass scan the trap is left empty. The ion or photon beam irradiates solely residual gas present in the trap chamber. The ionized content is extracted and a mass scan is recorded (ONLY BEAM).

The entire 3-step cycle is repeated typically for several hundred times until sufficient statistics and good signal to noise ratio are reached. In Fig. 2.11 a typical series of spectra is depicted.

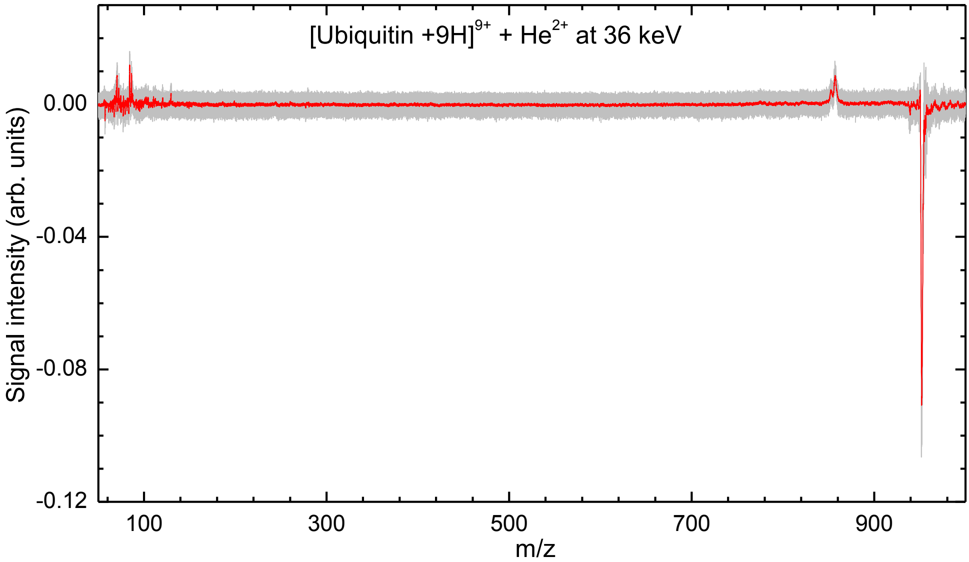

Figure 2.12: *Typical spectrum. The red signal is the result after applying a 17 points Adjacent-Averaging method.*

From these data the information of the net effect of the irradiation beam on the biomolecule ions can be obtained. The ONLY ESI and the ONLY BEAM spectra are subtracted from the ESI + BEAM spectrum as shown in Fig. 2.12.

2.5 Multicharged keV ion beams

An electron cyclotron resonance ion source (ECRIS) was used to produce the projectile ions for the keV ion induced dissociation (KID) studies presented in chapter 3. The source is located at the KVI ZernikeLEIF facility (Groningen, The Netherlands) [23]. The ECRIS can provide intense beams of atomic and molecular keV multiply charged ions.

The principle of operation of ECRIS is the ionization of atoms by electron impact in a plasma that contains electrons, atoms and ions. The plasma is confined in a *magnetic bottle* [24]. This configuration is produced from the superposition of an axial magnetic field generated by two coils and a radial magnetic field produced by a permanent hexapole magnet (see Fig. 2.13). The field strength at the center of the bottle is minimum and increases as function of the distance from the center. Electrons in the magnetic bottle revolve around the magnetic field lines with their cyclotron frequency given by $\omega_B = \frac{eB}{m_e}$. An RF field in the microwave region (14 GHz) is coupled into the plasma chamber, to heat the electrons. When the cyclotron frequency ω_B equals the RF frequency ω_{RF}, energy is transferred from

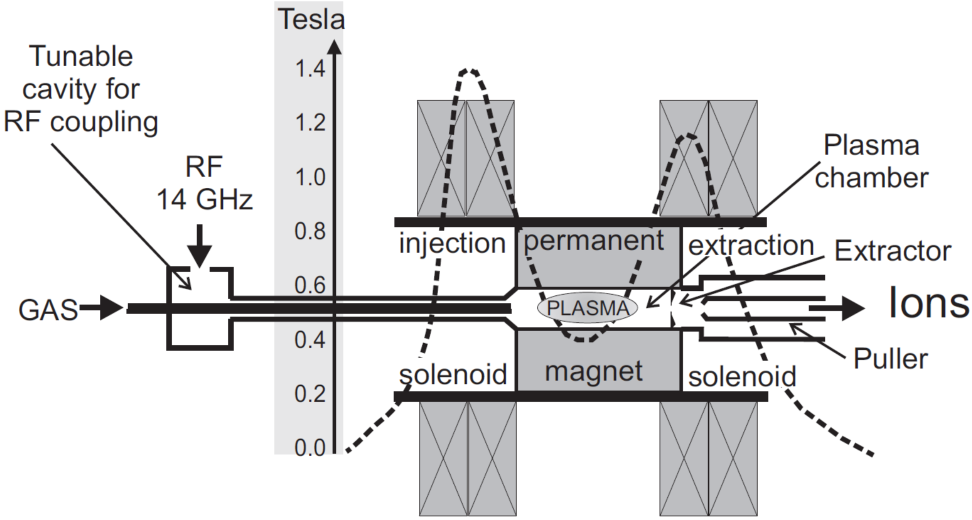

Figure 2.13: *Schematic view of ECRIS (see text).*

the RF field to the electrons. When sufficiently accelerated, these electrons ionize neutrals or previously ionized ions. Highly charged ions are the direct result of series of multiple electron impact events.

The whole source is floated on a high voltage V_S between few kV and 25 kV. An electrostatic electrode is used to extract ions from the magnetic bottle into the beamline, operating at ground potential. The ion kinetic energy in keV therefore is $E = V_S \times q$, where q is the charge state of the ions. A 110° dipole magnet produces a magnetic field that deflects the desired beam according to the relation $B^{110^\circ} = C\sqrt{V_S \times A/q}$, where A is the mass of the ion and C is a constant value. The nominal A/q resolution of the magnet is slightly better than 1%. The typical intensities of the ion beams we used were somewhere between hundreds of nA to tens of μA. The ion beam is transported further by means of two triplets of quadrupole magnets along a central beam line and deflected to the Paultje setup by a 45^o magnet.

The projectile ions are eventually focused towards the center of the Paul trap by an Einzel lens that is located between the 45° magnet and the trap. A long tube with a small diaphragm is installed between the Einzel lens and the trap, in order to prevent secondary electrons and scattered ions from entering the trap. The ion beam intensity is measured by a Faraday cup behind the Paul trap, with typical ion currents in the range of few hundreds of nA.

2.6 Synchrotron user facilities

Modern synchrotron facilities such as ALS (Berkeley USA), BESSY II (Berlin, Germany), ESRF (Grenoble, France), LNLS (Campinas, Brazil), MAX-lab (Lund, Sweden), PETRA (Hamburg, Germany), SPring-8 (Sayo, Hyogo Prefecture, Japan), etc. produce synchrotron light from the oscillation of ultrarelativistic charged particles in a undulator, a periodic structure of alternating dipole magnets. For an updated list of available synchrotron sources see Ref. [25].

The synchrotron light produced by such third generation facilities is characterized by a high flux and brilliance over a large range of frequencies, typically ranging from Terahertz to hard X-rays. Synchrotron radiation has interesting properties such as spatial coherence, control over the polarization and the possibility of slicing out temporal beam structures with pulse lengths down to picoseconds.

2.6.1 BESSY II

The storage ring BESSY II is a third generation synchrotron radiation source that provides 25% of the XUV–infrastructure in Europe [26]. Electrons are injected by a linear accelerator into the storage ring up to a maximal operational current of 300 mA and an energy of up to 1.72 GeV. The storage ring has a circumference of 240 m and contains a set of 11 permanent magnet undulators. These undulators provide ultrabright photon beams from the Terahertz to hard X-ray spectral range (energy range 6 meV - 150 keV). The light is produced with complete control of the polarization.

A small fraction of the electrons is lost from the ring due to collisions with background gas or by perturbations to the electron orbits. The half–life time of electrons in the ring is around 10 hrs, therefore the available photon flux for experiments decreases exponentially with time. BESSY II worked with a scheme of three injections per day, with ring currents of 300 mA right after injection and 150 mA before re-injection. In 2012, the storage ring was upgraded to the so called Top–Up mode of operation, in which regular injections at a rate of 0.1Hz keeps the electron current constant at a ring current of about 300 mA.

A total of 50 beamlines are attached to undulators and dipole magnets and available to (external) users. In this thesis, the BESSY beamlines U125–2 10m–NIM [27] and U49–2 PGM1 [28] were used, for which a brief description is presented.

The main components of beamline U125–2 10m–NIM are the quasi-periodic undulator U125–2 and the monochromator 10m–NIM. The undulator U125–2 consists of a periodic structure of magnets as shown in Fig. 2.14. The full undulator counts 32 periods each 125 mm long. The movable gap distance between the magnets is used to tune the photon energy distribution that comes out from the undulator. Variation of the gap allows for generation of photons ranging in energy from 20 to 500 eV with a flux of up to 5×10^{12} ph/s. The minimal

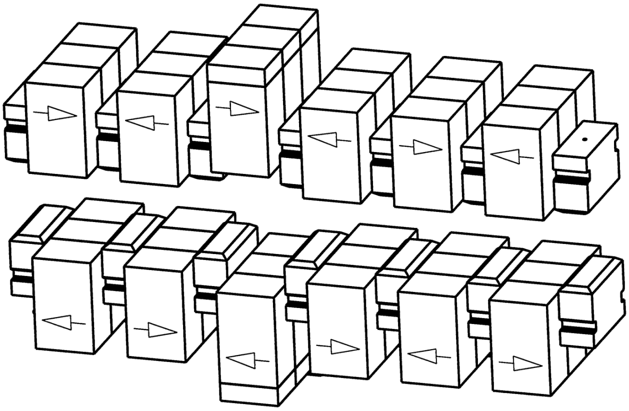

Reprinted from Nucl. Instr. and Meth. A, Vol 467–468, J. Bahrdt, et al., A quasi-periodic hybrid undulator at BESSY II, 130., Copyright (2001), with permission from Elsevier.

Figure 2.14: *Mechanical layout of a quasic-periodic structure in undulatour U125–2. Note the dislocation on the pattern of periodic magnets which helps to red shift high harmonics and avoid contamination of the photon beam through the monochromator (see text).*

gap is 15.7 mm. The beam produced by the undulator reaches off–Rowland Circle Normal Incidence Monochromator (NIM) consisting of an entrance and exit slit and a spherical grating with a 10 m focus [29]. The monochromator is equipped with a set of gratings with different lines/mm and thus different resolving power. We used the lower resolution gold coated 300 l/mm grating in order to get the maximum photon flux. Two toroidal mirrors are used for the final alignment and focusing of the beam into the Paul trap.

Experimental data can be contaminated by the higher harmonic photon beams produced by the undulator. As its name suggest, these higher harmonics have energies that are multiples of the fundamental energy of the undulator. They can affect the data if they pass through the monochomator together with the first harmonic. To solve this problem, the undulator was designed to have a quasiperiodic magnetic structure configuration that slightly red shifts the energy of the harmonics, ensuring that they are efficiently blocked by the monochromator [27]. For example, at 11 eV the flux ratio Φ_n/Φ_1 for the higher harmonics of a periodic versus the quasi-periodic design are reduced from 0.08 to 0.03 for n=2, from 1.6 to 0.3 for n=3, from 0.3 to 0.01 for n=4 and from 1.5 to 0 for n=5 [29].

For soft X rays, we used the beamline U49–2 PGM1 which has a photon energy range of 85 – 1600 eV and a flux of 10^{13} ph/s. The undulator here consists of 84 periods each 49.4 mm long with a minimal gap of 15.64 mm. The beamline monochromator is a plane grating monochromator (PGM). The available photon flux drops at the carbon K-edge energy range due to the strong absorption of carbon containing compounds in the mirrors and monochromator gratings in the beamline. To compensate the lower photon fluxes near the carbon K–edge, irradiation times were increased somewhere in between 1 to 3 s.

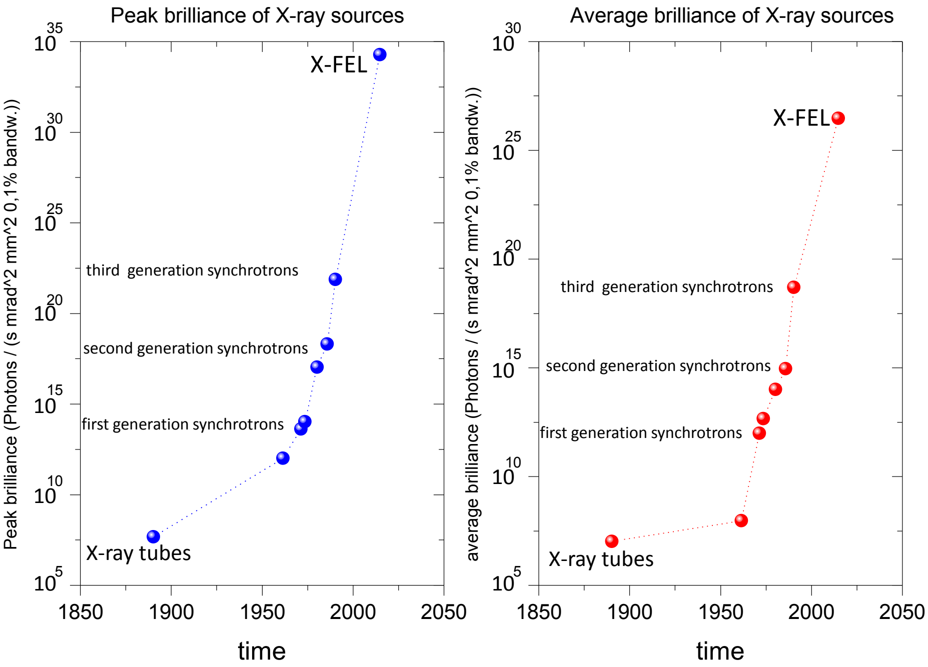

Figure 2.15: *Development of the brilliance of man-made X rays sources over time. Adapted from Ref. [32].*

2.6.2 MAX II

MAX II is a third generation synchrotron source located at MAX-lab. The storage ring has seven insertion devices along its circumference of 90 meter. A beam of electrons (300 mA) is injected at an energy of 400 MeV and then accelerated up to 1500 MeV. MAX II has 11 beamlines that provide user with synchrotron light from the ultraviolet to the hard X-ray spectral regime. The experiments were performed at the beamline I411 which has a photon energy range from 50 to 1500 eV [30, 31]. The photons are monochromatized by a Zeiss SX-700 plane grating monochromator.

2.7 FLASH

A free–electron laser (FEL) is a fourth generation synchrotron user facility with a peak and average brilliance which exceeds by several orders of magnitude any previous synchrotron or laser plasma source (see Fig. 2.15). Moreover, a FEL generates intrinsically short pulses of coherent light.

The Free–electron -LASer in Hamburg (FLASH) at DESY (Hamburg, Germany) was the world's first FEL facility for radiation in the extreme ultraviolet and soft X-ray range of the spectrum [32]. In a specific micro-macro pulse structure FLASH can deliver up to 5000 FEL pulses per second with an average FEL radiation power of 400 mW and ultra high intensities from 10^{12} to 10^{16} W cm^{-2} [33]. The photon flux is about 10^{13} photons per pulse with durations of 30-100 fs. Note that a typical photon flux by a storage ring synchrotron is 10^{13} photons per second. FLASH is driven by a 260 m linear accelerator equipped with seven TESLA-type 1.3 GHz superconducting accelerator modules where electrons are accelerated to a relativistic energy of 1.25 GeV.

The physical process behind the production of FEL pulses is the Self-Amplified Spontaneous Emission (SASE) [34]. Briefly, the FEL pulses are produced by a single pass of a bunch of electrons through a long undulator (length 30 m). If the undulator is long enough, the electron bunch starts to interact with its own radiation field leading to a charge density modulation within the bunch which produces a microbunching. This enhances emission of coherent radiation, which in turn enhances the microbunching process until saturation is reached. The power and coherence of the radiation increase exponentially in the process. Because the occurrence of coherent radiation in each bunch is stochastic (at the begin of the process only a small number of electrons is radiating coherently [34]) each FEL pulse differs in intensity, temporal structure and spectral distribution [32].

Our setup Paultje was interfaced to the beamline BL3 at FLASH for a study on (multi)-photon ionization of the multiply protonated protein Ubiquitin (M.W $\approx$ 8566 u). We used a FEL beam with a wavelength of the photons of 13.8 nm. As the intensity of each FEL pulse is different, the information for every single pulse energy was recorded. This value fluctuated typically between 9 and 14 μJ. For the experiment we used a split-mirror system of the group of Mosshammer (MPIK, Heidelberg) [35, 36]. The incoming FEL pulse is reflected by a spherical multilayer mirror (1-in. Mo/Si mirror, 50-cm focal length) that was cut into two identical mirrors. One of the mirrors is located at a fixed position whereas the other is mounted on a high–precision piezoelectric translational stage. Two reflections of the FEL pulse are obtained, one with a adjustable time delay with respect of the other one. The time delay can be set up to $\pm$ 2 ps at a resolution of better than 1 fs [36]. The two reflected pulses have approximate half of the incoming FEL pulse intensity in case of proper alignment. Asymmetric pulse distributions can be generated as well. Both pulses are focused to the center of the Paul trap located off-axis at a distance of 50 cm.

For the experiment described in Chapter 6 only one half-mirror was used. The FEL pulse intensity can be reduced upstream of the experimental setup, by using a Xe gas chamber attenuator and/or an aluminium filter. The FEL pulse intensity was typically attenuated by factors ranging from 0.97 to 0.22 for a Xe pressure from 4×10^{-4} to 2.5×10^{-2} mbar respectively.

BIBLIOGRAPHY

[1] Paul, W., Rev. Mod. Phys., **62**, 531 (1990).

[2] Bari, S., *The Influence of Peptide Structure on Fragmentation Pathways*, Ph.D. thesis, Kernfysisch Versneller Instituut, University of Groningen (2010).

[3] Yamashita, M. and Fenn, J. B., J. Phys. Chem., **88**, 4451 (1984).

[4] Yamashita, M. and Fenn, J. B., J. Phys. Chem., **88**, 4671 (1984).

[5] Cole, R. B., editor, *Electrospray Ionization Mass Spectrometry: Fundamentals, Instrumentation, and applications*, Wiley-Interscience (1997).

[6] Taylor, G., Proc. Roy. Soc. London A, **280**, 383 (1964).

[7] Dole, M., Mack, L. L., Hines, R. L., Mobley, R. C., Ferguson, L. D., and Alice, M. B., J. Chem. Phys., **49**, 2240 (1968).

[8] Wilm, M., Molecular & Cellular Proteomics, **10**, M111.009407. (2011).

[9] Ryce, S. A. and Patriarche, D. A., Can. J. Phys., **43**, 2192 (1965).

[10] Cahn, J. W., Phys. Fluids, **5**, 1662 (1962).

[11] Gomez, A. and Tang, K., Phys. Fluids, **6**, 404 (1994).

[12] Iribarne, J. V. and Thomson, B. A., J. Chem. Phys., **64**, 2287 (1976).

[13] Thomson, B. A. and Iribarne, J. V., J. Chem. Phys., **71**, 4451 (1979).

[14] Wilm, M. S. and Mann, M., Int.. J. Mass Spectrom., **136**, 167 (1994).

[15] Douglas, D. and French, J., J. Am. Soc. Mass Spectrom., **3**, 398 (1992).

[16] Julian, R. R., Mabbett, S. R., and Jarrold, M. F., J. Am. Soc. Mass Spectrom., **16**, 1708 (2005).

[17] Smith, R. D., Loo, J. A., Loo, R. R. O., Busman, M., and Udseth, H. R., Mass Spectrom. Rev., **10**, 359 (1991).

[18] Kelly, R. T., Tolmachev, A. V., Page, J. S., Tang, K., and Smith, R. D., Mass Spectrom. Rev., **29**, 294 (2010).

[19] Shaffer, S. A., Tang, K., Anderson, G. A., Prior, D. C., Udseth, H. R., and Smith, R. D., Rapid Commun. Mass Spectrom., **11**, 1813 (1997).

[20] Belov, M. E., Gorshkov, M. V., Udseth, H. R., Anderson, G. A., Tolmachev, A. V., Prior, D. C., Harkewicz, R., and Smith, R. D., J. Am. Soc. Mass Spectrom., **11**, 19 (2000).

[21] Inklaar, M., *An electrodynamic interface for an electrospray ionization setup*, Master's thesis, University of Groningen (2008).

[22] March, R. E., J. Mass Spectrom., **32**, 351 (1997).

[23] Drentje, A. G., Rev. Sci. Instrum., **74**, 2631 (2003).

[24] Hadjar, O., *Hidden sides of* C_{60}, Ph.D. thesis, University of Groningen (2001).

[25] Lightsources of the world, web, http://www.lightsources.org/regions (2013).

[26] Helms, I., Electron storage ring bessy, http://www.helmholtz-berlin.de/zentrum/gross/-geraete/elektronenspeicherring/index_en.html (2012).

[27] Bahrdt, J., Frentrup, W., Gaupp, A., Scheer, M., Gudat, W., Ingold, G., and Sasaki, S., Nucl. Instr. and Meth. A, **467–468**, 130 (2001).

[28] Sawhney, K., Senf, F., and Gudat, W., Nucl. Instr. and Meth. A, **467-468**, 466 (2001).

[29] Reichardt, G., Bahrdt, J., Schmidt, J.-S., Gudat, W., Ehresmann, A., Müller-Albrecht, R., Molter, H., Schmoranzer, H., Martins, M., Schwentner, N., and Sasaki, S., Nucl. Instr. and Meth. A, **467**, 462 (2001).

[30] Bässler, M., Forsell, J.-O., Björneholm, O., Feifel, R., Jurvansuu, M., Aksela, S., Sundin, S., Sorensen, S., Nyholm, R., Ausmees, A., and Svensson, S., J. Electron Spectrosc. Relat. Phenom., **101-103**, 953 (1999).

[31] Bässler, M., Ausmees, A., Jurvansuu, M., Feifel, R., Forsell, J.-O., de Tarso Fonseca, P., Kivimäki, A., Sundin, S., Sorensen, S., Nyholm, R., Björneholm, O., Aksela, S., and Svensson, S., Nucl. Instr. and Meth. A, **469**, 382 (2001).

[32] Tiedtke, K., Azima, A., von Bargen, N., Bittner, L., Bonfigt, S., Düsterer, S., Faatz, B., Frühling, U., Gensch, M., Gerth, C., Guerassimova, N., Hahn, U., Hans, T., Hesse, M., Honkavaar, K., Jastrow, U., Juranic, P., Kapitzki, S., Keitel, B., Kracht, T., Kuhlmann, M., Li, W. B., Martins, M., nez, T. N., Plönjes, E., Redlin, H., Saldin, E. L., Schneidmiller, E. A., Schneider, J. R., Schreiber, S., Stojanovic, N., Tavella, F., Toleikis, S., Treusch, R., Weigelt, H., Wellhöfer, M., Wabnitz, H., Yurkov, M. V., and Feldhaus, J., New J. Phys., **11**, 023029 (2009).

[33] Sorokin, A. A., Bobashev, S. V., Feigl, T., Tiedtke, K., Wabnitz, H., and Richter, M., Phys. Rev. Lett., **99**, 213002 (2007).

[34] Lindblad, A., Svensson, K., and Tiedtke, K., *A compendium on beam transport and beam diagnostic methods for Free Electron Laser*, Technical report, EuroFEL (2011).

[35] Jiang, Y. H., Rudenko, A., Herrwerth, O., Foucar, L., Kurka, M., Kühnel, K. U., Lezius, M., Kling, M. F., van Tilborg, J., Belkacem, A., Ueda, K., Düsterer, S., Treusch, R., Schröter, C. D., Moshammer, R., and Ullrich, J., Phys. Rev. Lett., **105**, 263002 (2010).

[36] Jiang, Y. H., Pfeifer, T., Rudenko, A., Herrwerth, O., Foucar, L., Kurka, M., Kühnel, K. U., Lezius, M., Kling, M. F., Liu, X., Ueda, K., Düsterer, S., Treusch, R., Schröter, C. D., Moshammer, R., and Ullrich, J., Phys. Rev. A, **82**, 041403 (2010).

Chapter 3

Fragmentation of protonated oligonucleotides by energetic photons and C^{q+} ions

The ionization and fragmentation of trapped protonated dGCAT oligonucleotides upon interaction with energetic photons ($h\nu$ = 10 eV - 570 eV) and keV C^{q+} ions was investigated by means of time-of-flight mass spectrometry. The observed fragmentation patterns are dominated by protonated and non-protonated nucleobase ions and fragments of the deoxyribose moiety. Fragments exceeding the size of nucleosides are almost completely absent. Absorption of VUV photons as well as interaction with keV ions predominantly involves ionization or excitation of molecular valence electrons and accordingly the observed fragmentation patterns exhibit qualitatively similar features. Soft X-ray induced ionization of core level electrons accompanied by subsequent emission of an Auger-electron shifts the fragment distributions towards smaller masses. This systematic study allows for first insights into differences and similarities between ion and photon induced excitation and fragmentation mechanisms. In particular, the crucial role of the deoxyribose moiety for radiation induced DNA damage that was predicted on basis of gas-phase experiments using isolated deoxyribose molecules is confirmed.

---

based on:
O. González-Magaña, M. Tiemens, G. Reitsma, L. Boschman, M. Door, S. Bari, P. O. Lahaie, J. R. Wagner, M. A. Huels, R. Hoekstra, and T. Schlathölter,
Phys. Rev. A 87, 032702 (2013)

3.1 Introduction

Most biological effects of ionizing radiation are triggered by direct and indirect DNA damage. The latter is mainly due to DNA interaction with free radicals from radiolysis of nearby water molecules. Direct damage to DNA is induced either by the primary quanta of radiation themselves or by secondary particles such as electrons and ions. A typical experimental approach to assess direct and indirect effects is the irradiation of plasmid DNA in solution with X-rays or fast ions and subsequent detection of single or double strand breaks [1–3]. Indirect damage can be quenched to a large extent by the addition of radical scavengers [3–5]. Low-energy electrons and (sub-)keV ions have a very short penetration depth and, therefore, their potential to induce strand breaks is most often studied using plasmid DNA deposited onto surfaces [6–10]. Sophisticated analytical techniques such as X-ray photoelectron spectroscopy allow for going into more detail and to investigate chemical DNA modifications e.g., dehydrogenation and oxygen loss [11]. However, the assignment of such reaction pathways to a particular damage mechanism remains ambiguous because of the interplay of direct and indirect damage.

The most straightforward approach to single out the direct effect is using molecular DNA building blocks in the gas phase. Gas-phase targets of these molecules are relatively easily produced by means of evaporation from an oven. Over the last decade, many studies have focused on molecular ionization and fragmentation dynamics upon interaction with energetic photons [12, 13], low energy electrons [14, 15] and keV ions [16–20]. It was observed that amongst the small DNA building blocks deoxyribose molecules are particularly sensitive to irradiation. They disintegrate completely upon ionization by electrons [21], photons [13] and keV ions [22, 23]. For keV ion impact, theoretical efforts have until now focused on determination of ionization and electron capture cross sections, e.g. in proton [24, 25] and C^{q+} [26, 27] collisions with nucleobases.

With the wealth of existing data on the response of gas-phase DNA building blocks to interaction with energetic ions or photons, it is important to know in how far these results can help understanding the response of an entire strand of gas-phase DNA. Are gas-phase oligonucleotides most prone to dissociation at the sugar moieties whereas the nucleobases are more stable? Do known breakup channels of isolated building blocks show up in the fragmentation pattern of the much larger macromolecule?

A first hint came from experiments on keV ion induced fragmentation of nucleobases or amino acids in a cluster. In the cluster environment, new fragmentation channels open up that are closed for isolated molecules [28, 29]. The structure and composition of homomolecular clusters differs still strongly from the one of DNA strands. Intermediate molecular systems such as nucleotides and oligonucleotides (cf. Fig. 3.1) are more appropriate to use as test beds bridging the gap between DNA and its smallest molecular building blocks. However, nucleotides and oligonucleotides already decompose thermally upon very moderate heating.

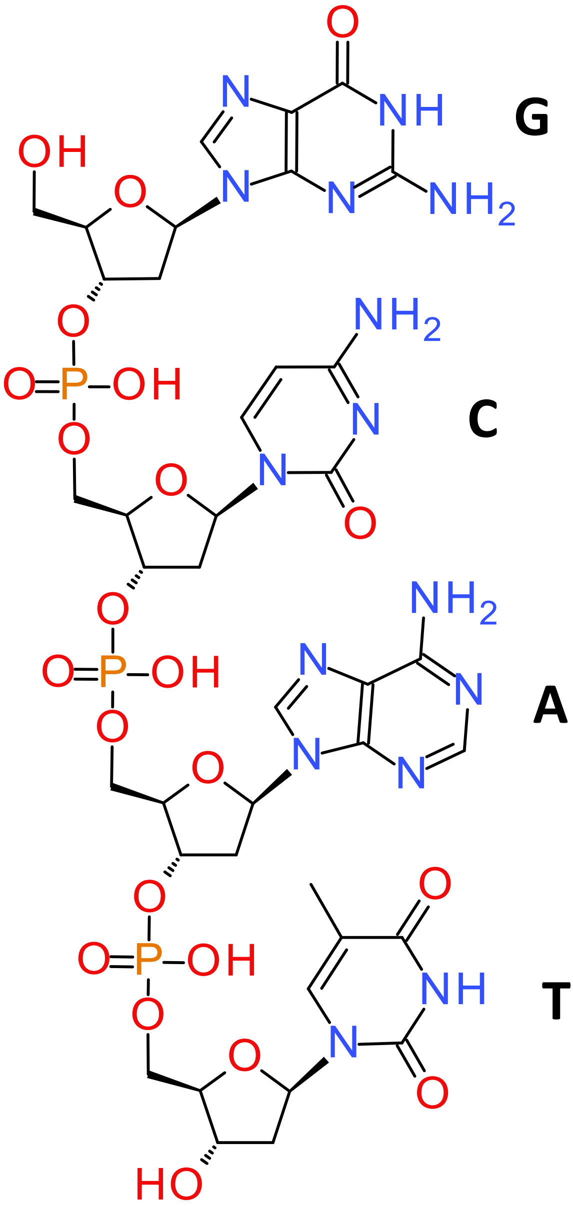

Figure 3.1: *The structure of the oligonucleotide dGCAT. The letters G, C, A and T label the nucleobases guanine, cytosine, adenine and thymine, respectively.*

To bring these species into the gas phase, it is necessary to employ electrospray ionization, laser desorption or similar advanced techniques. The target densities that can be achieved by these techniques are usually much lower than those obtained by evaporation of for example the nucleobases. To circumvent this target-density problem it is possible to take the opposite route and study energetic collisions of electrosprayed oligonucleotide anions with a gas target of neutral noble gas atoms [30]. Collision experiments of this type have for instance shown that nanosolvation of the nucleotide adenosine 5-monophosphate can efficiently quench collision-induced fragmentation of the embedded molecule [31]. A limitation of this type of collision studies is, that only relatively low collision energies can be reached in the center of mass system and therefore, only very moderate amounts of excitation energy can be deposited in the biomolecule.

We have therefore chosen to investigate the impact of keV C^{q+} ions and energetic photons on protonated tetranucleotides with sequences dGCAT (for a sketch of the structure, see Fig. 3.1) and dGTAT, stored in a radiofrequency trap. In the following we will present the resulting fragmentation patterns. The yields of the various dissociation products recorded as a function of photon energy and ion charge state q will be interpreted with emphasis laid on the role of DNA building blocks in comparison to their dissociation dynamics as free molecules.

3.2 Experiment

The photoionization experiments presented in this work have been carried out at the synchrotron beamlines MAXlab i411 (Lund, Sweden [32]) and BESSY II U125/2-NIM (Berlin, Germany, [33]). The ion-induced fragmentation experiments were performed at Zernike-LEIF facility at the KVI (University of Groningen, The Netherlands).

Briefly, an in-house built electrospray ionization (ESI) source was used to spray a 40μM solution of the oligonucleotides dGCAT (DNA technology, Risskov, Denmark) solvated in a mixture of 80% methanol, 20% water and with 0.5% formic acid under atmospheric conditions. The ESI beam was then expanded into a first vacuum chamber housing an RF ion funnel for phase space compression. After further phase space compression in a quadrupole RF ion guide, the cations entered a RF quadrupole mass filter, where selection of the doubly protonated oligonucleotides $[\text{dGCAT} + 2\text{H}]^{2+}$ or $[\text{dGTAT}+2\text{H}]^{2+}$ took place. These dications were then transferred into a 3D RF-ion trap (base pressure: $p \approx 1 \times 10^{-8}$ mbar) and accumulated to reach sufficient target density.

For collisional cooling of the protonated oligonucleotides, a He buffer gas pulse was applied. At typical operating conditions, the cooled target had a 300 μm diameter and contained a few 1000 protonated oligonucleotides. The typical target number density was thus of the order of 10^8 cm^{-3}. To determine the mass distribution of the RF-trap content, the cations were then extracted into a linear time-of-flight (TOF) mass spectrometer ($M/\Delta M \approx 200$) by applying bias voltages of about ± 200 V to the RF-trap endcaps for 5 μs.

The RF-trap was typically filled for about 1s. A time interval of 100 ms allows for the buffer-gas pressure to decrease before exposure to ions or photons is started. Depending on photon or ion flux, exposure times between 150-2000 ms were typically chosen such that less than 10% of the trap content was ionized. This way it was ensured that not more than 10% of the trapped protonated oligonucleotides underwent multiple interaction processes. Subsequently, an additional short buffer gas pulse (50 ms) was applied, to cool down energetic fragmentation products. To compensate for contributions of residual gas, from each acquired spectrum, a subsequent second mass-scan obtained under identical conditions but with an empty trap was substracted. As a reference for the trap content, eventually a mass scan of the native trap content without ion/photon exposure is also substracted. Typically, this sequence of three mass-scans is repeated 500-1000 times, to accumulate sufficient statistics.

For photon energies between 10 and 30 eV, the setup was interfaced with the BESSY II U125/2 beamline: Photons were generated in a quasi periodic undulator consisting of 32 dipole magnet periods each 125 mm long, in combination with a 10 m focal length normal incidence monochromator (NIM [33]). For maximum photon flux of $\approx 10^{13}$ photons/s, a relatively low resolution 300 lines/mm grating was employed. For the soft X-ray photoabsorption studies, we used the MAXlab i411 beamline. Here, the undulator consisted of 43 dipole magnets of 59 mm length. A modified SX-700 monochromator equipped with a 1220 lines/mm grating delivered a flux typically exceeding 10^{12} photons/s. The photon flux was determined using a SXUV-type silicon p-n junction photodiode (IRD, Newbury Park, USA) and the exposure time was controlled using a mechanical shutter with a 14 mm aperture (Uniblitz, Rochester, USA). For the ion induced fragmentation studies, the setup was interfaced to the Zernike-LEIF keV ion beamline. The ion current was measured using a Faraday cup with typical currents in the nA regime. Exposure time was controlled by means of an electrostatic deflection field in the keV ion beamline.

For keV ions, the RF-trap potentials strongly affect the ion-beam profile within the trap. Part of the broadened beam may miss the trapped molecules. To compensate for reduced beam overlap we normalized the mass spectra obtained at different ion energies to the loss of $[\text{dGCAT+2H}]^{2+}$ cations from the trap. Throughout this article, for the cases of keV ion collisions, fragment ion yields are thus always *relative* with respect to the total ionization cross section. For photons the beam profile only varies with photon energy but stays an order of magnitude smaller than the diameter of the target volume. The loss of parent ions from the trap together with the absolute photon flux can thus be used to determine relative total photoabsortion cross sections as function of photon energy.

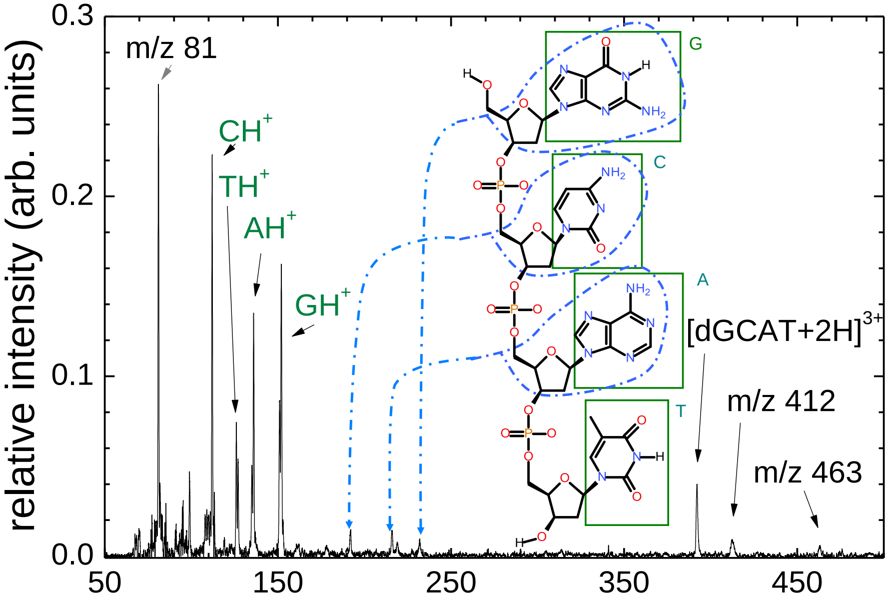

Figure 3.2: *Mass spectrum of interaction products from 40 keV C^{4+} collisions with [dGCAT+2H]$^{2+}$. The intensity was normalized to the total loss of the parent peak after irradiation.*

3.3 Results

In the following, mass spectra and fragment ion yields from (dGCAT+2H)$^{2+}$ interactions with keV ions or energetic photons will be presented.

3.3.1 C^{q+} ions at keV energies

Fig. 3.2 displays a mass spectrum of the cationic products obtained after collisions of 40 keV C^{4+} with [dGCAT+2H]$^{2+}$ (keV ion induced dissociation, KID). The latter has a monoisotopic mass of 1175.2 amu, i.e. the parent ion is found at m/z 587.6 amu. A clear peak due to [dGCAT+2H]$^{3+}$ is an evidence for non-dissociative electron capture from the oligonucleotide dication. However, the spectrum is dominated by intense peaks in the low-mass range from m/z 60 to 160 (note that ion with masses below 60 were not trapped). The strongest peak at m/z 81 is likely to be mainly due to a $C_5H_5O^+$ fragment from the sugar moiety in the dGCAT backbone (see discussion below). The next four peaks are actually doublets due to protonated nucleobase cations [C+H]$^+$ (cytosine, m/z 112), [T+H]$^+$ (thymine, m/z 127), [A+H]$^+$ (adenine, m/z 136) and [G+H]$^+$ (guanine, m/z 152) and their non-protonated coun-

mass over charge ratio	assigment	KID				photons						
		C^{5+}	C^{4+}	C^{3+}	C^{2+}	40	250	300	330	415	430	570
	deoxyribose related											
69	C_4H_5O	–	–	–	–	6.8	12.7	8.1	22.8	15.3	13.5	7.1
81	C_5H_5O	17.3	25.1	20.1	22.5	61.5	54.6	37.4	176	124	74.6	44.8
82		–	2.5	2.9	2.5	23.2	5.9	3.3	22.6	10.5	10.7	5.8
99	$C_5H_7O_2$ (5′)	1.3	1.8	1.7	1.4	6.1	9.4	5.1	22.2	13.2	12.5	6.3
	nucleobase related											
112	(C+H)	11.4	17.8	9.1	13.3	55.3	33.8	19.1	55.8	38.6	35.6	21.0
126	T	1.9	5.7	1.0	1.3	4.6	3.3	2.4	4.7	2.8	2.5	1.7
127	(T+H)	0.3	4.1	0.1	1.7	8.7	8.4	5.9	15.8	13	11.4	7.3
135	A	2.6	4.1	3.4	3.8	4.5	9.4	4.6	21.9	15.2	13.6	8.9
136	(A+H)	6.8	10.4	5.5	8.3	31.6	24.4	14.6	44.3	31.7	28.4	17.8
151	G	4.0	7.5	3.3	3.3	17.1	13.2	8.7	21.1	15.8	13.7	9.4
152	(G+H)	7.8	13.7	8.4	7.6	46.2	23.6	14.0	48.9	13.5	17.1	14.2
83	C_4H_5NO, $h\nu \rightarrow$T [12], $H^+ \rightarrow$C [35]	0.5	3.5	3.9	–	–	5.0	3.0	16.3	2.6	6.7	4.5
95	$C_4H_5N_3$, $h\nu \rightarrow$C [36]	–	–	–	–	–	1.5	–	1.3	2.7	2.3	0.5
97	$C_4H_3NO_2$, $h\nu \rightarrow$T [12]	–	–	–	–	0.3	0.6	0.3	0.9	1.2	0.8	0.2
108	$C_4H_4N_4$, $h\nu \rightarrow$A [12], $C^+ \rightarrow$A [37]	0.8	1.6	1.6	1.6	–	3.5	2.4	3.5	8.6	5.4	2.9
109	$C_4H_5N_4$, $h\nu \rightarrow$G [36]	0.5	1.7	1.2	1.9	–	1.3	–	1.4	3.9	2.2	0.9
110	$C_4H_4N_3O$, $h\nu \rightarrow$G [36]	1.0	1.7	2.1	2.0	0.3	3.8	2.9	3.5	6.5	5.2	2.7
	nucleoside related											
192	C + sugar moiety	0.5	0.8	0.2	0.5	3.7	1.6	0.2	1.2	4.3	0.1	0.3
216	A + sugar moiety	0.6	0.9	0.3	0.9	5.6	2.0	1.8	4.6	1.6	1.8	1.9
232	G + sugar moiety	0.3	0.7	0.3	0.4	3.8	1.5	0.5	–	1.4	1.3	0.9
392	$(dGCAT+2H)^{3+}$	2.6	3.2	4.2	1.2	9.9	2.3	–	–	0.2	0.5	1.8

Table I: *[dGCAT+2H]*$^{2+}$ *fragments formed upon 40 keV C*$^{q+}$ *ion impact and photoabsorption (photon energies given in eV). Relative intensities are given in % of the loss of parent ions from the trap. All fragments are singly charged cations unless stated otherwise. Note, that m/z 81 and 82 have also been observed with relatively small yields as nucleobase fragments formed in VUV photofragmentation [12]. For m/z 83, 95, 97, 108, 109 and 110, only one of the possible assignments is given.*

terparts T^+, A^+, and G^+, with m/z 126, 135 and 151. C^+ (m/z 111) has negligible intensity. It is important to note, that the nomenclature can be ambiguous: The nucleobase fragments are formed by glycosidic bond cleavage, and therefore lack an H atom in comparison with their gas phase counterparts. What we call the non-protonated nucleobase cation B^+ and the protonated cation $[B+H]^+$ thus require addition of H and 2H, respectively.

Three peaks at m/z 192, 216 and 232 have been previously observed in collision induced dissociation (CID) studies [34] and were assigned to cyclic nucleoside complexes containing the 5 membered sugar ring and the nucleobases cytosine, adenine and guanine, respectively (see inset in Fig. 3.2). A few other larger fragments observed with very small relative intensities will be discussed in the photoionization context. The relative yields of all fragments are summarized in Table I.

Zooms in the most relevant mass region m/z 60 - 160 are displayed in Fig. 3.3 for 40 keV C^{q+} impact on $[dGCAT+2H]^{2+}$ and $q = 2 - 5$. For all q the splitting of the nucleobase-related peaks into a protonated and an non-protonated component is clearly visible for G, A and T. For C, A and G, the protonated cation is clearly stronger than the non-protonated one.

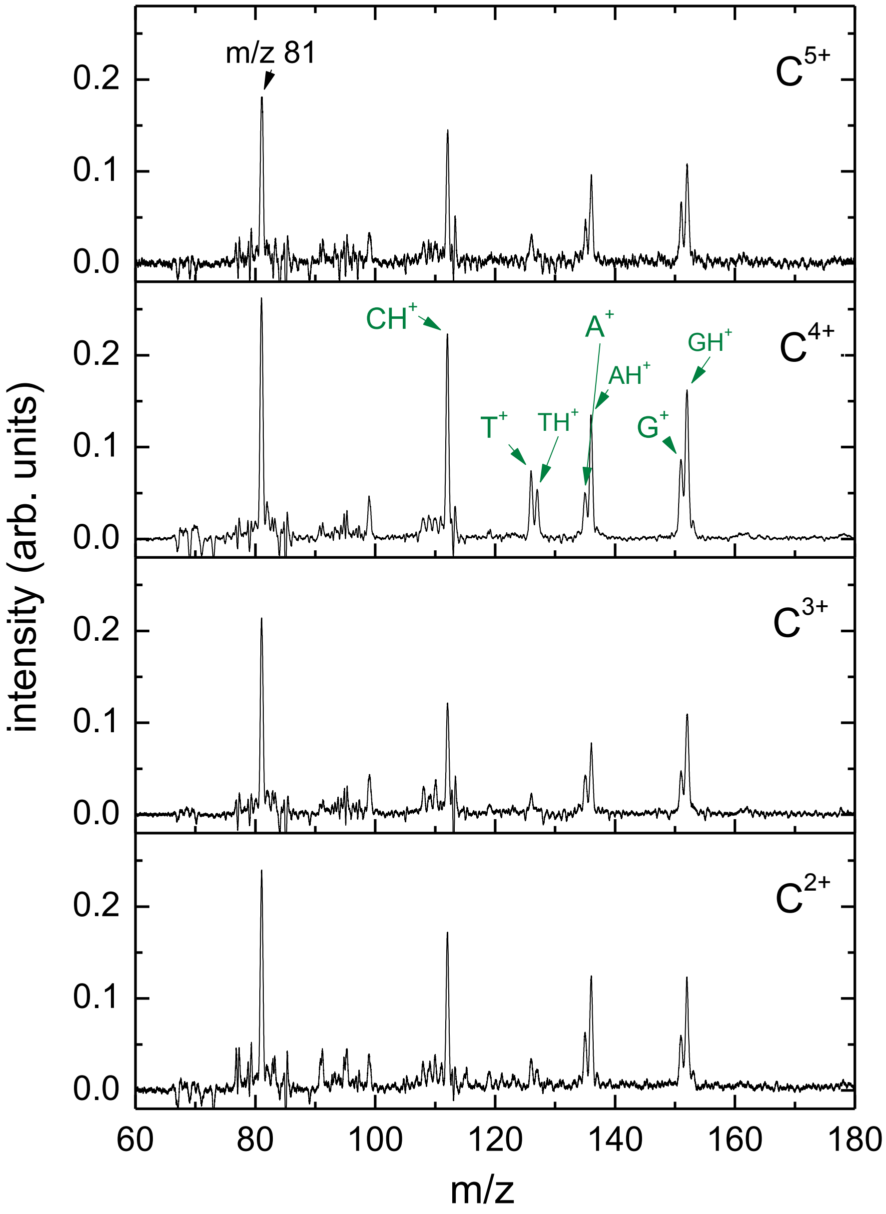

Figure 3.3: *Mass spectra of interaction products from 40 keV C^{q+} ($q = 2-5$) collisions with [dGCAT+2H]$^{2+}$.*

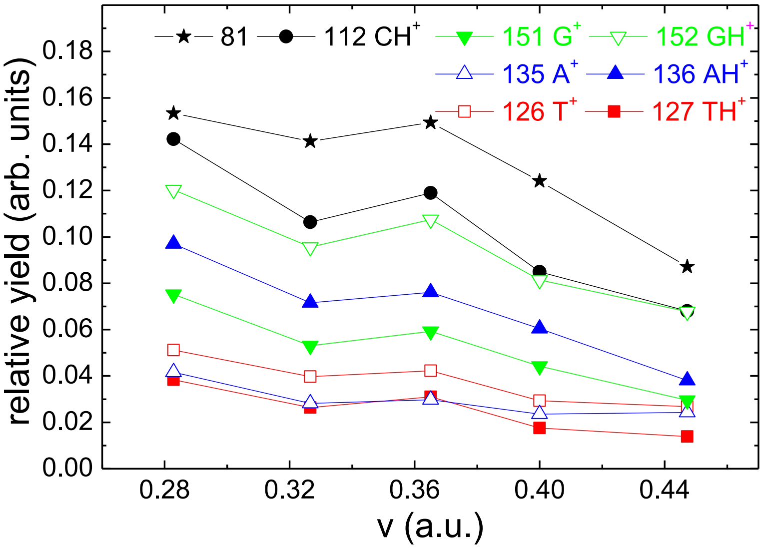

Figure 3.4: *Relative yields for protonated and non-protonated nucleobases and for the m/z 81 fragment for collisions of* C^{4+} *with [dGCAT+2H]*$^{2+}$ *as a function of ion velocity* v. *The error bars would not exceed the symbol sizes.*

For T, the opposite is observed. The relative intensities of the peak doublets vary strongly on q. The T peaks are always weakest and only have appreciable intensity for $q = 4$, whereas C is strongest for $q = 2-5$.

For C^{4+} projectile ions, Fig. 3.4 displays the integrated relative yields for the nucleobase fragments as a function of projectile velocity v in atomic units (a.u.). All fragment yields exhibit an obvious decrease with v, which reflects the well known fact that for keV ions impinging on DNA building blocks, molecular excitation due to electronic stopping increases with the velocity [22, 38]. The larger amount of excitation energy deposited in the molecule then leads to more extensive fragmentation and thus to a shift of the fragmentation pattern towards smaller masses. Because of the low-mass cutoff of the 3D-ion trap, this is manifest in the mass spectra as a relative increase of the m/z 81 peak. Interestingly, the different nucleobase yields decrease differently with v.

Figure 3.5 therefore displays the ratio between protonated and non-protonated cations of the nucleobases T, A and G as a function of ion velocity v. It is clear that for T, the degree of protonation is always lower than one and systematically decreases with v. For A, very high degrees of protonation are observed which depend only weakly on v. A strong v dependence is observed for G where the relative yields increase from 1.6 at $v \approx 0.28$ a.u. to 2.3 at $v \approx 0.45$ a.u..

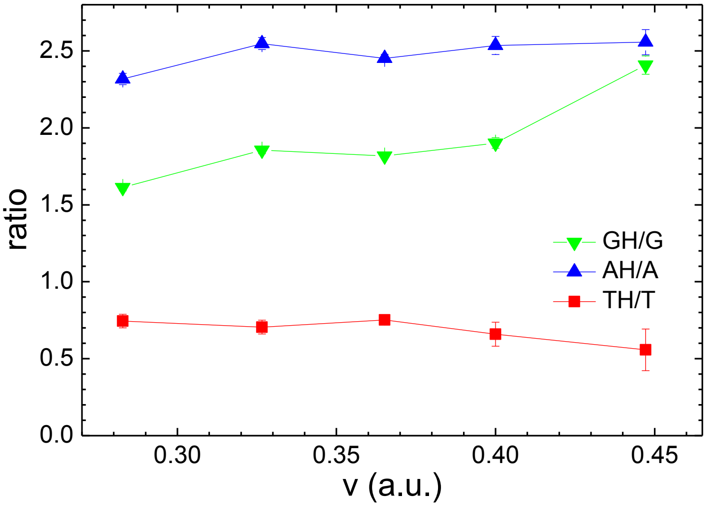

Figure 3.5: *Ratios between protonated and non-protonated nucleobase yields for T, A and G as a function of projectile ion velocity v.*

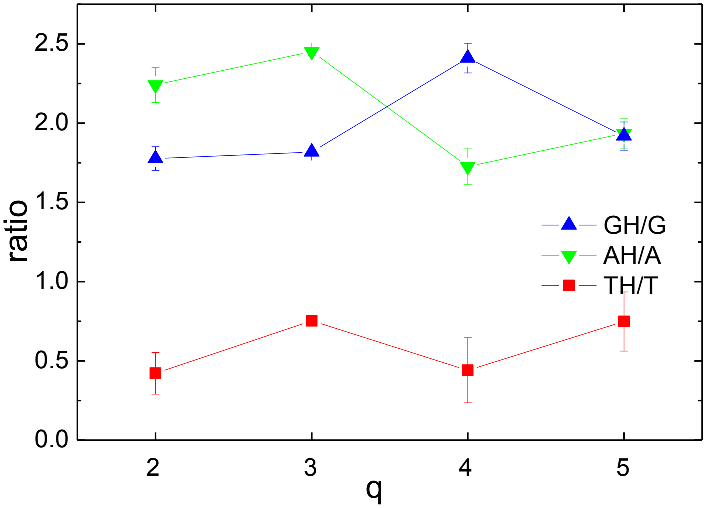

Figure 3.6: *Ratios between protonated and non-protonated nucleobases as a function of the* C^{q+} *charge state* q.

Finally, Fig. 3.6 shows the ratios between protonated and non-protonated nucleobase cations for constant v as a function of projectile charge state q. For $q = 2-5$, the ratios for T are consistently below 1 whereas for A and G, ratios around 2 are observed. For a given nucleobase, there is no apparent trend in the q-dependence.

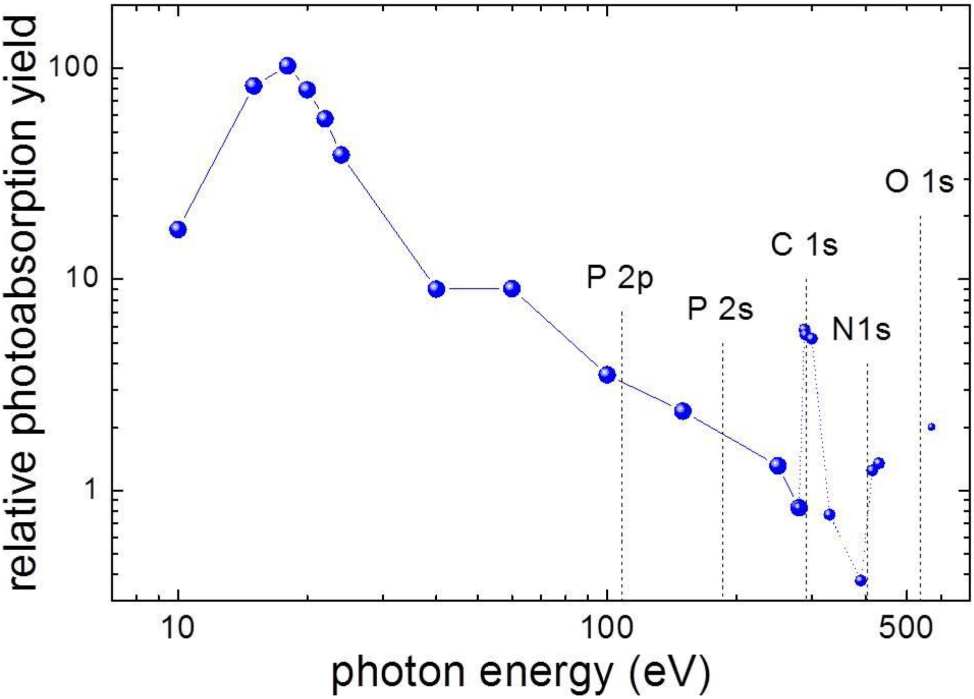

Figure 3.7: *Relative photoabsorption cross sections as function of photon energy for the oligonucleotide [dGCAT+2H]$^{2+}$. The error bars would not exceed the symbol sizes.*

3.3.2 Energetic photons

For the complementary photoionization studies, mass spectra were recorded at several photon energies ranging from 10 eV up to 570 eV covering the entire range from valence photoionization to C, N and O K-shell ionization.

Relative total photoabsorption cross sections as a function of photon energy can be directly obtained from the experimental data and are displayed in Figure 3.7. The maximum due to molecular valence electrons is observed between 15 and 20 eV in line with the findings for smaller biomolecules such as nucleobases [12]. The cross section then decreases with increasing photon energy until the K-edges of C, N and O are reached and the associated increase in cross section can be observed. To our knowledge, accurate 1s electron binding energies for gas-phase oligonucleotides, nucleotides and even nucleosides are unknown. For nucleobases values of 290.7-294.8 eV (C), 404.2-407.1 eV (N) and 536.5-537.5 eV (O) are predicted by theory [39].

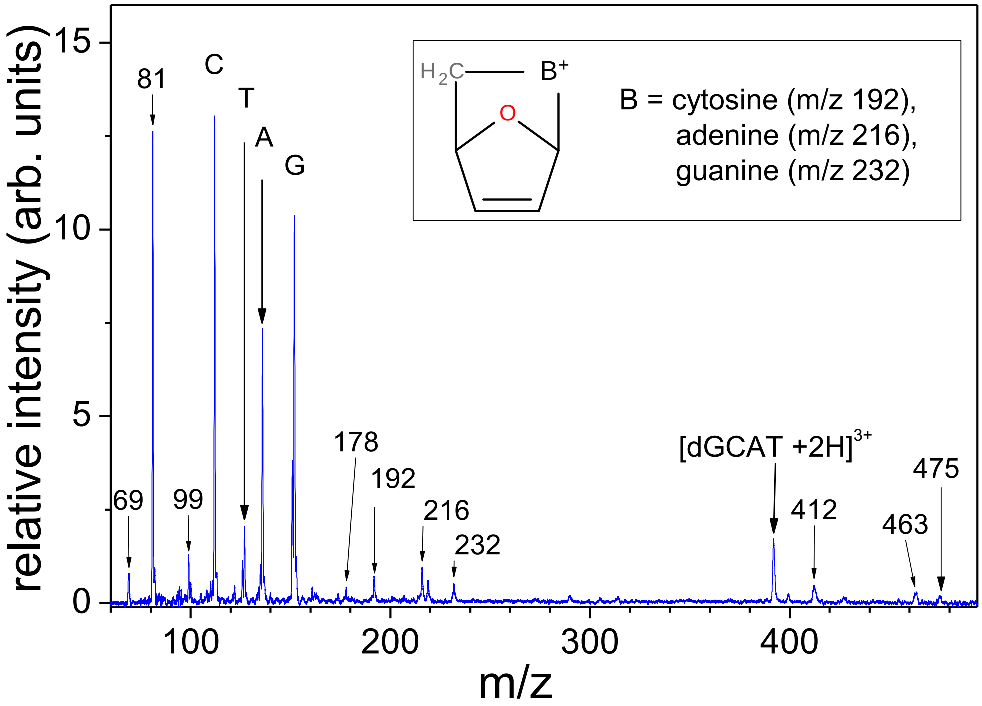

Figure 3.8: *Normalized mass spectra of molecular cations formed upon absorption of 40 eV photons in [dGCAT+2H]$^{2+}$. The insets show possible fragment structures (see text).*

Note that cross sections and mass spectra have always been recorded for photon energies clearly above the K-edge (330 eV, 415 eV, 430 eV, 570 eV) ensuring 1s ionization which is usually followed by an Auger de-excitation. Thus, two electrons are removed from [dGCAT+2H]$^{2+}$. Only for the C 1s, additional spectra have been recorded just below the K-edge (280 eV), in the 1s excitation regime (288.25 eV and 290 eV) and just above the K-edge (300 eV).

A [dGCAT+2H]$^{2+}$ photofragmentation spectrum obtained at 40 eV photon energy is shown in Fig. 3.8 and a list of most common fragments can be found in Table I. At this photon energy, essentially the same fragments are observed that are formed upon keV ion impact (see Fig. 3.3). The strongest peaks are again due to intact protonated and non-protonated nucleobases and the m/z 81 fragment, which is most likely due to $C_5H_5O^+$ from the deoxyribose moiety. Also the nucleoside complexes with m/z 192, 216 and 232 (containing C, A and G, respectively) can be clearly recognized (see inset in Fig. 3.3). A number of weaker peaks in Fig. 3.8 are found at m/z 69 (tentatively assigned to $C_4H_5O^+$), 178 (sugar moiety + phosphate group, $C_5H_7O_5P^+$), 219 (not assigned), 392 ([M+2H]$^{3+}$), 412 ([p+dA+p]$^+$, where p is the phosphate group moiety and dA stands for deoxyadenosine), 427 ([a_2 - C]$^+$ or a_3^{2+}), 463

(w_2^{2+}). Two larger fragments with relatively small yields are found at m/z 636 (not assigned) and 700 ($[a_3\text{-G}]^+$) (not shown in Fig. 3.8). Here, we follow the usual notation with a_i and w_j being ions containing the $5'$ and $3'$ terminus, respectively, formed by phosphodiester bond scission at the deoxyribose $5'$ carbon.

Figure 3.9 compares $[\text{dGCAT+2H}]^{2+}$ photofragmentation spectra obtained at photon energies of 15, 40, 330, 430 and 570 eV. In all spectra essentially the same fragment cations are formed. However, relative yields depend strongly on photon energy. At 15 eV the spectrum is dominated by the G and A doublets. C is a bit weaker and the m/z 81 fragment is very weak. The $[\text{dGCAT+2H}]^{3+}$ peak due to non-dissociative photoionization is more prominent than for C^{q+} ion impact. An increase in photon energy to 40 eV leads to strong changes in fragmentation pattern, which shifts to smaller masses. The m/z 81 peak becomes strong, non-dissociative ionization is reduced as are the intensities of the larger fragments. The nucleobase peak doublets are of comparable intensity as the m/z 81 peak. In contrast to the 15 eV case, at 40 eV C is strongest and T becomes visible. At 330, 430 and 570 eV, i.e. beyond the C, N and O K-edge, respectively, very similar fragmentation patterns are observed. Here, non-dissociative ionization is not observed anymore and larger fragments do not appear anymore. The m/z 81 peak dominates over the nucleobase doublets, which are clearly visible, again with C being strongest.

Figure 3.10 displays the photofragmentation yield for C, T, A and G in their protonated and non-protonated form as a function of photon energy. No sizeable yield of non-protonated C (m/z 111) is observed over the whole range. for all fragments, yields show a similar trend as the total photoabsorption cross section (Fig. 3.7) and the yields of the protonated species are always exceeding the respective non-protonated ones. However, clearly different slopes are observed when comparing protonated and non-protonated fragment cations. This is visualized in Fig. 3.11 where the ratio of protonated and non-protonated species as a function of photon energy is displayed.

3.4 Discussion

Nucleobases are dominating the fragmentation patterns for both, ions and photons. The following sections will therefore focus on the determination of the $[\text{dGCAT+2H}]^{2+}$ initial protonation sites. Subsequently, the yields of protonated and non-protonated nucleobase cations will be discussed in the context of photoionization and electron capture. The variation of the ratios between protonated and non-protonated nucleobase cations with photon energy, ion velocity v and ion charge state q will be examined with emphasis laid on excitation energies and timescales. Eventually, DNA damage involving nucleobase fragmentation or backbone scission will be discussed.

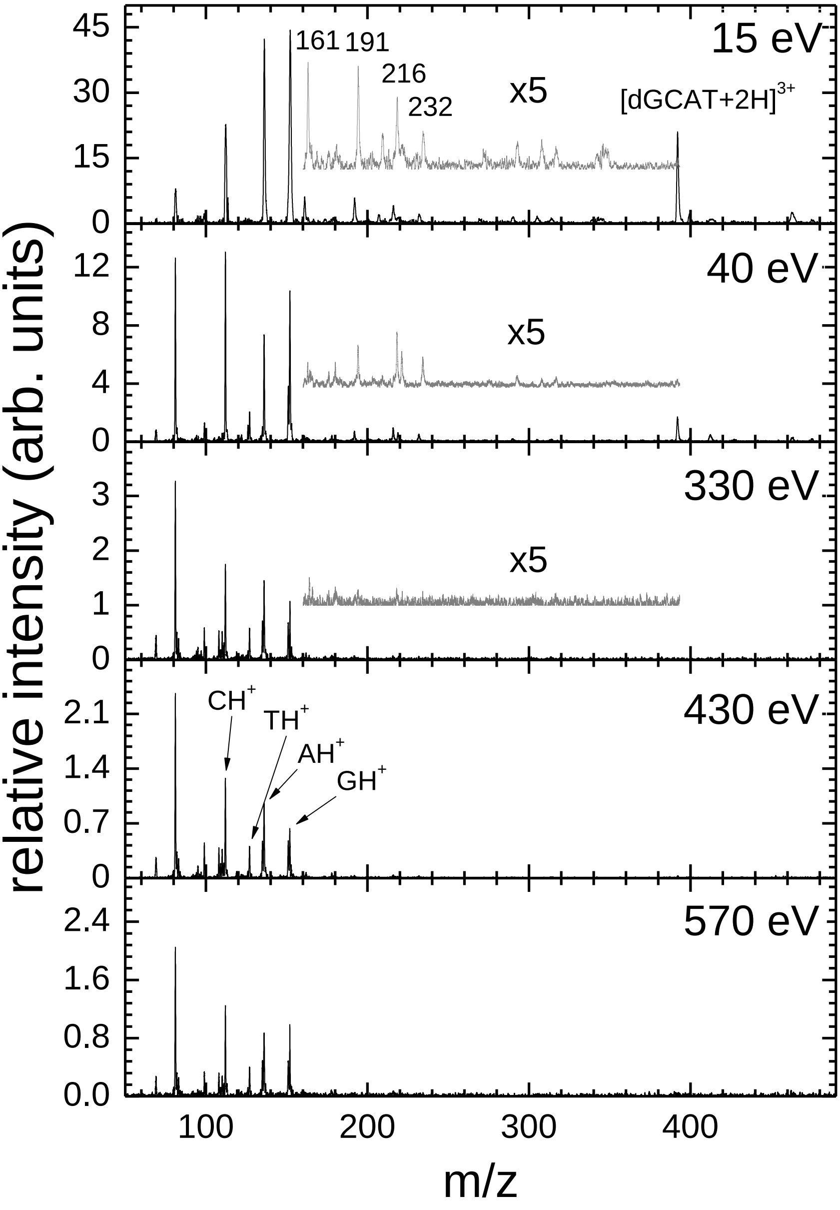

Figure 3.9: *Mass spectra of molecular cations formed upon [dGCAT+2H]$^{2+}$ photofragmentation at 15, 40, 330, 430 and 570 eV (for the peak assignments, see text).*

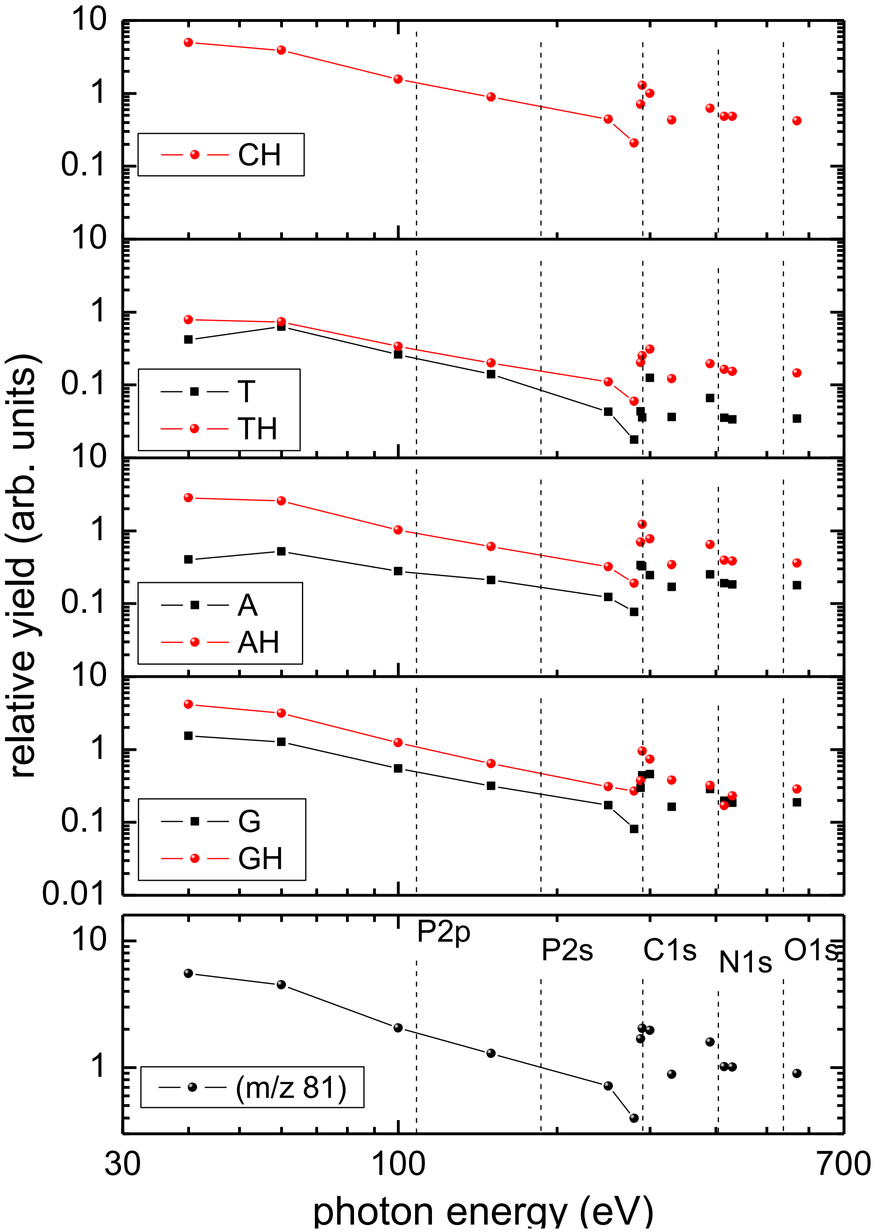

Figure 3.10: *Top 4 panels: Photofragmentation yields for protonated and non-protonated nucleobases. Bottom panel: The yield of the m/z 81 fragment. The error bars would not exceed the symbol sizes.*

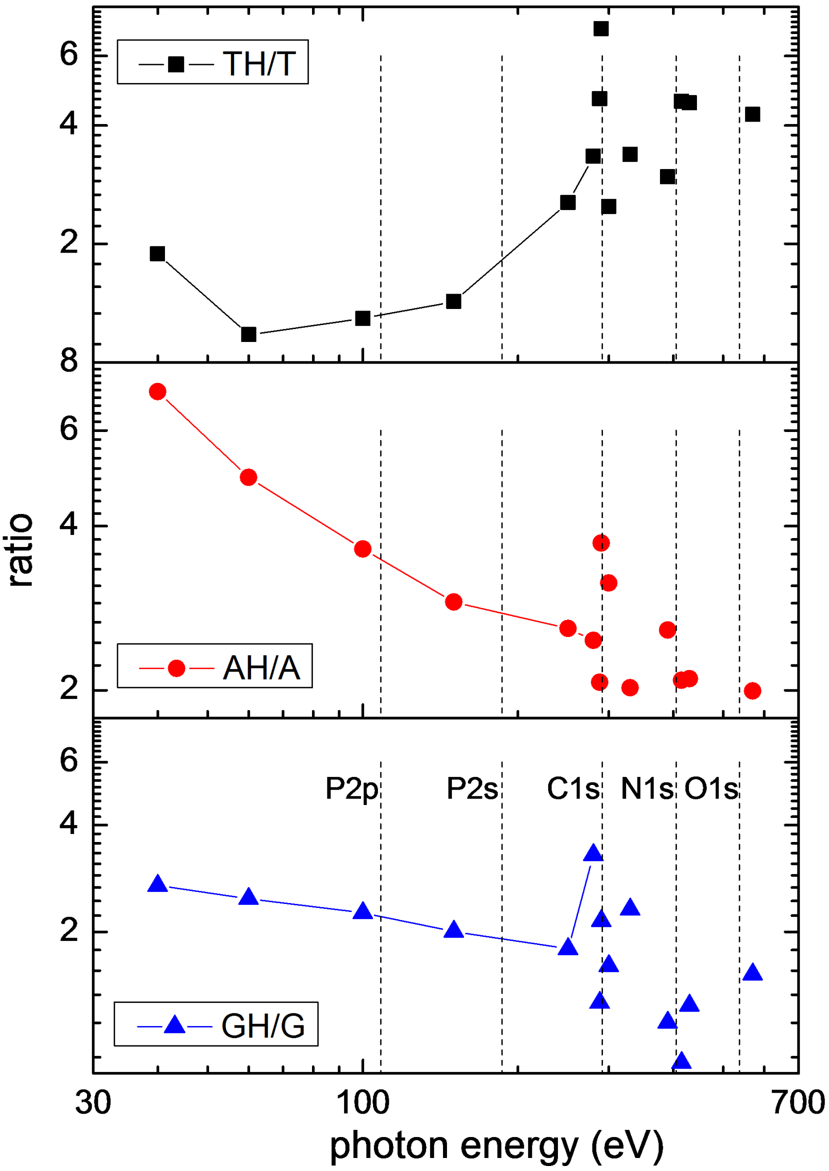

Figure 3.11: *Ratios between protonated and non-protonated nucleobase yields for T, A and G as a function of photon energy. The error bars would not exceed the symbol sizes.*

molecule	PA (kcal/mol)	$p\mathrm{K}_a$	vertical IE (eV)
DNA bases			
guanine G	229.3 [41]		8.26 [42]
cytosine C	227.0 [41]		8.89 [43]
adenine A	225.3 [41]		8.47 [43]
thymine T	210.5 [41]		9.19 [43]
nucleosides			
dG	237.9 [41]	2.9-3.3 [44, 45]	
dC	236.2 [41]	4.3-4.4 [44, 45]	
dA	237.0 [41]	3.8-4.1 [44, 45]	
dT	226.7 [41]	1.6	9.9 [44, 45]
deoxyribose (furanose)			10.06 [46] (t)
phosphate group	220-225 [47]	(2.1 for phospheric acid)	

Table II: *Proton affinities (PA), vertical ionization energies (IE) and logarithmic acid dissociation constants (pK_a) of various dGCAT building blocks. Where available, experimental values are given. Theoretical data are indicated with a (t). The values for the phosphate group are estimated from related compounds [47].*

3.4.1 Pathways to nucleobase fragment ions: the initial protonation site

For keV ion collisions as well as for absorption of energetic photons, the dominating dissociation products are protonated and non-protonated nucleobase cations C, T, A and G. In early low energy CID studies on various gas-phase protonated dinucleotides, Phillips and McCloskey [40] have investigated the formation of protonated nucleobase cations. The underlying fundamental process was found to be cleavage of the glycosidic bond between a sugar and a protonated nucleobase followed by a hydrogen transfer from the sugar to the base. Assuming a similar scenario for KID and photofragmentation, the most probable protonation sites of $[\mathrm{dGCAT+2H}]^{2+}$ need to be known to quantitatively understand the relative intensities of the nucleobase related cation yields.

For dGCAT, the approximate distribution of protonation sites over the nucleobases can be estimated using the pK_a values of the different nucleosides. The 0.5% solution of formic acid used for the ESI has a pH of about 2.3. With the $\mathrm{p}K_a$ values from Table II it follows that probabilities of protonation for C, A, G are about 100%, 90%, and 75% respectively, whereas thymine and phosphate group remain likely unprotonated.

We assume the protonation site ratio to be preserved upon transfer into the gas-phase [48] because of the higher proton affinities (PAs) of the four nucleobases as compared to the sugar or phosphate groups within the oligonucleotide. Table II lists gas-phase PAs of different DNA building blocks. The PAs for nucleobases are within a narrow range of $\approx$ 225-230 kcal mol^{-1} for A, C and G, while T has a substantially lower value of $\approx$ 210 kcal mol^{-1}. For the respective nucleosides, PAs are systematically larger but follow the same trend as the nucleobases. The higher PA of nucleosides as compared to the free bases is due to intramolecular hydrogen bonding between sugar and base and electron donating action of the sugar towards the base [47]. The PA value for the phosphate group is expected to lie in the range of 220-225 kcal mol^{-1} and clearly falls short of the nucleoside PAs.

Therefore, in the target [dGCAT+2H]$^{2+}$ ions, C is expected to be 100% protonated whereas T is 100% unprotonated. The second proton is expected either on A or on G with a preference for A. Exactly this order is found for photofragmentation over the whole range of wavelength under study (see Table I). Also in case of KID, protonated C has the highest yield whereas protonated T is almost negligible. However, here the order of A and G is reversed (see Table I and Fig. 3.4). In particular the low T yields are in line with CID studies: Vrkic *et al.* investigated all possible sequences of trimer oligonucleotides and several tetramers and found approximately equal yields for protonated C and G, slightly lower yields for protonated A and very low yields for protonated T [49]. Furthermore, in CID protonated bases from the 3′ residue are often more abundant than identical ones from the 5′ residue [40, 49]. For dGCAT investigated here, T is in the 3′ position but this clearly does not compensate for the high pK_a and low PA. We have performed CID control experiments on [dGCAT+H]$^{+}$ and [dGCAT+2H]$^{2+}$ using a liquid chromatography-MS/MS approach. The experiments confirm that for the singly protonated case, neither T^{+} or TH^{+} are formed whereas for [dGCAT+2H]$^{2+}$ traces of T^{+} nor TH^{+} are observed.

The suggested two-step pathway toward protonated nucleobase formation starting from a protonated nucleobase moiety is summarized in Fig. 3.12.

Ion impact or photoabsorption trigger the cleavage of the C-N glycosidic bond of a protonated site, leading to formation of the non-protonated nucleobase cations. In a slower process, the resulting N radical (homolytic cleavage) or anion (heterolytic cleavage) then abstracts an H radical or a proton, respectively, from the sugar moiety and a protonated nucleobase cation is formed. Clearly, this second pathway is only possible, if the initial cleavage process is sufficiently slow.

Since T is almost certainly not protonated in [dGCAT+2H]$^{2+}$, the formation of T^{+} (m/z 126) and TH^{+} (m/z 127) by either KID or photoionization must have a very different precursor than the formation of G^{+}, GH^{+}, CH^{+}, A^{+} and AH^{+}. The corresponding processes are sketched in Fig. 3.13 (a). For T, a hole localises on the sugar moiety, leading to rapid beta bond cleavage and release of a neutral (and thus undetected) thymine base (m/z 125), and a [dGCA+2H]$^{2+}$-sugar radical cation, which can form by O-C5' bond scission from the sugar. The remaining sugar radical cation can dissociate, leading to the observed fragments m/z 69, 81, and 99. The remaining [dGCA+2H]$^{2+}$ ion (m/z 475) is observed as

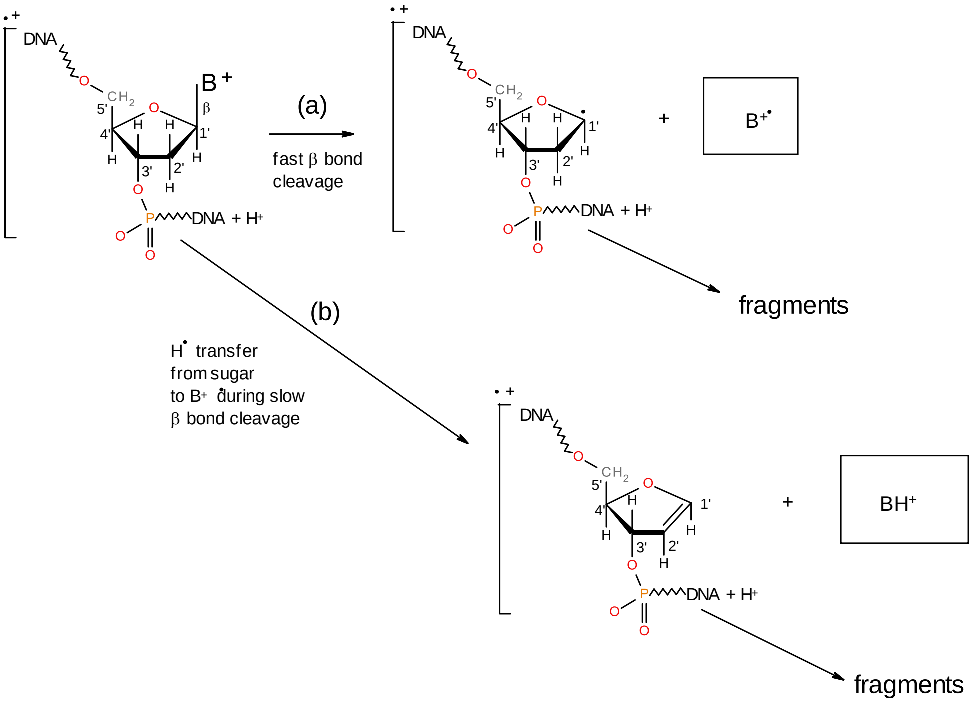

Figure 3.12: *Pathways from a protonated nucleobase towards formation of non-protonated and protonated nucleobase cations. Here, B=G, C, or A. However, in [dGCAT+2H]$^{2+}$, for B=G, the C5' DNA residue is actually just an OH. The B moieties are formed after scission of the glycosidic bond and thus lack an H. B$^{\bullet+}$ and BH^{+} accordingly denote the non-protonated nucleobase radical cation and the protonated nucleobase cation, respectively. The boxes indicate observed fragments. Note, that the double radical site formed after release of the BH+ moiety is an intermediate that quickly rearranges to a more stable structure.*

a weak peak in low-energy photofragmentation (see Fig. 3.8) and in traces for KID. It can be however be assumed that further fragmentation is a more likely process. The preferential hole localication on the sugar moiety has recently been directly observed in photoionization studies of neutral gas-phase thymidine [50]: Whereas C 1s photoionization only leads to formation of small fragments, 50 eV photons induced formation of approximately equal yields of T^{+} and TH^{+}, which in total only amount to half the yield of the sugar moiety fragment.

Alternatively, the initial hole produced on the thymine sugar moiety leads to rapid proton transfer from C1'or C2' to the T moiety (b), followed by rapid beta bond cleavage (c), i.e. formation of a T^{+} radical cation (m/z 126). We do not observe the remaining [dGCA+

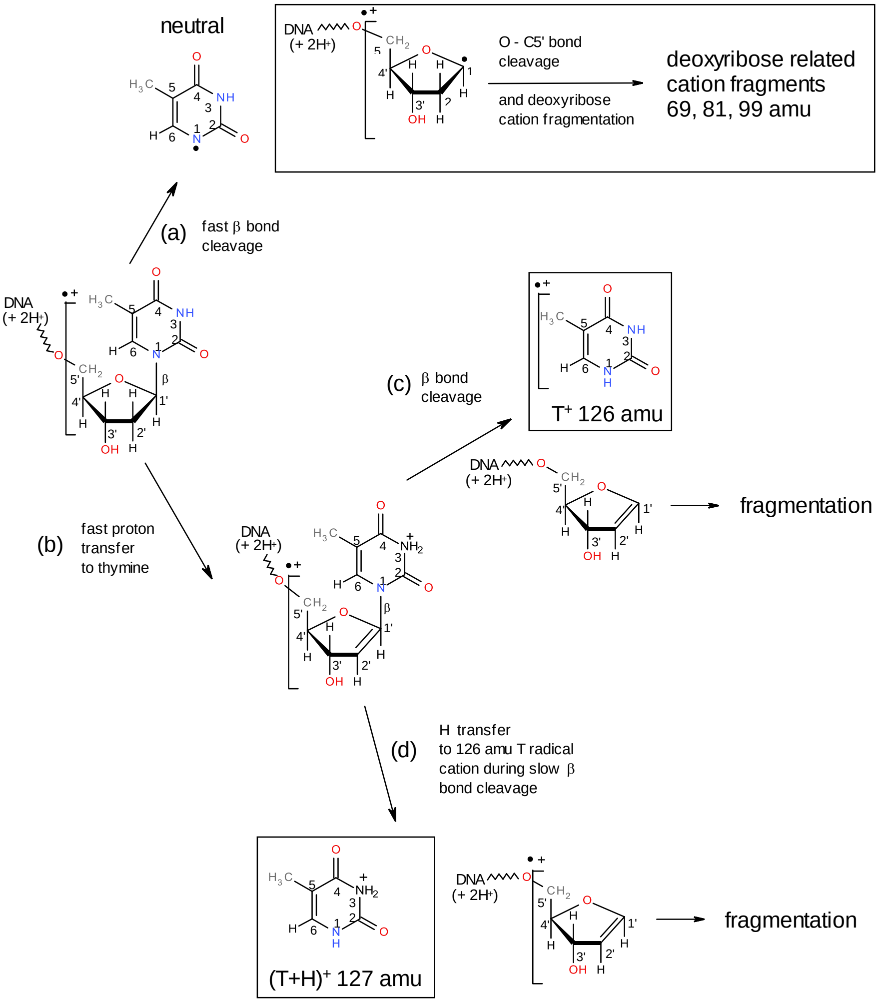

Figure 3.13: *Pathways from non-protonated T nucleotides towards formation of neutral, non-protonated and protonated nucleobase cations (see text). The boxes indicate observed fragments.*

2H]$^{2+}$-sugar moiety (m/z 524.6), i.e. it can be assumed it fragments further to yield other (observed) fragments.

However if after step (b), beta bond cleavage is slow enough, a neutral H can be transfered, from e.g. C2’, to the thymine moiety during beta bond cleavage , leading to (T+H)$^{+}$ (m/z 127), i.e. a protonated free base (d). Again, non-observation of the [dGCA+ 2H]$^{2+}$-sugar moiety suggests further fragmentation into other ion fragments.

3.4.2 Pathways to nucleobase fragment ions: protonated vs non-protonated species

Non-protonated nucleobase cations as observed in our experiments are usually not seen in CID spectra of protonated oligonucleotides. Their occurance in KID and photofragmentation thus is most likely related to the ion or photon induced $[\mathrm{dGCAT+2H}]^{2+}$ ionization and not neccessarily a reflection of the initial protonation site. Clearly, non-protonated fragments can be formed along the two-step pathway sketched above, when the glycosidic bond scission occurs at an unprotonated site or they can be formed from a protonated site, when the H abstraction from the sugar is hindered. As explained before, in $[\mathrm{dGCAT+2H}]^{2+}$, C is always protonated and T is always unprotonated. One of the purines A and G then is protonated, the other one unprotonated. The ratio of protonated to non-protonated ions in the mass spectra will then be determined by the ability 1) to break the C-N bond of either a protonated base or an unprotonated base and 2) the ability of the resulting radical (or ion) to abstract an H radical or a proton from the sugar moiety.

Assuming photoabsorption on a random site of the molecule, C-N cleavage is thermodynamically most likely for pathways leading to most stable products. The protonated radical cation formed from a protonated base (see Fig. 3.12) is more stable than a neutral radical formed from an unprotonated species and C-N cleavage (1) should thus be most likely for protonated bases. Judging from the fact that for the 100% protonated C, only protonated fragment cations are observed for KID and photofragmentation, suggests that H radical abstraction (2) is a very likely process. Additionally, in the less likely case of C-N cleavage for a unprotonated base, H^+ abstraction leads to a non-protonated fragment cation whereas abstraction of a neutral H or no H at all leaves the fragment in a neutral and thus un-detectable state. For the purine bases, cleavage of the C-N bond involving the protonated base is more likely and will most probably lead to formation of a protonated base. Cleavage of the C-N bond for the unprotonated base is less likely and the product might stay an undetected neutral.

This explains the high GH^+/G^+ and AH^+/A^+ ratios observed in KID (see Fig. 3.5) and photofragmentation below the K-edges (see Fig. 3.11). For the 100% unprotonated T, protonated base cations can only be formed after proton migration. For KID, TH^+/T^+ ratios between 0.5 and 0.7 are observed (see Fig. 3.5). For photoionization this ratio is larger than one.

How does the ionization process itself come into play? In pioneering KID studies on polypeptides [51, 52] it was shown that mainly glancing ion trajectories contribute most to the mass spectra. This is because head-on collisions lead to excitation energies in the range of tens of eV inducing extensive multifragmentation into small fragments with masses below the trapping limit employed here. The dominant mechanism in glancing ion-molecule collisions is resonant valence electron capture. KID involving single electron capture is thus expected to trigger fragmentation mechanisms very similar to those following valence photoionization by VUV photons. In our experiments, this is for instance reflected in the observation of sizeable branching ratios for non-dissociative ionization in KID (i.e. for instance formation of 4.2% $[\mathrm{dGCAT+2H}]^{3+}$ after C^{4+} collisions. See Table I.). For the case of photoionization, a similarly high $[\mathrm{dGCAT+2H}]^{3+}$ yield of 9.9% is observed for a photon energy of 15 eV which only allows for photoionization of the highest occupied molecular orbitals. Non-dissociative ionization decreases dramatically with increasing photon energy.

A crucial quantity in the context of ionization are vertical ionization energies (IEs). In nucleotides and DNA the lowest local vertical IEs are found on the nucleobase moieties. As obvious from Table II, the highest vertical IE of an isolated nucleobase is found for T, whereas the purine nucleobases A and in particular G are lowest [42, 43]. This ordering is unaffected by the presence of deoxyribose and phosphate group and reflects the well known fact that holes in DNA are usually trapped at the purine bases [53]. This ordering is pretty much reproduced in the valence photoionization data (photon energies below the C K-edge) and to a much weaker extent in the KID data (see Table I): G^{+} is always strongest and T^{+} is almost always weakest. Induced holes apparently migrate through the oligonucleotide and get trapped at the non-protonated base which has the lowest IE. Accordingly, C^{+} is not observed at all, because it is 100% protonated.

For the projectile ion charge states q=2-5 under investigation here, double (or multiple) electron capture will contribute as well. In this case, KID is expected to resemble deeper photoionization processes. Above threshold K-shell photoionization is usually followed by an Auger-type de-excitation process, leading to double ionization of the $[\mathrm{dGCAT+2H}]^{2+}$ parent molecule accompanied by substantial molecular excitation. High photon energies which are still below the C K-edge can induce a variety of other processes most of which involve deposition of high excitation energies with the possibility of loss of additional electrons. Qualitatively, this is in line with the observation that fragmentation patterns in the low mass range are very similar for C^{q+} impact on $[\mathrm{dGCAT+2H}]^{2+}$ and for photoionization with higher photon energies. Multiple ionization and/or higher excitation also reflects in the yields of non-protonated nucleobase cations. As mentioned above, for KID where single and multiple electron removal contribute, the prevalence of G^{+} is relatively weak and A^{+} and T^{+} have comparable yields for all q. For photoionization above the C K-edge, A^{+} becomes comparable to G^{+} but T^{+} remains low (see Table I).

3.4.3 Protonated vs ionized nucleobases: excitation energy and interaction time

In contrast to CID, photoionization and KID are processes in which charge is removed (and energy is deposited) in a single collision event. Given the size of the oligonucleotides under study, even multiple electron transfer to a C^{q+} projectile ion can be considered a localized process. Furthermore, the timescales of collision or photoionizatin processes are ultra-short in comparision to typical timescales for internal vibrational redistribution of excitiation energy. Most likely this leads to modified fragmentation mechanisms. It is difficult to recognize the consequences of such ultrafast processes from the fragment yields alone. The mere amount of deposited energy strongly influences these yields, as is obvious from Figs. 3.4 and 3.10 where for instance all yields of nucleobase related fragments decrease with increasing C^{4+} velocity v or (over a wide range) with photon energy. Ratios between fragment yields stemming from competing channels, however, can be much more sensitive. The ratio between protonated and non-protonated nucleobase cations shown in Fig. 3.5 clearly shows a relative increase of $[G+H]^+$ as compared to G^+. Clearly, an increase of v (leading to shorter interaction times and higher excitation energies) hinders hole migration towards G. For T, the opposite trend is observed. Here, hole migration *away* from T becomes hindered. The fact that for T a ratio smaller than 1 is found whereas for A and G, the ratios are of the order of two is readily explained by the previously mentioned low PA of T, which is unlikely to be protonated in the first place.

For photoionization a completely different dependence of the ratios on the photon energy is observed (see Fig. 3.11): Below the C K-edge, for T the protonated species is found to increase in comparison to the non-protonated one, whereas for G a moderate decrease is observed. For A, even a dramatic decrease is found. Only for G, the ratios are quantitatively similar to KID. It could be assumed that with increasing photon energy, even below the C K-edge, multiple ionization starts to play a role. In KID, the projectile ion charge state q has an influence on electron removal. However, Fig. 3.6 shows that the effect of increasing q from 2 to 5 on the protonation ratios is only weak.

3.4.4 Backbone scission and the fragmentation of DNA building blocks

The H-abstraction step leading to formation of a protonated or a non-protonated nucleobase fragment (see Fig. 3.12) is likely to trigger the formation of a sugar moiety based dehydrated fragment with m/z 81 (C_5H_5O), which involves backbone scission [40]. This process is indicated as a last step in Fig. 3.12. It is possible, that this fragment transforms into a 6-membered ring. An alternative assignement of m/z 81 to PO_3H_2 derived from the phosphate group was ruled out by deuterium exchange [40]. For KID m/z 81 is dominating the spectra for all charge states and ion kinetic energies. In the photofragmentation case, m/z 81 is very weak for photon energies around 10 eV. However, it becomes comparable to the stronger nucleobase peaks already at 40 eV. Beyond the K-edges of C, N and O, similarly to KID, this fragment dominates (see Fig. 3.10 bottom). The related fragments with m/z 69 and 82 are much weaker in intensity. The peak at m/z 99 can be assigned to a deoxyribose fragment also related to m/z 81 but stemming from either the 5' or the 3' terminal deoxyribose moiety.

It is interesting to note that in collisions with keV ions [22] (and even 70 eV electrons [21]) with gas-phase deoxyribose, C_5H_5O is only observed with very small relative yields. VUV photoabsorption in gas-phase deoxyribose does not lead to formation of this fragment either [13] and also in soft X-ray induced damage to deoxyribose thin films, the yield of m/z 81 fragments is negligible [54]. Why is the fragmentation of gas-phase oligonucleotides so different from its building blocks? First of all, it is not *a priori* clear that gas-phase deoxyribose has the same 5-membered ring structure (furanose form) of its DNA counterpart. A different molecular structure can obviously lead to different fragmentation channels [55]. Secondly the fragments observed do not neccessarily stem from the ion-impact/photoabsorption site in the macromolecule. In case of localized damage, the remaining oligonucleotide might dissociate in a way totally unrelated to that of the impact site. Secondly, the chemical environment is known to dramatically change fragmentation. Last but not least excitation energy might distribute over the entire molecule before dissociation sets in, efficiently "cooling down" the impact/photoabsorption site. To summarize this, the $[GCAT+H]^{2+}$ fragmentation data clearly confirms that the deoxyribose moiety plays an important role in radiation damage of DNA as it was concluded in most gas-phase experiments on isolated deoxybribose molecules but only fragments unobserved in the gas-phase occur.

Besides the gas-phase deoxyribose data, various gas-phase studies have been performed on nucleobases. In the gas-phase nucleobases prove to be more stable than deoxyribose which clearly reflects in the $[GCAT+H]^{2+}$ fragmentation - intact nucleobase cations are always dominating the mass spectra. However, in contrast to the case of deoxyribose, a number of nucleobase fragments is observed, which is found for the gas-phase species as well (see Table I). In VUV photofragmentation, the peaks at m/z 83 and 97 were for instance found for T [12], m/z 95 was found for C [36], m/z 108 was found for A [12] and m/z 109 and 110 were found for G [36]. For ion impact m/z 108 was observed for A [37] and m/z 83 was observed for C [35]. Nucleobase fragmentation in oligonucleotides is thus a non-negligible but weak channel, which leads to fragments also observed for isolated gas-phase nucleobases.

Finally, if the backbone scission leading to the m/z 81 fragment is not preceded by nucleobase loss, fragment cations with m/z 192, 216, and 232 can be formed which correspond to C_5H_5O plus the nucleobase cytosine, adenine, or guanine respectively (see Fig. 3.8). No thymine containing fragment is formed - most probably again due to the low thymine proton affinity already discussed. These nucleoside-related fragments are observed in all KID spectra. For photofragmentation, the respective peaks are strong only for lower photon energies and almost absent when the K-edges are reached. Clearly multiple ionization and higher excitation energies quench these fragments since more extensive multifragmentation is induced.

An important finding of our study is that photofragmentation at the K-edges of either C, N or O leads to virtually identical mass spectra. The non-specifity on the photoabsorption site is not *a priori* expected because in DNA, N is exclusively found in the nucleobases (see Fig. 3.1). Nevertheless, this result is in agreement with studies on dry DNA in the condensed phase, where no characteristic effect was observed for photoionization above ($h\nu = 2147$ eV) and below ($h\nu = 2153$ eV) the phosphorus K-shell.

3.5 Conclusions

In this chapter we have for the first time investigated the response of isolated protonated oligonucleotides upon keV ion impact and upon absorption of energetic photons. Qualitatively similar fragmentation patterns were observed. The spectra were found to be dominated by a deoxyribose fragment with m/z 81 and protonated and non-protonated nucleobase cations. Deoxyribose fragments contribute strongly to the mass spectra but the fragment masses are typically unobserved in gas-phase studies. In agreement to the gas-phase studies, however, deoxyribose seems to be involved in most fragmentation channels. For nucleobases, oligonucleotide fragmentation qualitatively reflects the gas-phase data: Nucleobases appear to be very stable and all observed fragments have previously been described in gas-phase studies. However, our study proves that great care must be taken when directly comparing gas-phase data obtained for a DNA building block with results for more complex systems.

Nucleobase protonation largely reflects the energetic ordering of the nucleobase proton affinities. The ratio between formation of protonated and non-protonated species depends strongly on ion velocity and photon energy. For ions the results indicate that more energetic collisions hinder proton migration towards guanine.

In the future we plan to perform similar experiments with larger oligonucleotides in their de-protonated form. Such species are expected to allow an even more realistic look at molecular mechanisms underlying biological radiation damage.

BIBLIOGRAPHY

[1] J.R. Milligan, J. W., J.A. Aguilera, Radiat. Res., **133**, 151 (1993).

[2] Taucher-Scholz, G. and Kraft, G., Radiat. Res., **151**, 595 (1999).

[3] Dang, H. M., van Goethem, M. J., van der Graaf, E. R., Brandenburg, S., Hoekstra, R., and Schlathölter, T., Eur. Phys. J. D, **60**, 51 (2010).

[4] von Sonntag, C., *The chemical basis for radiation biology*, Taylor and Francis, London (1987).

[5] Jones, G. D. D., Milligan, J. R., Ward, J. F., Calabro-Jones, P. M., and Aguilera, J. A., Radiat. Res., **136**, 190 (1993).

[6] Boudaïffa, B., Cloutier, P., Hunting, D., Huels, M. A., and Sanche, L., Science, **287**, 1658 (2000).

[7] Pan, X., Cloutier, C., Hunting, D., and Sanche, L., Phys. Rev. Lett., **90**, 208102 (2003).

[8] Martin, F., Burrow, P. D., Cai, Z., Cloutier, P., Hunting, D., and Sanche, L., Phys. Rev. Lett., **93**, 068101 (2004).

[9] Lacombe, S., Sech, C. L., and Esaulov, V., Phys. Med. Biol., **49**, N65 (2004).

[10] Hunniford, C. A., Timson, D. J., Davies, R. J. H., and McCullough, R. W., Phys. Med. Biol., **52**, 3729 (2007).

[11] Ptasinska, S., Stypczynska, A., Nixon, T., Mason, N. J., Klyachko, D. V., and Sanche, L., J. Chem. Phys., **129**, 065102 (2008).

[12] Jochims, H.-W., Schwell, M., Baumgärtel, H., and Leach, S., Chem. Phys., **314**, 263 (2005).

[13] Vall-llosera, G., Huels, M. A., Coreno, M., Kivimäki, A., Jakubowska, K., Stankiewicz, M., and Rachlew, E., ChemPhysChem, **9**, 1020 (2008).

[14] Hanel, G., Gstir, B., Denifl, S., Scheier, P., Probst, M., Farizon, B., Farizon, M., Illenberger, E., and Märk, T. D., Phys. Rev. Lett., **90**, 188104 (2003).

[15] Abdoul-Carime, H., Gohlke, S., and Illenberger, E., Phys. Rev. Lett., **92**, 168103 (2004).

[16] Coupier, B., Farizon, B., Farizon, M., Gobet, M. G. F., de Castro Faria, N., Jalbert, G., Quaskit, S., Carre, M., Gstir, B., Hanel, G., Feketova, S. D. L., Scheier, P., and Märk, T., Eur. Phys. J. D, **20**, 459 (2002).

[17] de Vries, J., Hoekstra, R., Morgenstern, R., and Schlathölter, T., Phys. Rev. Lett., **91**, 053401 (2003).

[18] Tabet, S., Eden, S., Feil, S., Abdoul-Carime, H., Farizon, B., Farizon, M., Quaskit, S., and Märk, T. D., Int. J. Mass Spectr., **292**, 53 (2010).

[19] Martin, S., Brédy., R., Allouche., A. R., Bernard., J., Salmoun., A., Li, B., and Chen, L., Phys. Rev. A, **77**, 062513 (2008).

[20] Lopez-Tarifa, P., du Penhoat, M.-A. H., Vuilleumier, R., Gaigeot, M.-P., Tavernelli, I., Padellec, A. L., Champeaux, J.-P., Moretto-Capelle, M. A. P., Martin, F., and Politis, M.-F., Phys. Rev. Lett., **107**, 023202 (2011).

[21] Ptasinska, S., Denifl, S., Scheier, P., and Märk, T. D., J. Chem. Phys., **120**, 8505 (2004).

[22] Alvarado, F., Bari, S., Hoekstra, R., and Schlathölter, T., Phys. Chem. Chem. Phys., **8**, 1922 (2006).

[23] Alvarado, F., Bernard, J., Li, B., Brédy, R., Chen, L., Hoekstra, R., Martin, S., and Schlathölter, T., ChemPhysChem, **9**, 1254 (2008).

[24] Galassi, M. E., Champion, C., Weck, P. F., Rivarola, R. D., Fojón, O., and Hanssen, J., Phys. Med. Biol., **57**, 2081 (2012).

[25] Champion, C., Weck, P. F., Lekadir, H., Galassi, M. E., Fojón, O. A., Abufager, P., Rivarola, R. D., and Hanssen, J., Phys. Med. Biol., **57**, 3039 (2012).

[26] Bacchus-Montabonel, M. C., Łabuda, M., Tergiman, Y. S., and Sienkiewicz, J. E., Phys. Rev. A, **72**, 052706 (2005).

[27] Bacchus-Montabonel, M.-C. and Tergiman, Y. S., Phys. Chem. Chem. Phys., **13**, 9761 (2011).

[28] Schlathölter, T., Alvarado, F., Bari, S., Lecointre, A., Hoekstra, R., Bernigaud, V., Manil, B., Rangama, J., and Huber, B., ChemPhysChem, **7**, 2339 (2006).

[29] Maclot, S., Capron, M., Maisonny, R., Lawicki, A., Méry, A., Rangama, J., Chesnel, J.-Y., Bari, S., Hoekstra, R., Schlathölter, T., Manil, B., Adoui, L., Rousseau, P., and Huber, B. A., ChemPhysChem, **12**, 930 (2011).

[30] Liu, B., Hvelplund, P., Nielsen, S. B., and Tomita, S., Int. J. Mass Spectr., **230**, 19 (2003).

[31] Liu, B., Haag, N., Johansson, H., Schmidt, H. T., Cederquist, H., Nielsen, S. B., Zettergren, H., Hvelplund, P., Manil, B., and Huber, B. A., J. Chem. Phys., **128**, 075102 (2008).

[32] Bässler, M., Ausmees, A., Jurvansuu, M., Feifel, R., Forsell, J.-O., de Tarso Fonseca, P., Kivimäki, A., Sundin, S., Sorensen, S., Nyholm, R., Björneholm, O., Aksela, S., and Svensson, S., Nucl. Instr. and Meth. A, **469**, 382 (2001).

[33] Reichardt, G., Bahrdt, J., Schmidt, J.-S., Gudat, W., Ehresmann, A., Müller-Albrecht, R., Molter, H., Schmoranzer, H., Martins, M., Schwentner, N., and Sasaki, S., Nucl. Instr. and Meth. A, **467**, 462 (2001).

[34] Ni, J., Mathews, M. A. A., and McCloskey, J. A., Rapid Commun. Mass Spectrom., **11**, 535 (1997).

[35] Padellec, A. L., Moretto-Capelle, P., Richard-Viard, M., Champeaux, J. P., and Cafarelli, P., JPCS, **101**, 012007 (2008).

[36] Plekan, O., Feyer, V., Richter, R., Coreno, M., de Simone, M., and Prince, K., Chem. Phys., **334**, 53 (2007).

[37] Alvarado, F., Bari, S., Hoekstra, R., and Schlathölter, T., J. Chem. Phys., **127**, 034301 (2007).

[38] de Vries, J., Hoekstra, R., Morgenstern, R., and Schlathölter, T., J. Phys. B.: At. Mol. Opt. Phys., **35**, 4373 (2002).

[39] Takahata, Y., Okamoto, A. K., and Chong, D. P., Int. J. Quantum Chem., **106**, 2581 (2006).

[40] Phillips, D. R. and McCloskey, J. A., Int. J. Mass Spectrom., **128**, 61 (1993).

[41] Hunter, E. P. L. and Lias, S. G., J. Phys. Chem. Ref. Data, **27**, 413 (1998).

[42] Zaytseva, I. L., Trofimov, A. B., Schirmer, J., Plekan, O., Feyer, V., Richter, R., Coreno, M., and Prince, K. C., J. Phys. Chem. A, **113**, 15142 (2009).

[43] Trofimov, A. B., Schirmer, J., Kobychev, V. B., Potts, A. W., Holland, D. M. P., and Karlsson, L., J. Phys. B: At., Mol. Opt. Phys., **39**, 305 (2006).

[44] Acharya, P., Cheruku, P., Chatterjee, S., Acharya, S., and Chattopadhyaya, J., J. Am. Chem. Soc., **126**, 2862 (2004).

[45] Verdolino, V., Cammi, R., Munk, B. H., and Schlegel, H. B., J. Phys. Chem. B, **112**, 16860 (2008).

[46] Ghosh, D., Golan, A., Takahashi, L. K., Krylov, A. I., and Ahmed, M., J. Phys. Chem. Lett., **3**, 97 (2012).

[47] Rodgers, M., Campbell, S., Marzluff, E. M., and Beauchamp, J., Int. J. Mass Spectrom., **148**, 1 (1995).

[48] McCloskey, J. A., Acc. Chem. Res., **24**, 81 (1991).

[49] Vrkic, A. K., Hair, R. A. O., Foote, S., and Reid, G. E., Int. J. Mass Spectrom., **194**, 145 (2000).

[50] Itää, E., Kooser, K., Rachlew, E., Huels, M. A., and E., K., to be published (private cummunication).

[51] Bari, S., Hoekstra, R., and Schlathölter, T., Phys. Chem. Chem. Phys., **12**, 3360 (2010).

[52] Bari, S., Hoekstra, R., and Schlathölter, T., Int. J. Mass. Spectr., **299**, 64 (2011).

[53] Close, D. M. and Ohman, K. T., J. Phys. Chem. A, **112**, 11207 (2008).

[54] Fujii, K., Akamatsu, K., and Yokoya, A., Int. J. Radiat. Biol., **80**, 909 (2004).

[55] Bari, S., Sobocinski, P., Postma, J., Alvarado, F., Hoekstra, R., Bernigaud, V., Manil, B., Rangama, J., Huber, B., and Schlathölter, T., J. Chem. Phys., **128**, 074306 (2008).

Chapter 4

Length effects in VUV photofragmentation of protonated peptides

We have studied photoionization of protonated synthetic peptides YGnF (n = 0, 1, 3, 5, 10). Photon energies ranging from 8 to 30 eV were used. For YG_nF peptides up to n = 5 small fragment ions related to the sidechains of the aromatic terminal amino acids Y and F dominate the fragmentation patterns. The associated yields scale with total photoabsorption cross section, demonstrating efficient hole migration towards the terminal amino acids upon photoionization of the peptide backbone. For n = 10 the side-chain loss channel is quenched and a series of large dications appear.

---

published:
O. González-Magaña, G. Reitsma, S. Bari, R. Hoekstra, and T. Schlathölter,
Phys. Chem. Chem. Phys., 14, 4351 (2012).

4.1 Introduction

Vacuum ultraviolet (VUV) and extreme ultraviolet (XUV) photophysics of isolated biomolecules are of great interest for astrobiology and radiobiology. Key issues are e.g. ion chemistry in the interstellar medium, transport of free biomolecules from space to earth and their possible role in the development of life, molecular mechanisms of biological radiation damage and fundamental photophysics of complex molecules. In this context, charge migration is of particular interest. Intramolecular charge transfer processes can involve conformational changes and accordingly occur at relatively long timescales [1]. However, in groundbreaking experiments Weinkauf et al. [2, 3] have identified photoactivated fast hole migration in free peptide radical cations which is facilitated by the close energetic spacing of electronic states and their efficient coupling. Theoretical studies predict ultrafast (few fs or even sub-fs) hole migration processes over peptide bonds driven by electron correlation [4, 5] but direct experimental verification is still lacking. A promising route to investigate charge migration in biomolecules in a time-resolved fashion is XUV or VUV single-photon ionization. Very recently, Jiang et al. investigated ionization of gas-phase acetylene using 30 fs pulses of 38 eV photons from the free electron laser FLASH. Fast non-radiative decay via isomerization was observed [6]. Ideally, a similar technique should be applied to peptides but dense gas-phase targets of these fragile non-volatile molecules are difficult to produce. This problem can be overcome by trapping techniques.

Over the past 10 years visible and UV laser spectroscopy of the protonated and deprotonated trapped peptide and protein ions has received considerable attention (for a review, see Ref. [7]). First VUV photoionization and photofragmentation studies on these systems using synchrotron radiation have only been reported very recently [8–10]. For the protonated peptide leucine enkephalin (amino acid sequence tyrosine-glycine-glycine-phenylalanine-leucine, YGGFL) we found that VUV photoionization predominantly leads to formation of ions related to the aromatic tyrosine (Y) and phenylalanine (F) sidechains.

Here we investigate the formation of sidechain-related fragment ions in more detail with a focus on charge migration. Protonated synthetic peptides YGnF are used. Variation of the number of glycine (G) residues n allows for systematic investigation of the effect of peptide length on the formation of sidechain ions. Fragmentation of peptides can often be understood in terms of statistical models such as quasi-equilibrium theory of unimolecular reactions and accordingly breakup patterns are expected to vary strongly with peptide length [11]. For large peptides where statistical fragmentation should be weak, non-statistical fragmentation processes have been proposed [12]. Peptide-size could also affect charge migration, e.g. if it is Coulomb driven.

4.2 Experiment

The experimental technique is described in detail elsewhere [8]. Briefly, singly protonated synthetic peptides $[YG_nF + H]^+$ (n = 0, 1, 3, 5, 10, for 3 see Fig. 4.1) were generated in an electrospray ionization source (ESI). A radiofrequency (RF) ion funnel was used to collect the ions and transport them into a collisionally focusing RF-only quadrupole. The peptide ions were mass selected in a RF-quadrupole mass analyzer and transferred through an end-cap into a 3D RF quadrupole ion trap. A He buffer gas pulse was applied during the trap loading period for collisional cooling of the trapped ions. Typically, the trap was loaded with protonated peptides for a couple of 100 ms, before the ESI beam and the He buffer gas flow were stopped. The He gas was then pumped down for about 200 ms.

VUV and XUV photons from the U125 undulator at the BESSY II synchrotron (Berlin, Germany) were energy selected using a normal-incidence monochromator. The photon beam crossed the RF-trap through the ring electrode with its typical 100 μm × 120 μm focus located in the trap center. The photon flux was monitored on a silicon p-n junction photodiode. A mechanical shutter was used to expose the trapped protonated peptides for 0.1-1 s to the photon beam until a maximum of 10% of the trap content underwent photon absorption. A second He buffer gas pulse was used to cool off fragment kinetic energies before the trap content was extracted into a linear time-of-flight mass spectrometer ($M/\Delta M = 200$). Small fragments ($m < 80$ u) were not trapped. For each mass scan (ESI on, photons on (i)), subsequent subtraction of a scan of the residual-gas photoionization products (ESI off, photons on (ii)) yields the net effect of peptide irradiation. The target density was determined by a mass scan of the unexposed trap content (ESI on, photons off (iii)). For a typical spectrum 1000 of these cycles were accumulated.

4.3 Results

As an example, the evolution of the photoionization/photodissociation spectrum of $[YG_3F +H]^+$ as a function of photon energy is displayed for $m < 200$ u in Fig. 4.1. In the molecular structure shown below the spectra, the most relevant fragments are indicated. The photon energy dependence observed for $[YG_3F+H]^+$ is typical for all $[YG_nF+H]^+$ studied here. For $h\nu$ = 8-14 eV the strongest fragment is the Y immonium ion (m =136 u). Above 14 eV, the m = 148 u fragment due to y_1 that lost an H_2O unit becomes the strongest channel. The Y sidechain (Y_{side}, m = 107 u) becomes the second largest peak.

Except for $[YG_{10}+H]^+$ for all peptides almost exclusively fragments from the aromatic amino acids Y and F are observed, i.e. masses smaller than 200 u. Fig. 4.2 illustrates this for $h\nu$ = 20 eV. This is consistent with our earlier findings for VUV photoionization and keV ion induced ionization of the pentapeptide leucine enkephalin (YGGFL). [8, 13] For n = 10 doubly charged cations become relevant (see zoom in Fig. 4.2). For this peptide also larger fragments due to backbone scission of the peptide occur in sizeable amounts.

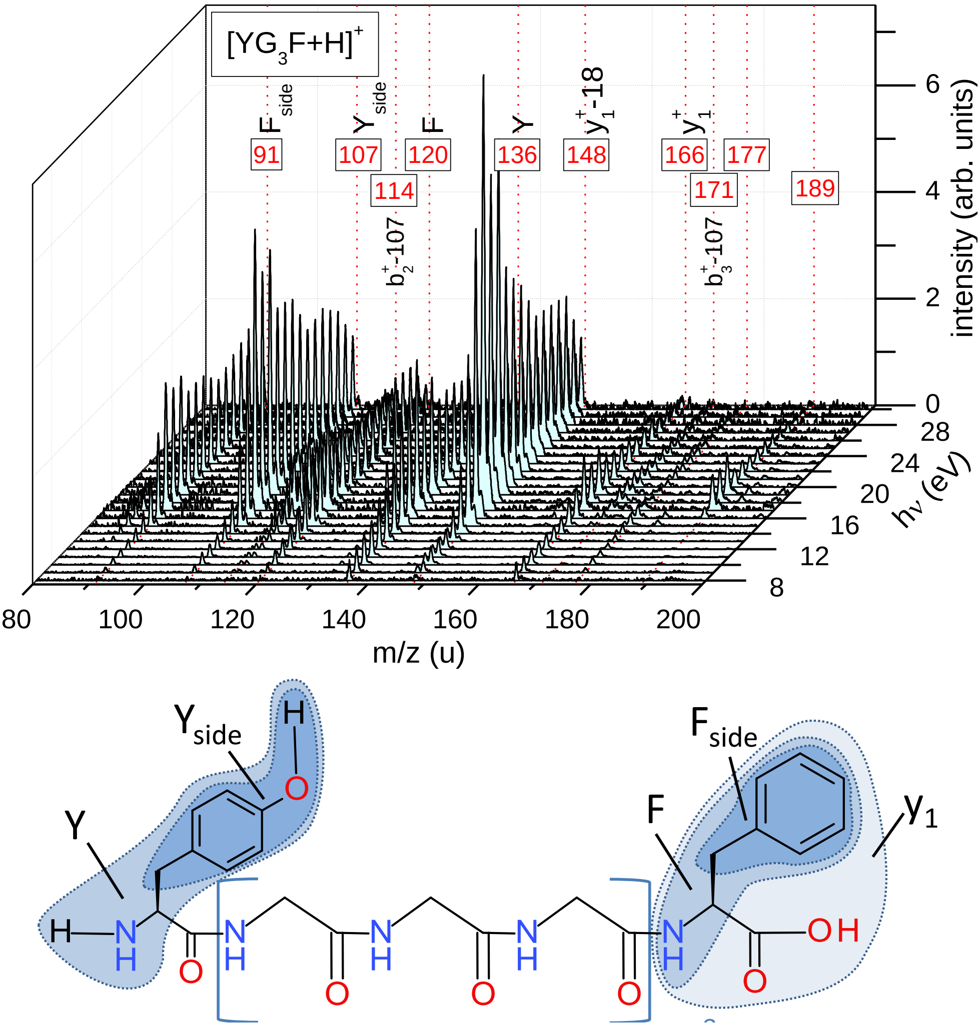

Figure 4.1: *Top: fragment mass spectra of [YG$_3$F + H]$^+$ irradiated by photons of hν = 8-30 eV. Bottom: structure of the YG$_n$F peptides for the example n = 3. The aromatic amino acids tyrosine (Y) and phenylalanine (F) enclose n = 0, 1, 3, 5 or 10 glycine units (G) indicated by brackets. Sidechain-related fragments are highlighted.*

Vertical ionization potentials of protonated peptides containing Y, G and F are typically around 9 eV with the highest occupied molecular orbitals localized on the Y and F aromatic sidechains. Above *hν* = 9 eV vertical ionization of [YG$_n$F + H]$^+$ is thus possible but competes with non-ionizing photodissociation processes following e.g. valence transitions and

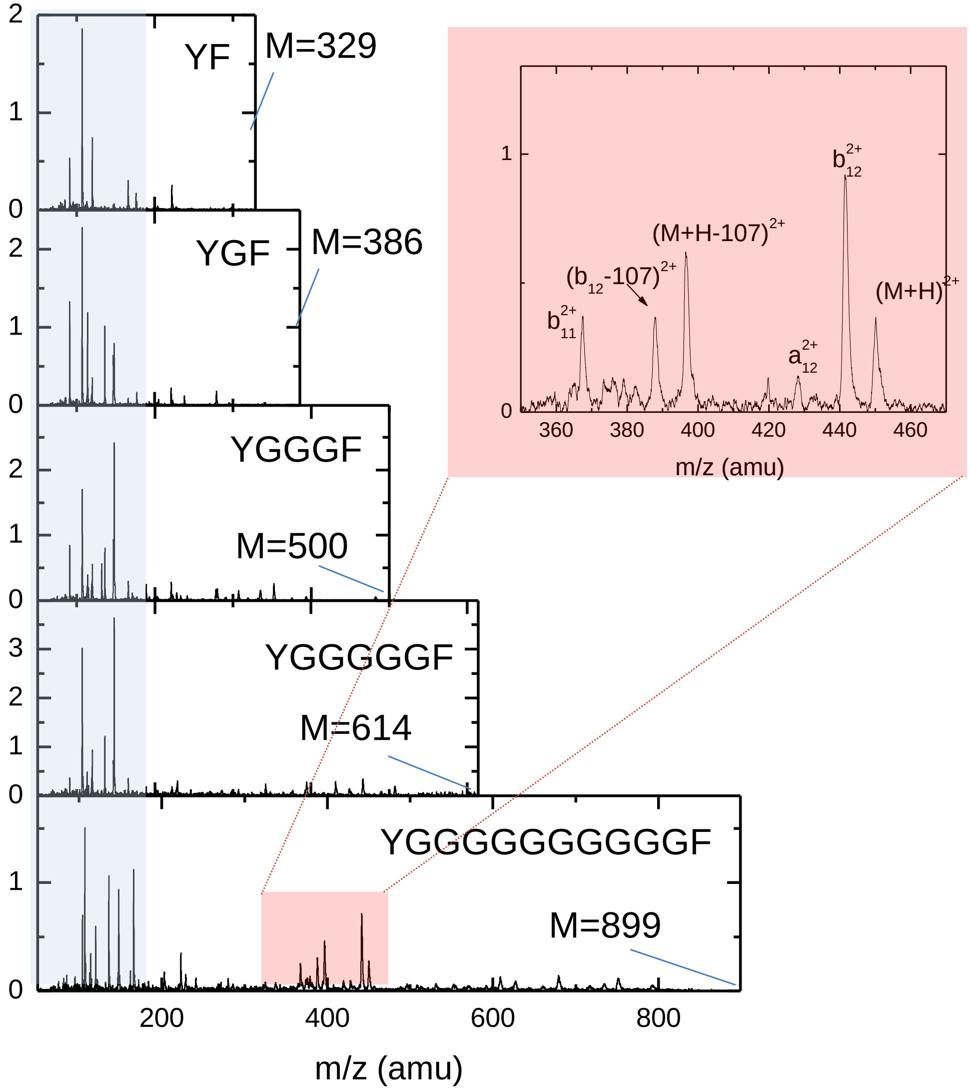

Figure 4.2: *Photofragmentation spectra for* $[YG_nF + H]^+$ *and* $n = 0, 1, 3, 5, 10$ *at* $h\nu = 20$ *eV. The inset displays a zoom in the* $m = 350 - 470$ *u region of the* $n = 10$ *spectrum, where a series of dication peaks are observed.*

transitions to Rydberg states. Since VUV photoabsorption thus leads to photoionization or photodissociation, loss of parent $[\mathrm{YG}_n\mathrm{F} + \mathrm{H}]^+$ from the trap is directly connected to the total photoabsorption cross section $\sigma_{exp}^{tot}(n)$, if the initial trap content, photon flux and irradiation time are known. The $\sigma_{exp}^{tot}(n)$ are displayed in Fig. 4.3 as a function of photon energy with $\sigma_{exp}^{tot}(0)$ set to unity at $h\nu$=17 eV.

For $h\nu$=8-13 eV, $\sigma_{exp}^{tot}(n)$ is almost constant indicating that increasing cross sections for photoionization of outer valence orbitals and decreasing cross section for photodissociation approximately cancel. In this energy range photoionization can be due to the π_1 and π_2 orbitals of the two aromatic rings (the HOMOs in $[YG_nF{+}H]^+$) [14]. From the central G_n part of the $[YG_nF{+}H]^+$, contributions from nonbonding orbitals and π orbitals in the peptide groups strongly contribute, as observed in photoemission studies on GG dipeptides [15].

Above $\approx$13 eV, $\sigma_{exp}^{tot}(n)$ increases strongly with $h\nu$ to reach a broad maximum for $h\nu$ $\approx$16 -18 eV. GG photoemission spectra exhibit two broad maxima for electron binding energies between 13-15.5 eV and 15.5-19 eV [15] due to σ orbitals formed by the C, O and N 2p atomic orbitals [16]. For gas-phase Y and F, broad photoemission features between 13-20 eV are also due to orbitals arising from the atomic 2p orbitals [14]. For higher energies, atomic C(2s) valence orbitals become accessible but the overall cross sections continuously drop.

As obvious from Fig. 4.3, $\sigma_{exp}^{tot}(n)$ strongly increases with n. YG_nF ($C_{18+2n}H_{20+3n}$ $N_{2+n}O_{4+n}$) photoabsorption cross sections can be estimated by adding atomic cross sections [17].
For $h\nu$ =16.7 eV (in the $\sigma_{exp}^{tot}(n)$ maximum region) this procedure yields the cross sections $\sigma_{atom}^{tot}(n)$ given in table I. The addition of atomic photoabsorption cross sections neglects the molecular nature of the target peptides and e.g. underestimates experimental data for benzene by a factor of two in the valence region [18]. Alternatively, we have estimated the $[YG_nF{+}H]^+$ absolute photoabsorption cross sections by adding the available experimental data for the constituent amino acids G and F [19] and assumed $\sigma_Y \approx \sigma_F$. At the same photon energy of 16.7 eV the values for $\sigma_{amino}^{tot}(n) = \sigma_Y + n\sigma_G + \sigma_F$ are given in the table I. $\sigma_{amino}^{tot}(n)$ probably overestimates peptide cross sections slightly as each peptide bond implies the loss of an H_2O unit. The main issue here is to compare the n-dependence of $\sigma_{atom}^{tot}(n)$ and $\sigma_{amino}^{tot}(n)$ with the experimental data. Scaled to the data for n = 0, the $\sigma_{atom}^{tot}(n)$ and the $\sigma_{amino}^{tot}(n)$ are almost equal (see Table I). Scaled to the experimental data for n = 0, the $\sigma_{amino}^{tot}(n)$ are added as shaded bars in Fig. 4.3.

The $\sigma_{exp}^{tot}(n)$ thus scale with peptide cation length n indicating that the aromatic sidechains do not seem to play a special role. This is fundamentally different from the UV range, where photo-absorption chromophores in biomolecules can be very site-specific (e.g. aromatic sidechains such as those of Y and F) [20]. However, up to n = 5 G units we still find the fragmentation spectra to be dominated by fragments related to the Y or the F aromatic sidechain (note: photoionization typically leads to formation of *two* cationic fragments and $\sigma_{exp}^{Y,F}(n)$ can exceed $\sigma_{exp}^{tot}(n)$). To quantify this finding, Fig. 4.3 also displays the total yield of Y and F sidechain related fragments $\sigma_{exp}^{Y,F}(n)$. $\sigma_{exp}^{Y,F}(n)$, defined as the sum of the fragment peak integrals for Y_{side}, Y, F_{side}, F, y_1^+ and $(y_1^+ - H_2O)$ (see Fig. 4.1), increases similar to

n	$\sigma^{tot}_{atom}(n)$	$\sigma^{tot}_{amino}(n)$	$\frac{\sigma^{tot}_{atom}(n)}{\sigma^{tot}_{atom}(0)}$	$\frac{\sigma^{tot}_{amino}(n)}{\sigma^{tot}_{amino}(0)}$	$\frac{\sigma^{tot}_{exp}(n)}{\sigma^{tot}_{exp}(0)}$	$\frac{\sigma^{Y,F}_{exp}(n)}{\sigma^{Y,F}_{exp}(0)}$
0	2.9	5.0	1	1	1	1
1	3.4	5.8	1.17	1.15	1.11	1.31
3	4.3	7.3	1.51	1.45	1.93	1.91
5	5.3	8.8	1.86	1.75	1.82	2.16
10	7.8	12.6	2.71	2.5	2.32	0.78

Table I: *Photoabsorption cross sections at* $h\nu$ *= 16.7 eV (in* 10^{-16} cm^2*) from addition of atomic cross sections [17] (*$\sigma^{tot}_{atom}(n)$*) and addition of amino acid cross sections [19] (*$\sigma^{tot}_{amino}(n)$*). The remaining columns display cross section ratios between* YG_nF *and YF.*

$\sigma^{tot}_{exp}(n)$ untill $n = 5$ is reached. Clearly, holes generated on a G site must migrate towards the Y or F terminal, before formation of a sidechain related fragment cation can take place. Hole migration towards Y and F is energetically favorable because of the lower ionization potentials of Y and F as compared to G, even when initial protonation on the N-terminal is assumed. In the latter case however formation of Y-related cations does not neccessarily require hole migration towards Y. N-terminal protonation will even hinder hole migration towards Y. This is supported by the fact that in the maximum of the photofragmentation cross section, Y related yields always exceed the F related ones with their ratio increasing with n.

Regardless of the exact nature of the hole migration process, two arguments suggest it to be ultrafast, occuring before internal vibrational redistribution (IVR) can set in a couple of ps: i) for a given n the fragmentation pattern is only weakly dependent on the photon energy. Higher photon energies give access to deeper valence orbitals and accordingly increase the average electronic excitation energy of the photoionized molecules. An increase of electronic excitation energy followed by IVR and subsequent statistical fragmentation would neccessarily lead to clear alterations of the fragmentation pattern. ii) for a given photon energy, the fragmentation pattern depends only weakly on n (for n = 0-5 only small fragments are formed). In an IVR/statistical fragmentation scenario, fragmentation patterns would exhibit a strong n dependence because at fixed excitation energy increasing n equals an increase in phase space volume associated to an exponential decrease of dissociation rates for possible dissociation channels [21].

For $n = 10$ (see Fig. 4.3 and Table I) $\sigma^{Y,F}_{exp}(n)$ dropped back to values comparable to the $n = 0$ case. This decrease is remarkable as it indicates that not even holes created on the G units directly adjacent to the Y and F termini are subject to fast migration. Particularly for $h\nu$ = 14-16 eV the yield of doubly charged cations ($\sigma_{dication}$ defined as the sum of the peak integrals $[YG_{10}F{+}H]^{2+}$, a^{2+}_{12}, b^{2+}_{12}, $[YG_{10}F{+}H{-}107]^{2+}$, $[b_{12}-107]^{2+}$ and b^{2+}_{11}, see see Fig. 4.2) is exceeding $\sigma^{Y,F}_{exp}(n)$. Very recently Milosavljević *et al.* [9] reported that VUV photoionization of multiply protonated large protein cytochrome c ($m \approx 12000$ u) either leads to formation

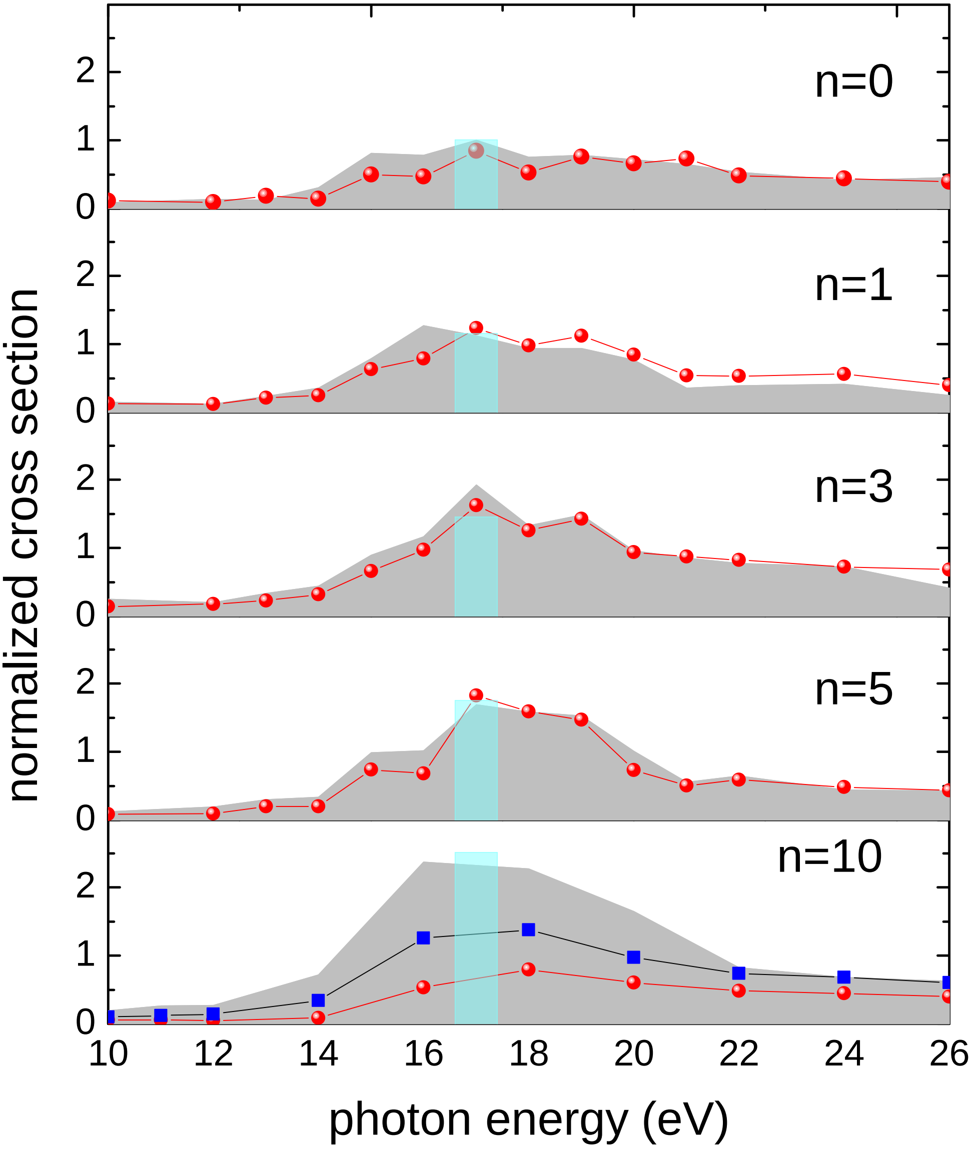

Figure 4.3: *Shaded area:* $\sigma_{exp}^{tot}(n)$ *for [YG*$_n$*F + H]*$^+$ *as a function of photon energy for* n *= 0, 1, 3, 5, 10. The bars indicate* $\sigma_{amino}^{tot}(n)$ *at 16.7 eV and scaled to the experimental data for* n *= 0. Circles: : cross sections* $\sigma_{exp}^{Y,F}(n)$ *for production of Y,F related fragment ions. Squares (n=10): sum of* $\sigma_{exp}^{Y,F}(n)$ *and the cross section for production of doubly charged fragments* $\sigma_{dication}$.

of intact parent cations or to loss of a CO_2 unit. Apparently, for YG_nF and n=10 we witness the transition to the large peptide regime. Holes induced by photoionization of the G sites are not subject to fast migration towards the aromatic terminal amino acids anymore.

Based on the available data it is impossible to identify the exact mechanism of hole migration and its quenching for $n = 10$. Schlag *et al.* [12] for instance discuss the possibility of charge transport along the peptide due to rapid ($\approx$ 100 fs) and almost barrierless dihedral rotation occuring before IVR. In this model, it is conceivable that a G_{10} chain is simply too long to energetically allow for charge transport. On the other hand, electron correlation driven fast charge migration for instance can proceed via very different mechanisms [22, 23] and conformational differences cause differences in timescale ranging from the few fs regime to more than 100 fs [24]. Last but not least, charge migration could also be driven by the Coulomb repulsion away from the existing protonation site and also here, size and conformation are expected to play key roles. Future studies on peptide photoionization must therefore aim for identification of the migration mechanism. Ideally coincident measurement of fragment ion masses and photoelectron kinetic energies to determine the exact excitation energy transferred to the molecule has to be combined with a pump-probe scheme. The latter is feasible at free electron lasers and would give access to the time evolution of charge migration and fragmentation.

To summarize, we investigated VUV photoionization of $[YG_nF+H]^+$ peptide cations for n=0, 1, 3, 5 and 10 for photon energies $h\nu$ = 8-30 eV. $\sigma_{exp}^{tot}(n)$ was found to increase systematically with n as expected from addition of cross sections of the constituent amino acids. Up to $n = 5$ the fragmentation pattern is dominated by formation of cations related to the aromatic sidechains of the terminal Y and F residues, i.e. photoabsorption on the G residues is followed by charge migration to the terminal amino acids. For $n = 10$ this charge migration process was found to be quenched. Instead, large dications and large singly charged fragments were observed while yields of sidechain related fragments get reduced.

BIBLIOGRAPHY

[1] Jortner, J., Bixon, M., Wegewijs, B., Verhoeven, J. W., and Rettschnick, R. P. H., Chem. Phys. Lett., **205**, 451 (1993).

[2] Weinkauf, R., Schanen, P., Yang, D., Soukara, S., and Schlag, E. W., J. Phys. Chem., **99**, 11255 (1995).

[3] Weinkauf, R., Schanen, P., Metsala, A., Schlag, E. W., Bürgle, M., and Kessler, H., J. Phys. Chem., **100**, 18567 (1996).

[4] Henning, H., Breidbach, J., and Cederbaum, L. S., J. Phys. Chem. A, **109**, 409 (2005).

[5] Remacle, F. and Levine, R. D., Proc. Natl. Acad. Sci., **103**, 6793 (2006).

[6] Jiang, Y. H., Rudenko, A., Herrwerth, O., Foucar, L., Kurka, M., Kühnel, K. U., Lezius, M., Kling, M. F., van Tilborg, J., Belkacem, A., Ueda, K., Düsterer, S., Treusch, R., Schröter, C. D., Moshammer, R., and Ullrich, J., Phys. Rev. Lett., **105**, 263002 (2010).

[7] Antoine, R. and Dugourd, P., Phys. Chem. Chem. Phys., **13**, 16494 (2011).

[8] Bari, S., González-Magaña, O., Reitsma, G., Hoekstra, R., Werner, J., Schippers, S., and Schlathölter, T., J. Chem. Phys., **134**, 024314 (2011).

[9] Milosavljević, A. R., Nicolas, C., Lemaire, J., Dehon, C., Thissen, R., Bizau, J.-M., Refregiers, M., Nahon, L., and Giuliani, A., Phys. Chem. Chem. Phys., **13**, 15432 (2011).

[10] Brunet, C., Antoine, R., Allouche, A.-R., and Dugourd, P., J. Phys. Chem. A, **115**, 8933 (2011).

[11] Hu, Y., Hadas, B., Davidovitz, M., Balta, B., and Lifshitz, C., J. Phys. Chem. A, **107**, 6507 (2003).

[12] Schlag, E. W., Selzle, H. L., Schanen, P., Weinkauf, R., and Levine, R. D., J. Phys. Chem. A, **110**, 8497 (2006).

[13] Bari, S., Hoekstra, R., and Schlathölter, T., Phys. Chem. Chem. Phys., **12**, 3360 (2010).

[14] Plekan, O., Feyer, V., Richter, R., Coreno, M., and Prince, K. C., Mol. Phys., **106**, 1143 (2008).

[15] Feyer, V., Plekan, O., Richter, R., Coreno, M., Prince, K. C., and Carravetta, V., J. Phys. Chem. A, **113**, 10726 (2009).

[16] Falzon, C. T., Wang, F., and Pang, W., J. Phys. Chem. B, **110**, 9713 (2006).

[17] Yeh, J. J., *Atomic Calculation of Photoionization Cross-Sections and Asymmetry Parameters*, Gordon and Breach Science Publishers, Langhorne, PE (USA) (1993).

[18] Feng, R., Cooper, G., and Brion, C. E., J. El. Spectr. Rel. Phen., **123**, 199 (2002).

[19] Kamohara, M., Izumi, Y., M.Tanaka, Okamoto, K., Tanaka, M., Kaneko, F., Kodama, Y., Koketsu, T., and Nakagawa, K., Rad. Phys. Chem., **77**, 1153 (2008).

[20] Reilly, J. P., Mass Spectr. Rev., **28**, 425 (2009).

[21] Diau, E. W.-G., Herek, J. L., Kim, Z. H., and Zewail, A. H., Science, **279**, 847 (1998).

[22] Remacle, F., Levine, R. D., Schlag, E. W., and Weinkauf, R., J. Phys. Chem. A, **103**, 10149 (1999).

[23] Breidbach, J. and Cederbaum, L. S., J. Chem. Phys., **118**, 3983 (2003).

[24] Kuleff, A. I. and Cederbaum, L. S., Chem. Phys., **338**, 320 (2007).

Chapter 5

Near Edge X-ray Absorption Mass Spectrometry of a Gas-Phase Peptide

We have studied the dissociation of the gas-phase protonated peptide leucine enkephalin upon X-ray absorption in the region of the C K-edge. The yield of photodissociation products was recorded as a function of photon energy. The total photoabsorption yield is qualitatively similar to near-edge X-ray absorption fine structure (NEXAFS) spectra recorded from condensed phase peptides and proteins. Fragment specificity reveals distinct quantitative differences between spectra obtained for different masses. Fragmentation channels can be assigned to specific electronic transitions some of which are site specific. For instance, C 1$s \rightarrow \pi^\star$ excitations in the leucine enkephalin aromatic sidechains lead to relatively little fragmentation whereas such excitations along the peptide backbone induce strong fragmentation.

---

published:
O. González-Magaña, G. Reitsma, M. Tiemens, L. Boschman, R. Hoekstra, and T. Schlathölter,
J. Phys. Chem. A, 116, 10745 (2012)

5.1 Introduction

Soft X-rays of high flux and high resolution as provided by state of the art synchrotron facilities are an established tool for spectroscopic investigations of various properties of biomolecular systems. Near-edge X-ray absorption fine structure (NEXAFS) and X-ray photoelectron spectroscopy (XPS) are for instance employed to investigate thin films of peptides and proteins. Making use of a comprehensive NEXAFS dataset for common amino acids at all relevant absorption edges [1] it could be shown that soft X-ray spectroscopy is a suitable tool for protein identification and mapping [2, 3]. Furthermore NEXAFS spectral features characteristic for the peptide bond and for different peptide conformations have been identified [4]. However, the sensitivity of NEXAFS to protein secondary structure seems weak [5].

Until very recently, soft X-ray spectroscopy was limited to biomolecular systems in the condensed phase with the exception of comparably small systems (nucleobases, amino acids etc.) for which gas-phase studies have been performed. A major advantage of gas-phase studies is the inherent absence of radiation damage, which can be a serious limitation in the condensed phase. Thin films of the amino acids glycine are for instance subject to peptide bond formation upon soft X-ray absorption [6] whereas dry DNA is found to be efficiently degraded by soft X-rays [7, 8]. Another advantage of gas-phase studies is the possibility of studying photoinduced molecular dynamics in the absence of an energy-dissipating environment. By using nano-solvated gas-phase systems the coupling to the environment can even be studied in detail. In a series of experimental soft X-ray spectroscopy studies on a serious of gas-phase amino acids, electronic transitions were assigned to the various spectral features and conformational effects were investigated [9–11]. Similar studies have been performed for a variety of pyrimidines [12]. Huels *et al.* have investigated photofragmentation of DNA and RNA sugars upon photoabsorption at the C and O 1s edges by means of a photoelectron-photoion coincidence technique and found extensive fragmentation [13].

Gas-phase studies have delivered a wealth of knowledge on small biomolecular systems. The step to larger biomolecular systems in the gas-phase however is difficult, as only a few specific small peptides such as glycyl-glycine (GG [14]) can be evaporated without thermal decomposition. A strategy to circumvent thermal decomposition is the use of small cyclic peptides [15] which possess high stability owing to their ring structure. However, most large biomolecular systems such as peptides, proteins or DNA are so fragile that they disintegrate upon evaporation. The same holds for many smaller systems such as most amino acids. A number of experimental techniques have been developed to overcome this problem. Desorption techniques such as matrix assisted laser desorption ionization (MALDI [16]) or laser induced acoustic desorption (LIAD [17]) have already been used to generate gas-phase biomolecular targets for photoionization experiments. A versatile approach which at the same time allows for production of very pure targets is electrospray ionization (ESI [18]). We have shown that radiofrequency (RF) trapping of mass-selected electrosprayed protonated peptides or oligonucleotides can provide targets sufficiently dense for VUV [19, 20] photofragmentation studies. Similar tandem mass spectrometry experiments on VUV photoionization of much larger protonated proteins [21] and on deprotonated peptides [22, 23] have been reported recently. In a pioneering soft X-ray absorption study, Milosavljević *et al.* have used a trapped gas-phase target to obtain single and double C, N and O near-edge photoionization yields of multiply protonated cytochrome c proteins [24]. Non-dissociative ionization was found to be the dominant channel. (Note, that for effusive targets of much smaller gas-phase molecules, X-ray partial-ion-yield spectroscopy has been performed earlier, for instance on CF_4 at the C and F K-edges [25].)

In the present chapter, we present to our knowledge the first partial-ion-yields of a protonated peptide, the neurotransmitter leucine enkephaline ([YGGFL+H]$+$, m=555.62 Dalton), upon soft X-ray absorption at the C K-edge. Peptides differ from proteins solely in size. In contrast to the much larger protein cytochrome c, leucine enkephaline is subject to extensive fragmentation upon soft X-ray absorption and thus ideally suited to study the photon energy dependence of the various fragmentation channels. In view of the mass-spectrometric approach employed here, throughout this chapter we will therefore refer to the experimental technique as near edge X-ray absorption mass spectrometry (NEXAMS). Based on the experimental data, fragmentation channels can be correlated to electronic transitions. There is a pronounced dependence of peptide stability on the soft X-ray absorption site.

5.2 Experimental technique

We have interfaced a home-built tandem mass spectrometer with the soft X-ray beamline U49/2-PGM-1 at the BESSY II synchrotron facility (Berlin, Germany) . Experimental details can be found in previous articles [19]. Briefly, a beam of protonated peptides was extracted from an electrospray ionization source, phase-space compressed by means of an RF ion funnel and an RF quadrupole ion guide and subsequently mass selected using a RF quadrupole mass filter. Eventually the biomolecular cations were accumulated in a 3D RF ion trap (Paul trap) to reach sufficient target density. Pulsed He buffer gas was employed to collisionally cool the trapped protonated peptides.

The target molecules were then exposed for up to 2600 ms to the soft X-rays until about 5% of the protonated peptides in the trap were photoionized. Subsequent pulsed extraction of the cationic trap content into a linear time-of-flight (TOF) spectrometer ($M/\Delta M \approx 200$) was used to obtain the mass spectrum of the photofragments. Note that ions with $m/z < 70$ are not trapped and the mass spectra are thus cut off in this range. Due to carbon-rich contaminations of the monochromator gratings, at the C K-edge the photon flux varies strongly as a function of photon energy. The photon flux through the trap was therefore monitored using a SXUV-type silicon p-n junction photodiode (IRD, Newbury Park, USA). Typically, photon fluxes in the range of 3×10^{12} s^{-1} - 1.5×10^{13} s^{-1} were used. Absolute energy calibration was accomplished by photoionization of an N_2 gas target at $\approx$ 401 eV [26]. To compensate for contributions of residual gas, from each acquired spectrum a mass scan under identical conditions but with deflected ESI beam (i.e. with an empty trap) was substracted. Eventually a mass scan of the native trap content without ion/photon exposure was measured as a reference and also substracted from the inclusive scan.

Because native trap content and soft X-ray photon flux are known parameters, the loss of parent molecules from the trap can then be used to determine the relative photoionization cross section. Typical mass spectra for soft X-ray photofragmentation of protonated leucine enkephalin $[\mathrm{YGGFL+H}]^+$, which contains the aliphatic amino acids glycine (G) and leucine (L) and the two aromatic amino acids tyrosine (Y) and phenylalanine (F), are displayed in Fig. 5.1 b). The spectra have been obtained at three different photon energies labeled **A**, **B** and **C** corresponding to 285.5 eV, 288.5 eV and 292.0 eV, respectively. We have systematically recorded such mass spectra for photon energies between 282 eV and 310 eV. The stepsize was adapted to the anticipated spectral features, ranging from 0.25 eV to a few eV at an energy resolution of 280 mV fwhm.

Peak integration in these mass spectra allowed to determine cation yields as a function of photon energy. Integration windows were adjusted to the peak broadening with increasing mass. Identical integration windows were used for a given m/z over the whole photon energy range under study. Fig. 5.1 c) displays such a cation yield for m/z 120, i.e. the phenylalanine (F) immonium ion. In the course of this chapter we will refer to such plots as near-edge X-ray absorption mass spectrometry (NEXAMS) spectra.

5.3 Results and discussion

5.3.1 General spectral features

As mentioned in the last paragraph, this work is based on two types of spectra. Mass spectra of the photofragmentation products were recorded systematically for a large number of photon energies (I). NEXAMS spectra for various photofragments were then extracted from this data (II).

I) *Photofragmentation mass spectra:* As is obvious from Fig. 5.1 b) the photofragmentation mass spectra are dominated by fragments with m/z 80–150 u. It is clear that virtually no fragments with masses exceeding m/z 300 are observed. For reference, Table I summarizes all fragments mentioned in this chapter. The strongest yields are observed for the immonium ions at m/z 120 (F), 136 (Y) and the fragments of these groups with m/z 91 and 107 (for the structures of the immonium related fragments, see Fig. 5.2). This is fundamentally different from $[\mathrm{YGGFL+H}]^+$ fragmentation by collision induced dissociation [27], surface induced dissociation [28] and also infrared multiphoton absorption [29] where large fragments due to peptide backbone scission dominate the spectra and immonium ion yields

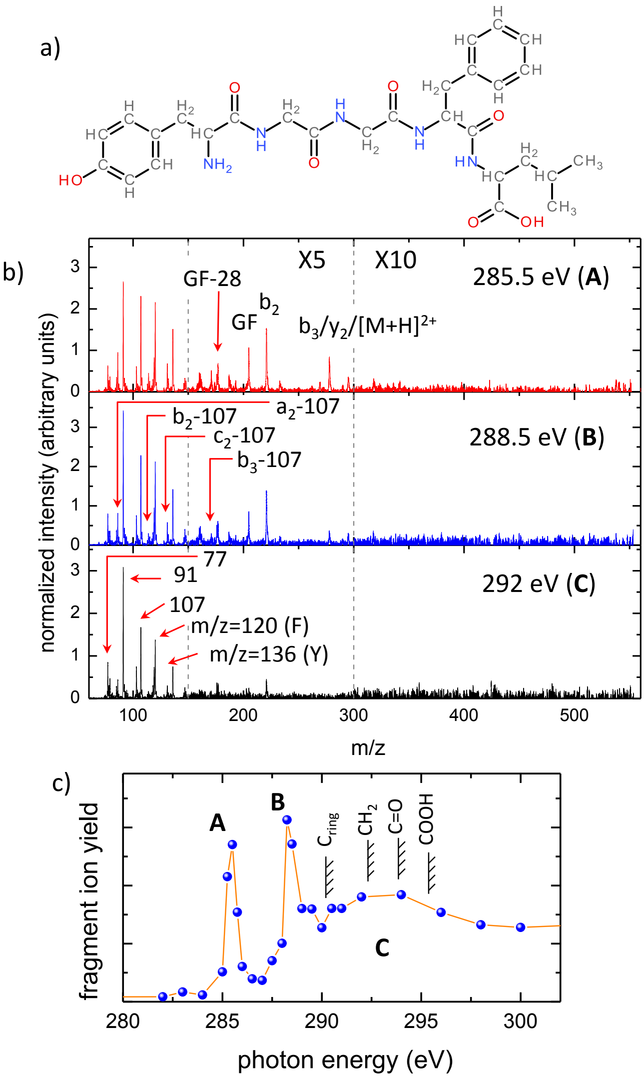

Figure 5.1: *a) Schematic structure of leucine enkephalin. b) Photofragmentation mass spectra for $h\nu$ = 285.5 eV (**A**), 288.5 eV (**B**) and 292 eV (**C**). The intensities in the mass region between 150 and 300 are multiplied by 5 and in the region between 300 and 560 by 10. c) typical C K-edge photoionization yield for the fragment with m/z 120 (phenylalanine immonium ion). The dominating spectral features are labeled **A**, **B** and **C**. Indicated are the C 1s ionization energies for ring (C_{ring}) [11], amino group (CH_2), peptide bond (C=O) and carboxyl (COOH) sites [14].*

are weak. In contrast, VUV photofragmentation spectra at $\approx$ 15 eV are dominated by intermediate size fragments but start to exhibit significant contributions of immonium ions [19]. $[\mathrm{YGGFL{+}H}]^+$ fragmentation spectra that resemble the data in Fig. 5.1 b) have previously only been observed in keV ion induced dissociation (KID) [30]. The predominance of immonium ions in KID and their abundance in VUV photofragmentation has been attributed to relatively high excitation energies in combination with fast dissociation preceeded by charge migration.

A second class of fragments was previously observed for VUV photoionization as well: The spectra in figs. 5.1 b) exhibit a series of fragments due to backbone scission (a_2, b_2, b_3 and c_2) which have subsequently cooled off excess energy by losing the tyrosine sidechain with m/z 107. The structures of these fragments can be found in Fig. 5.3. A number of heavier fragments is observed which are commonly found in conventional mass spectrometric studies. These include an internal GF fragment with m/z 205 [28] and a (GF-CO) fragment with m/z 177. These fragments as well as m/z 295 are probably derived from a cyclicly rearranged a_4 fragment of leucine enkephalin [31]. Another relatively strong larger fragment is found at m/z 221. Finally, the peaks at m/z 278 and 279 due to the b_3 and y_2 fragments, respectively (see sketch in Fig. 5.3), cannot be separated in the spectrum. The $[\mathrm{YGGFL{+}H}]^{2+}$ dication can also contribute to this peak.

II) *NEXAMS spectra:* The overall shapes of the NEXAMS distributions for the various fragments are very similar. Therefore, the spectral features will be discussed exemplarily using the spectrum displayed in Fig. 5.1 c). Clearly, the spectrum is dominated by two sharp peaks labeled **A** and **B** at 285.4 eV and 288.4 eV with FWHM of 0.6 eV and 0.7 eV, respectively. A broader structure (**C**) starts approximately at 290 eV and extends far beyond 300 eV. The spectra show some resemblance to single photoionization yields of the large, multiply protonated protein cytochrome c (m $\approx$ 12834 Dalton) [24]. Nevertheless, for cytochrome c the broad structure **C** is by far the strongest spectral feature.

NEXAFS spectra of condensed phase proteins and peptides can be well predicted by summation of the spectra of their constituent amino acids if a correction for the lack of the peptide bonds is taken into account [2] (C, N and O 1s NEXAFS spectra for 22 amino acids including G, L, Y and F can be found in reference [1]). It is interesting to note that the condensed phase NEXAFS spectra resemble the spectra displayed in Fig. 5.2 closer than the gas-phase protein data [24].

To assign transitions to the different peaks in the (gas-phase) NEXAMS spectra, it is straightforward to employ the available NEXAFS data on gas-phase amino acids. More recently, such gas-phase data became available for Y and F [11] and for G [9]. On the basis of those results the main features of our NEXAMS spectra can be assigned. Peak **A** (285.4 eV) is due to C 1s excitations into the π^*-orbitals of the Y and F aromatic rings. The fact that at this photon energy solely resonant transitions in the aromatic sidechains are induced is a very interesting feature as it adds site specificity to the data. Peak **B** (288.4 eV) stems from

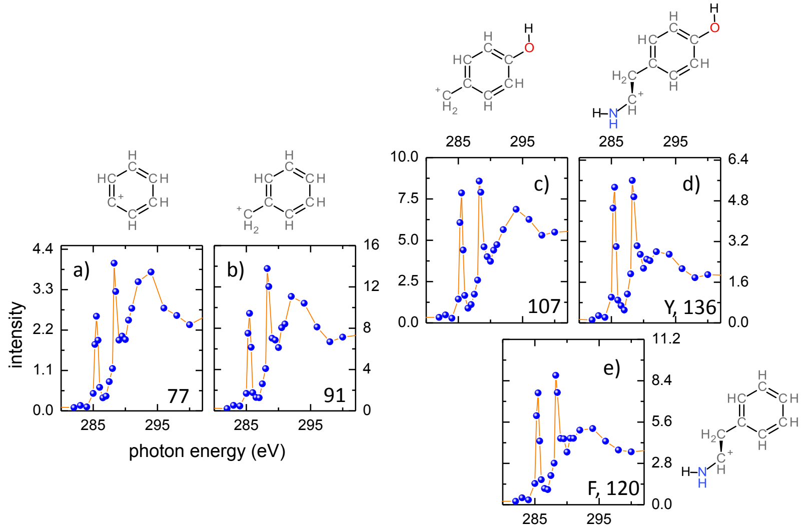

Figure 5.2: *C K-edge NEXAMS spectra of [YGGFL+H]$^+$ for Y and F immonium ions and related fragments of (right: intact Y (d) and F (e) immonium ion, left: related fragments common to both amino acids (a, b). The sketches next to the spectra display the structure of the respective fragment in the parent molecule. Intensities are given in arbitrary units on the same relative scale as the other NEXAMS spectra in this chapter.*

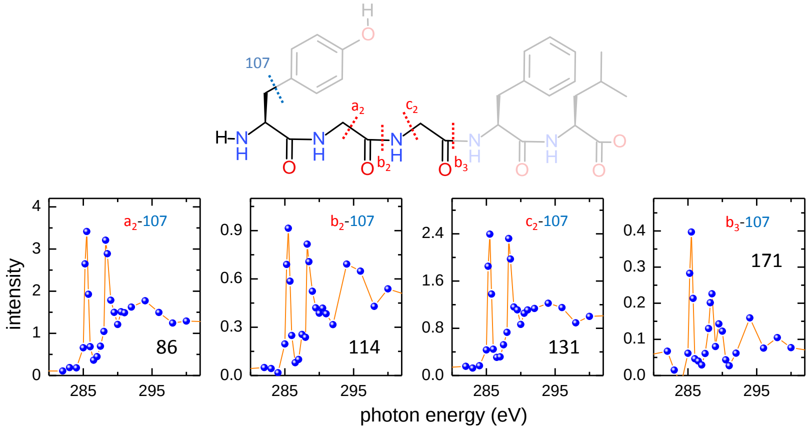

Figure 5.3: *C K-edge NEXAMS spectra of [YGGFL+H]$^+$ for fragments stemming from backbone scission followed by Y-sidechain loss. Intensities are given in arbitrary units on the same relative scale as the other NEXAMS spectra in this chapter.*

transitions of C 1s electrons into the $\pi^*_{C=O}$ of the amide group and is non-specific regarding the constituent amino-acids. On the other hand, the weak structure on the low-energy side of peak **B** which is recognizable in some spectra hints at a contribution of C 1s → σ^* excitations in the Y and F aromatic rings. These energetic positions of the resonances are in very good agreement with existing data, for instance for gas-phase multiply protonated cytochrome c (**A**: 285.5 eV, **B**: 288.5 eV [24]), the gas-phase neutral dipeptide glycyl-glycine (**B**: 288.4 eV [14]), gas-phase tyrosine (**A**: 285.5 eV, **B**: 288.5 eV [11]) and thin films of G, GG, GGG and fibrinogen (**B**: 288.2-288.6 [4]).

The C 1s ionization energies for the peptide backbone and termini can be assumed to be similar to those of the glycyl-glycine dipeptide determined experimentally by Feyer *et al.* [14] as 292.32 eV (C bonded to amino groups), 293.85 eV (peptide bond C) and 295.37 eV (carboxyl terminal C). In addition, the (lower) ionization energies of the aromatic side-chains have been determined experimentally for the isolated amino acids to be 290.2 eV (Y) and 290.3 eV (F) [11] which is exactly at the onset of the broad structure **C** (see Fig. 5.1). There is no gas-phase data available for leucine but it can be assumed that the C 1s ionization energy of the leucine sidechain has a value similar to the 291.0 eV found for alanine, the simplest aliphatic amino acid [10]. A substantial fraction of **C** is thus due to K-shell ionization which - in light elements such as C - rapidly decays nonradiatively by Auger de-excitation [32]. In this regime, a triply charged $[\mathrm{YGGFL+H}]^{3+}$ precursor is thus formed whereas below the ionization threshold, resonant Auger decay leads to formation of doubly charged $[\mathrm{YGGFL+H}]^{2+}$ precursor ions. Intact $[\mathrm{YGGFL+H}]^{3+}$ is clearly absent in the observed mass-spectra and to our knowledge has also not been observed in other studies. For $[\mathrm{YGGFL+H}]^{2+}$ a small yield cannot be ruled out. A second class of contributions to **C** is due to various C 1s $\sigma^\star$ and Rydberg transitions. Of particular interest is a broad continuum resonance at $\approx$ 293.5 eV due to $\sigma^\star$-resonances in the aromatic rings [11]. In the high energy tail of **C**, mainly shape resonances contribute [11, 14].

5.3.2 Fragment specificity

In a VUV photodissociation study of the $[\mathrm{YGGFL+H}]^+$ precursor we have shown that the loss of the aromatic Y and F sidechains is a dominating process [19]. As the immonium ions of the aromatic amino acids Y and F and their fragments play an important role in the fragmentation of $[\mathrm{YGGFL+H}]^+$, Fig. 5.2 displays NEXAMS data for cationic fragments with m/z 136 and 120 (immonium ions of Y and F, respectively), m/z 107 (fragment of the Y immonium ion) and m/z 91 and 77 (common fragments of Y and F immonium ions). Qualitatively, the spectra are similar which implies that near the C 1s edge X-ray absorption anywhere in $[\mathrm{YGGFL+H}]^+$ can trigger the formation of these fragments. This is in line with the results obtained in the VUV photofragmentation study of $[\mathrm{YG}_n\mathrm{F+H}]^+$ VUV photofragmentation study which proved that sidechain loss occurs independently of the initial

m/z	label	explanation	peak ratio **A/B**	peak ratio **A/C**
77		phenylalanine/tyrosine immonium fragment	1.05±0.03	0.9 ± 0.05
91		phenylalanine/tyrosine immonium fragment	1.00±0.01	1.1 ± 0.02
107		tyrosine immonium fragment	1.18±0.02	1.4 ± 0.01
120	F	phenylalanine immonium	1.22 ±0.02	1.8 ± 0.02
136	Y	tyrosine immonium	1.23±0.03	2.3 ± 0.03
86	$a_2 - 107$	N-terminal fragment + tyrosine sidechain loss	1.35±0.02	2.6±0.07
114	$b_2 - 107$	N-terminal fragment + tyrosine sidechain loss	1.54±0.18	1.9±0.23
131	$c_2 - 107$	N-terminal fragment + tyrosine sidechain loss	1.51±0.03	2.2±0.10
171	$b_3 - 107$	N-terminal fragment + tyrosine sidechain loss	1.78±0.18	5.1±1.22
161			1.18±0.24	3.7± 0.58
177	GF-28	internal fragment	1.12±0.15	2.7± 0.27
205	GF	internal fragment	1.39±0.06	5.5± 0.29
221	b_2	N-terminal fragment	1.16±0.06	4.3± 0.21
278	b_3,y_2,$(M+H)^{2+}$	doubly charged parent dominates	1.7±0.18	8.9± 1.17
295		product from cyclic a_4	1.03±0.20	6.5± 0.93

Table I: *Most relevant [YGGFL+H]$^+$ fragments with the respective peak ratios and the statistical errors.*

photoabsorption site, a finding which can be explained in a scenario of charge migration towards the aromatic side-chain followed by fast bond scission [20].

There are, however, clear quantitative differences between the immonium ion related fragment data. It is convenient for the discussion to quantify these differences in the form of the peak ratios as summarized in Table I.

Here, **A/B** denotes the ratio of the respective peak integrals (background substracted) whereas **A/C** is the ratio between the peak intensity in **A** and the average intensity between 290 and 300 eV. As mentioned before peaks **A** and **B** are due to C 1s $\rightarrow \pi^\star$ excitations in the aromatic rings and in the amide groups, respectively.

From Table I it is obvious that the immonium ions at m/z 136 and 120 are more likely to be formed upon $1s \rightarrow \pi^\star$ excitations in the Y and F aromatic rings than along the peptide backbone because **A/B** = 1.23 and 1.22, respectively. C 1s ionization is clearly less efficient in forming these fragments than exciation as indicated by **A/C** values of 1.8 and 2.3, respectively. With decreasing size of immonium fragments, **A/C** decreases rapidly, i.e. ionization becomes more dominant. For m/z 77, **A/C** = 0.9. This decrease is intuitively expected as higher initial charge and/or excitation energy in the system usually shifts the fragmentation pattern towards smaller masses [33]. It is remarkable that **A/B** decreases for m/z 91 and 77 to values close to 1. Therefore, the C $1s \rightarrow \pi^\star$ excitation in one of the sixmembered rings is thus not more likely to induce formation of a small aromatic fragment than photoabsorption along the peptide backbone.

This finding is in line with the NEXAMS data for the fragmentation channels involving backbone scission. These channels are usually associated with lower activation energies than immonium ion formation, because for the latter more bonds need to be broken. For all lower

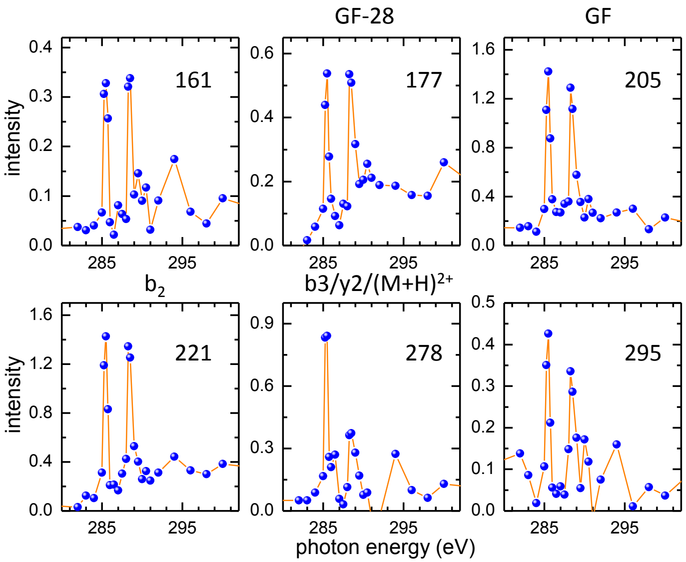

Figure 5.4: *C K-edge NEXAMS spectra of [YGGFL+H]$^+$ for various larger fragments. Intensities are given in arbitrary units on the same relative scale as the other NEXAMS spectra in this chapter.*

activation energy channels studied here, C $1s \rightarrow \pi^\star$ excitation in one of the sixmembered rings has the strongest contribution. We can classify these channels into two groups. As mentioned previously, a number of fragments observed here and also earlier in KID and VUV photofragmentation are due to backbone fragmentation preceded by loss of a m/z 107 Y sidechain. The respective NEXAMS data for the 4 strongest fragments are displayed in Fig. 5.3. The sketch shows which bonds need to be broken in order to form the different fragments. Clearly, for the relatively small $a_2 - 107$, $b_2 - 107$ and $c_2 - 107$ fragments almost identical NEXAMS data are observed. (We note that the $a_2 - 107$ fragment at m/z 86 may in part also be due to the L immonium ion.) For these fragments the ratios **A/B** and **A/C** are much larger than 1, namely ≈ 1.5 and $\geqslant 1.9$ (c.f. Table I). This implies that production of N-terminal fragments that lost the m/z 107 sidechain is mostly driven by $1s \rightarrow \pi^\star$ excitations on one of the aromatic rings. For the larger $b_3 - 107$ fragment the effect is most pronounced.

The NEXAMS data for various larger fragments formed without loss of the m/z 107 sidechain is displayed in Fig. 5.4. Here, **A/B** slightly exceeds unity but **A/C** has very large values. Large fragment thus mainly result from C 1s excitation and not from ionization. In the ionization case, probably too much energy remains in the molecule to allow for survival of the larger fragments.

Figs. 5.3 and 5.4 together confirm a conclusion based on our recent VUV photofragmentation study on [YGGFL+H]$^+$ [19]: the loss of the m/z 107 tyrosine sidechain efficiently cools off excess energy. Fragments a_2, b_2 and c_2 can be formed even for above threshold

X-ray absorption if their formation is accompanied by sidechain loss. Other relatively large fragments without a loss of the Y sidechain appear not to be formed above threshold.

For m/z 278 and 279, which is attributed to the $[\mathrm{YGGFL+H}]^{2+}$ dication, the b_3 and/or the y_2 fragment (see Fig. 5.4), low intensities lead to large error bars. It is however clear that this spectrum is special in the sense that **A** is by far the dominating peak whereas **B** is weaker and **C** almost absent. Clearly, mainly C $1s \rightarrow \pi^{\star}$ excitations on the aromatic rings are related to this channel. The particularly high **A/B** ratio might indicate that for this peak the non-dissociative ionization channel contributes strongly and that formation of an intact protonated dication is most likely when the photon is absorbed by one of the aromatic sidechains.

5.4 Conclusion

In this chapter we have presented a near-edge X-ray absorption mass spectrometry study for a gas-phase protonated peptide, the neurotransmitter leucine enkephalin. Partial-ion-yield for various fragments were systematically investigated at the C K-edge as a function of photon energy. Qualitatively the observed NEXAMS data resembles e.g. NEXAFS spectra of peptides and proteins in the condensed phase and photoionization yields of multiply protonated proteins in the gas phase. Quantitatively, significant differences are observed. The observed spectral features in NEXAMS data can be assigned to a number of inner shell excitations and ionizations localized at different sites within the peptide.

The resonance at 284.4 eV is solely due to C $1s \rightarrow \pi^{\star}$ excitations in the aromatic rings. These excitations predominantly lead to formation of large fragments up to the intact protonated dication and weaker in case of small fragments. Thus, C $1s \rightarrow \pi^{\star}$ excitations in the aromatic rings are apparently the softest X-ray absorption channels in protonated leucine enkephalin. However, C 1s excitation along the peptide backbone contributes strongly to the formation of smaller fragments and is a more destructive channel. C 1s ionization (above threshold) leads to very extensive fragmentation, independently of the actual absorption site.

From the presented data it is clear that NEXAMS is a new feasible approach to obtain information on dynamical processes in intermediately sized biomolecular systems. Together with the fact that site selective resonances can be identified this implies the possibility of studying charge migration upon inner shell excitation in synthetic model systems.

Judging from the extensive fragmentation observed in [YGGFL+H]+ upon soft X-ray absorption, the present study is focused on the high excitation regime. On the other hand, Milosavljević *et al.* have investigated a large protein where virtually no fragmentation is observed [24]. Therefore, it will be interesting to explore the intermediate regime where excitation energies become just sufficient to cause fragmentation. In this threshold region, site selectivities might be even more pronounced. NEXAMS is an experimental technique ideally suited for such studies.

BIBLIOGRAPHY

[1] Zubavichus, Y., Shaporenko, A., Grunze, M., and Zharnikov, M., J. Phys. Chem. A, **109**, 6998 (2005).

[2] Stewart-Ornstein, J., Hitchcock, A. P., Hernández Cruz, D., Henklein, P., Overhage, J., Hilpert, K., Hale, J. D., and Hancock, R. E. W., J. Phys. Chem. B, **111**, 7691 (2007).

[3] Zubavichus, Y., Shaporenko, A., Grunze, M., and Zharnikov, M., J. Phys. Chem. B, **112**, 4478 (2008).

[4] Gordon, M. L., Cooper, G., Morin, C., Araki, T., Turci, C. C., Kaznatcheev, K., and Hitchcock, A. P., J. Phys. Chem. A, **107**, 6144 (2003).

[5] Schwartz, C. P., Uejio, J. S., Duffin, A. M., England, A. H., Kelly, D. N., Prendergast, D., and Saykally, R. J., Proc. Natl. Acad. Sci., **107**, 14008 (2010).

[6] Kaneko, F., Tanaka, M., Narita, S., Kitada, T., Matsui, T., Nakagawa, K., Agui, A., Fujii, K., and Yokoya, A., J. Electron Spectrosc. Relat. Phenom., **144**, 291 (2005).

[7] Ptasinska, S., Stypczynska, A., Nixon, T., Mason, N. J., Klyachko, D. V., and Sanche, L., J. Chem. Phys., **129**, 065102 (2008).

[8] Fujii, K. and Yokoya, A., Radiat. Phys. Chem., **78**, 1188 (2009).

[9] Plekan, O., Feyer, V., Richter, R., Coreno, M., de Simone, M., Prince, K. C., and Carravetta, V., J. Phys. Chem. A, **111**, 10998 (2007).

[10] Feyer, V., Plekan, O., Richter, R., Coreno, M., Prince, K. C., and Carravetta, V., J. Phys. Chem. A, **112**, 7806 (2008).

[11] Zhang, W., Carravetta, V., Plekan, O., Feyer, V., Richter, R., Coreno, M., and Prince, K. C., J. Chem. Phys., **131**, 035103 (2009).

[12] Bolognesi, P., O'Keeffe, P., Ovcharenko, Y., Coreno, M., Avaldi, L., Feyer, V., Plekan, O., Prince, K. C., Zhang, W., and Carravetta, V., J. Chem. Phys., **133**, 034302 (2010).

[13] Ha, D. T., Huels, M. A., Huttula, M., Urpelainen, S., and kukk, E., Phys. Rev. A, **84**, 033419 (2011).

[14] Feyer, V., Plekan, O., Richter, R., Coreno, M., Prince, K. C., and Carravetta, V., J. Phys. Chem. A, **113**, 10726 (2009).

[15] Arachchilage, A. P. W., Wang, F., Feyer, V., Plekan, O., and Prince, K. C., J. Chem. Phys., **133**, 174319 (2010).

[16] Zhang, L., Pan, Y., Guo, H., Zhang, T., Sheng, L., Qi, F., Lo, P.-K., and Lau, K.-C., J. Phys. Chem. A, **113**, 5838 (2009).

[17] Calvert, C. R., Belshaw, L., Duffy, M. J., Kelly, O., King, R. B., Smyth, A. G., Kelly, T. J., Costello, J. T., Timson, D. J., Bryan, W. A., Kierspel, T., Rice, P., Turcu, I. C. E., Cacho, C. M., Springate, E., Williams, I. D., and Greenwood, J. B., Phys. Chem. Chem. Phys., **14**, 6289 (2012).

[18] Fenn, J., Angew. Chem. Int. Ed., **42**, 3871 (2003).

[19] Bari, S., González-Magaña, O., Reitsma, G., Hoekstra, R., Werner, J., Schippers, S., and Schlathölter, T., J. Chem. Phys., **134**, 024314 (2011).

[20] González-Magaña, O., Reitsma, G., Bari, S., Hoekstra, R., and Schlathölter, T., Phys. Chem. Chem. Phys., **14**, 4351 (2012).

[21] Milosavljević, A. R., Nicolas, C., Lemaire, J., Dehon, C., Thissen, R., Bizau, J.-M., Refregiers, M., Nahon, L., and Giuliani, A., Phys. Chem. Chem. Phys., **13**, 15432 (2011).

[22] Brunet, C., Antoine, R., Allouche, A.-R., and Dugourd, P., J. Phys. Chem. A, **115**, 8933 (2011).

[23] Brunet, C., Antoine, R., Dugourd, P., Canon, F., Giuliani, A., and Nahon, L., J. Am. Soc. Mass Spectrom., **23**, 274 (2012).

[24] Milosavljević, A. R., Canon, F., Nicolas, C., Miron, C., Nahon, L., and Giuliani, A., J. Phys. Chem. Lett., **3**, 1191 (2012).

[25] Guillemin, R., Stolte, W. C., Piancastelli, M. N., and Lindle, D. W., Phys. Rev. A, **82**, 043427 (2010).

[26] Fedoseenko, S., Vyalikh, D., Iossifov, I., Follath, R., Gorovikov, S., Püttner, R., Schmidt, J.-S., Molodtsov, S., Adamchuk, V., Gudat, W., and Kaindl, G., Nucl. Instr. and Meth. A, **505**, 718 (2003).

[27] Rakov, V. S., Borisov, O. V., and Whitehouse, C. M., J. Am. Soc. Mass Spectrom., **15**, 1794 (2004).

[28] Laskin, J., J. Phys. Chem. A, **110**, 8554 (2006).

[29] Jockusch, R. A., Paech, K., and Williams, E. R., J. Phys. Chem. A, **104**, 3188 (2000).

[30] Bari, S., Hoekstra, R., and Schlathölter, T., Phys. Chem. Chem. Phys., **12**, 3360 (2010).

[31] Vachet, R. W., Bishop, B. M., Erickson, B. W., and Glish, G. L., J. Am. Chem. Soc., **119**, 5481 (1997).

[32] Guillemin, R., Stolte, W. C., and Lindle, D. W., J. Phys. B: At., Mol. Opt. Phys., **42**, 125101 (2009).

[33] Bari, S., Hoekstra, R., and Schlathölter, T., Int. J. Mass. Spectr., **299**, 64 (2011).

Chapter 6

Ionization and stability of a small protein in ultrashort XUV free electron laser pulses

We have studied the ionization and dissociation of the gas-phase tenfold protonated protein ubiquitin upon XUV (multiple-)photon absorption at the free electron laser facility FLASH (Hamburg, Germany). Ultrashort and highly intense micropulses of (70±30) fs length and up to (18.12±0.03) TW/cm^2 power density were used. Few XUV photon absorption leads to a strong signal due to non-dissociative single and double photoionization, revealing a strong photo-stability of the molecule. The mass spectrum is complemented by a variety of small m/z peaks assigned to immonium ions and related fragments from the amino acids in the protein. multi-photon absorption induces extensive fragmentation of the molecule leading to a dominance of immonium ions and related fragments. Remarkably, the immonium ion yield increase lineally with the number of absorbed photons per molecule up to the range of massive multi-photon ionization. Immonium ion loss seems to be a localized and fast process, almost unperturbed by simultaneous ionization process nearby.

6.1 Introduction

High brightness XUV and X-ray pulses of femtosecond duration are a state of the art technology for the study of the chemical and electronic structure and the dynamics of complex biological molecules. X-ray free-electron lasers (FELs) allow for the study of biomolecular systems at an unprecedented spatial and temporal resolution using single molecules and nanocrystal diffraction [1]. Although significant progress has been made in recent years, there are still many challenges in understanding the initial ionization mechanisms and how they affect the stability of biomolecular systems. Furthermore, biomolecular stability upon (multiple) ionization is also of interest in fields like astrobiology and radiation damage. In the former field, knoeledge on stability and transport of intact building blocks of life from outer space to planets is of great importance. In the latter field, the focus is on the production of secondary particles and their properties.

Over many years, well established techniques based on the absorption of energetic photons from synchrotron sources, for instance X-ray photoelectron spectroscopy (XPS) or near edge X-ray absorption fine structure (NEXAFS), have been employed to study biomolecular structures and dynamics. Because of the relatively small cross sections involved, most often condensed-phase targets were used [2, 3]. Soft X-ray spectroscopy has for instance successfully been used for protein identification and mapping [4, 5]. However, in the condensed phase the structural and dynamical properties of molecules are often strongly influenced by intermolecular interactions such as ultrafast energy transfer [6] or the inevitable radiation damage [7, 8]. To overcome this limitation, very recently a number of groups including ours started to spectroscopically study large biomolecules in the gas-phase, using mass spectroscopy techniques such as ESI and RF ion traps.

In a recent pioneering article, Milosavljević and coworkers have performed ion yield spectroscopy on a 104 residues gas-phase protein to study photoionization processes at the C, N and O K-edges [9]. For ninefold protonated cytochrome c molecules (104 amino acid residues), spectral features similar to NEXAFS data observed for solid protein films were observed in the predominating non-dissociative single ionization channel. When increasing the photon energy beyond the K-edge, non-dissociative double photoionization becomes the dominant process. The only major fragmentation channel observed corresponds to the loss of a CO_2 molecule whereas backbone scission seems to be suppressed. However, it has to be noted that their experimental approach discriminates against small fragment ions. The predominance of non-dissociative processes at K-edge energies is astonishing because ionization is expected to be either due to the direct removal of core electrons or due to further Auger ionization, both involving high excitation energies (see Fig. 6.1).

In a related experiment performed at the KVI, Martin and coworkers have studied multi electron capture from 15 to 19 fold protonated gas-phase cytochrome c in collisions with Xe^{8+} ions [10]. Mainly non-dissociative single and double ionization was observed. The

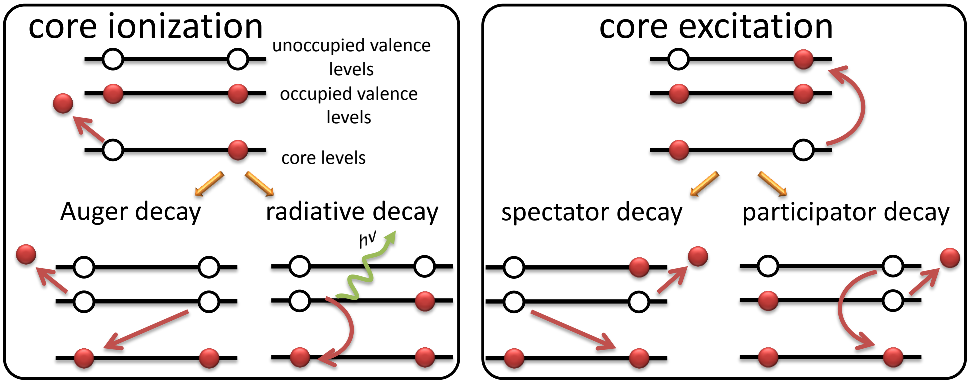

Figure 6.1: *Schematic representation of core excitation and ionization, and possible subsequent decay processes.*

electron capture cross sections were found to be only weakly dependent on the protonation state. Interestingly, even a decrement of the protein charge state by one was observed as a channel of sizable relative cross section. This finding was tentatively ascribed to long distance proton detachment induced by the dynamic polarizing action of the Xe^{8+} Coulomb field.

In contrast, our results on the 5 residue peptide leucine enkephalin (see chapter 5, [11]) showed that soft X-ray induced photoionization almost exclusively leads to extensive fragmentation. For such a system, near edge X-ray absorption mass spectrometry (NEXAMS) is therefore a straigthforward approach and the partial ion yields of the various fragments can be recorded. Clearly, aromatic sidechains play an important role in fragmentation as small sidechain related fragments dominate the breakup pattern. Qualitatively similar dynamics were observed in collisions with H^+ and He^{2+} ions [12].

These findings were rationalized in a framework of photoionization induced fast dissociation through repulsive states *before* internal vibrational redistribution (IVR) of the excitation energy sets in. Subsequent vacuum ultraviolet (VUV) photoionization studies on a series of protonated synthetic peptides of variable size (2-12 residues) confirmed this scenario (see chapter 4, [13]). It was found that ionization along the peptide backbone followed by (ultra)fast charge migration towards an aromatic sidechain seems to be the dominant underlying process. Only for the largest peptide $YG_{10}F$ with 12 residues, an appreciable contribution of non-dissociative single ionization was observed (see inset in Fig. 4.2, chapter 4). In contrast, a $YG_{10}F$ NEXAMS investigation at the C K-edge shows no signs of non-dissociative channels (see Fig. 6.2). VUV photoionization of larger multiply protonated proteins (cytochrome c with 104 residues, ubiquitin with 76 residues and pancreatic trypsin inhibitor with 58 residues), on the other hand, once again induces almost exclusively non-dissociative ionization [14].

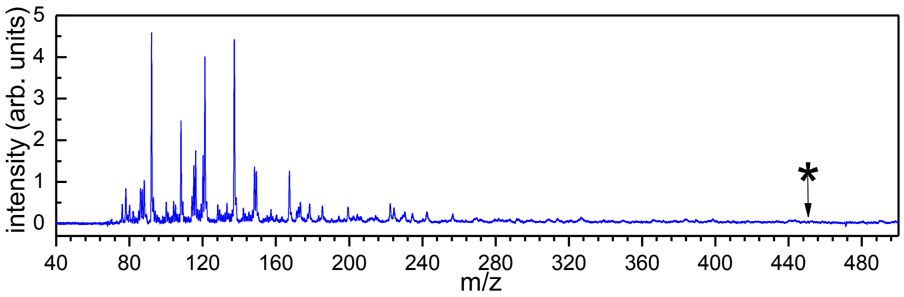

Figure 6.2: *Mass spectrum of protonated $YG_{10}F$ peptides after irradiation with 288.25 eV photons (BESSY). (*) Note that there is no signal due to non-dissociative single ionization which leads to* $[YG_{10}F+H]^{2+}$ *(m/z 450.5).*

The discrepancy between photoionization data for small peptides and for large proteins raises a number of questions: Why is the fast sidechain loss channel apparently suppressed in large systems, even though it is expected to occur before IVR? What is the role of the photoinduced charge(s)? To find answers, we have decided to investigate single and multiple photoionization of tenfold protonated ubiquitin $[Ub+10H]^{10+}$.

Ubiquitin is expressed in all eukaryotic cells where it is enzymatically attached to obsolete proteins as a tag for their controlled degradation [15]. The structural elements of ubiquitin (Ub) are shown in Fig. 6.3. With a well defined sequence of 76 amino acid residues and a mass m = 8565 u, ubiquitin is a relative small protein and thus a good candidate to study photofragmentation. Ubiquitin has no disulfide brigdes, and its tertiary structure thus is not very rigid. Due to a structural extension driven by the Coulomb repulsion of the protonation sites, the 3D structure of tenfold protonated ubiquitin ions is expected to be unfolded and elongated [14]. The protein is composed of two α-helices, five β-strands, and six short loops. The C-terminal tail (residues 71 to 76) is highly flexible [16]. The geometric cross section for tenfold protonated ubiquitin in the gas phase has been reported to range from about 1500 to 1750 $Å^2$, depending on the conformer under study [17]. In the structurally relaxed $[Ub+10H]^{10+}$ protein, photoabsortion induced long–distance migration of charge and/or excitation energy is expected to solely proceed along the protein backbone.

6.2 Experiment

A more detailed description of the setup is given in the experimental chapter. Briefly, in order to perform photoionization and keV ion collision experiments with protonated ubiquitin, we have interfaced our tandem mass spectrometer with the FLASH beamline BL3 (Hamburg, Germany) and with the soft X-ray synchrotron beamlines MAXlab i411 (Lund, Sweden) and BESSY II U-49 PGM1 (Berlin, Germany).

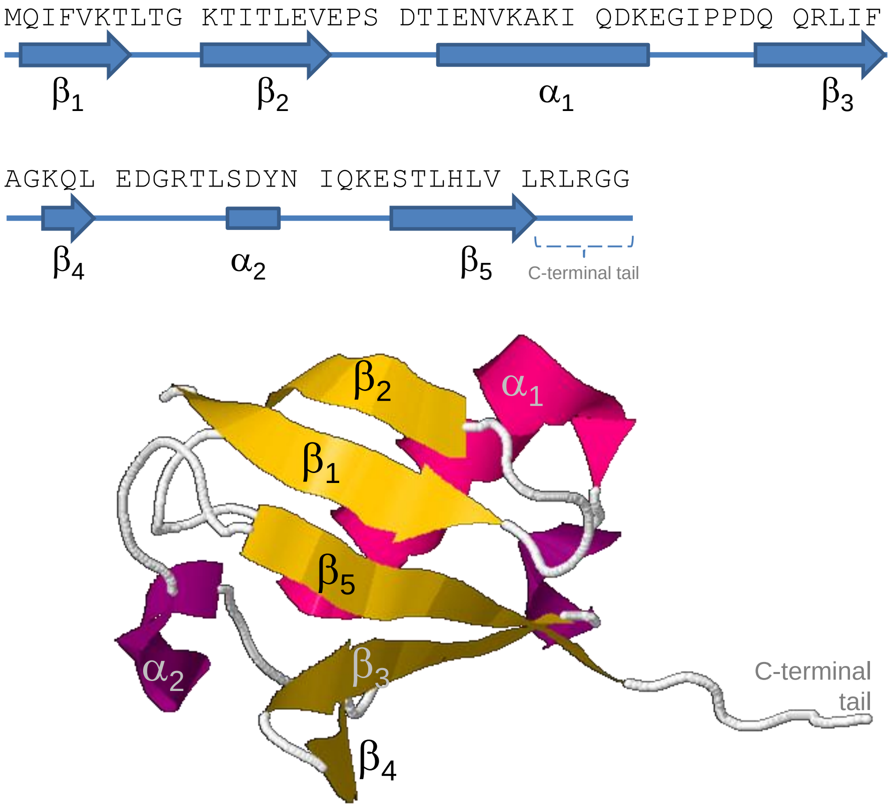

Figure 6.3: *Top: Primary and secondary structure of ubiquitin (Ub). The alpha helices are represented by bars and the beta strands by arrows. Bottom: View of the 3D (tertiary) structure of native ubiquitin. The image was created using Jsmol from the PDB ID1D3Z (www.pdb.org).*

Tenfold protonated ubiquitin ions $[\mathrm{Ub}+10\mathrm{H}]^{10+}$ were produced by means of an electrospray ionization (ESI) source. A 30μM solution of the protein Ubiquitin (isolated from bovine erythrocytes, Sigma-Aldrich, The Netherlands) was prepared using a 1:1 mixture of methanol and water blended with 1% acetic acid. The desired $[\mathrm{Ub}+10\mathrm{H}]^{10+}$ ubiquitin ions were mass selected from the sprayed beam using an RF-quadrupole mass analyzer and then transferred into a 3D RF quadrupole ion trap for subsequent irradiation.

For the FLASH experiments, the beam was tuned to a wavelength of 13.8 nm (89.84 eV) and operated at a macropulse repetition rate of 10 Hz. The FLASH beam was focused into the trap center by means of a back-reflecting mirror mounted 50 cm behind the trap. The reflectivity of the mirror was 70%. The beam diameter in the trap center was (15±5) μm [18, 19]. A fast mechanical shutter with a 14 mm aperture (Uniblitz, Rochester, USA) was used to block undesirable macropulses. In particular, depending on the percentage of

	Total photoabsorption cross section (Mb)		2s component Mb		2p component Mb	
	45 eV	90eV	45 eV	90eV	45 eV	90eV
C (378 atoms)	976.4	260.1	409.7	171.2	566.6	88.9
N (105 atoms)	492.2	132.9	110.7	58.5	381.6	74.3
O (118 atoms)	813.5	256.4	102.6	72.7	710.8	183.7
H (629 atoms)	136.3	16.9				
S (1 atom)	1.1	0.9				

	Total photoabsorption cross section (Mb)		2s component Mb		2p component Mb	
	45 eV	90eV	45 eV	90eV	45 eV	90eV
ubiquitin	2419.5	667.2	623.0	302.4	1659.0	346.9

Table I: *Estimated photoabsorption cross sections for ubiquitin (chemical formula:* $C_{378}H_{629}$-$N_{105}O_{118}S$*) at XUV energies of 45 and 90 eV. Data from Ref. [20].*

trap loss, the shutter was opened for 40 ms or 140 ms to allow for only one or two FEL macropulses to enter the trap, respectively.

Each macropulse, in turn, consisted of a train of 102 micropulses of (70±30) fs length separated 1 μs in time. This time separation is sufficient to ensure statistical movement of the ubiquitin cations out of the beam focus and exposure of a “fresh" set of ions to each micropulse. The micropulse energy delivered by FLASH and averaged over an entire macropulse was typically between 9 to 14 μJ but stable during the recording time of a typical mass spectrum. However, micropulse fluctuations during a macropulse were intrinsic to the experiment. Attenuation of the FLASH beam was accomplished by Xe pressure variation in a gas-cell and/or by moving in thin Al foils. Under the experimental conditions, the number of photons passing the trap per micropulse was varied by attenuation from 3.48×10^9 to 1.59×10^{11} photons.

To determine the number of photons absorbed per ubiquitin molecule from a single micropulse, it is necessary to determine the photoabsorption cross section. For photon energies around 90 eV, molecular photoionization cross sections for e.g. benzene are reproduced within a few percent by summation of the atomic cross sections [21], according to the approach introduced in chapter 4. Using the tabulated state selective atomic photoabsorption cross sections for H, C, N, O and S [20] at 90 eV and the chemical composition of ubiquitin ($C_{378}H_{629}N_{105}O_{118}S$), the total photoabsorption cross section can be determined as 667.2 Mb or 6.672×10^{-20} m^{-2}. Table I shows the details of this calculation. Furthermore, the relative contribution of the different atomic states to the cross section can be estimated. Table I shows that at 90 eV, about 302 Mb, or 45% of the cross section, is due to photoionization involving 2s atomic valence states of C, N and O, while 2p molecular valence states contribute 347 Mb.

amino acid	1-letter code	number of ocurrence	immonium ion mass	related ions found in CID [22, 23]
Alanine	A	2	44	
Aspartic acid	D	5	88	77
Glutamic acid	E	6	**102**	
Phenylalanine	F	2	**120**	91
Glycine	G	6	30	
Histidine	H	1	**110**	82,121,123,138,166
Isoleucine	I	7	**86**	44,72
Lysine	K	7	**101**	70,**84**,**112**,**129**
Leucine	L	9	**86**	44,72
Methionine	M	1	**104**	61
Asparagine	N	2	87	70
Proline	P	3	70	
Glutamine	Q	6	**101**	56,**84**,**129**
Arginine	R	4	**129**	59,70,73,87,100,**112**
Serine	S	3	60	
Threonine	T	7	74	
Valine	V	4	72	41,55,69
Tyrosine	Y	1	136	91,107

Table II: *Amino acids residues, their numbers of appearance in the ubiquitin molecule and m/z values for the respective immonium ions and sidechain related fragments. The fragments observed in the XUV FEL experiment at FLASH are marked in bold.*

6.3 Results and Discussion

In the following, mass spectra and fragment ion yields of tenfold protonated ubiquitin ions upon exposure to ultrashort XUV pulses will be presented. Variation of the pulse energy allows for investigation of a wide range, starting with single or few photon absorption up to the regime of massive multi-photon absorption, i.e. absorption of approximately one photon per residue. For every given pulse energy, only the average number $\bar{n}$ of photons absorbed per protein can be determined, due to the statistical nature of the photoabsorption process and due to experimental uncertainties such as beam fluctuations. The FLASH data will therefore be compared with data from (continuous beam) synchrotron sources, where the number of absorbed photons is exactly one. Variation of the synchrotron photon energy, however, allows to change the excitation energy and the ionization state.

As already observed for smaller peptides, the presence of immonium ions and related fragments of the amino acids are of particular relevance in the spectra. For reference, a list of these ions is given in Table II.

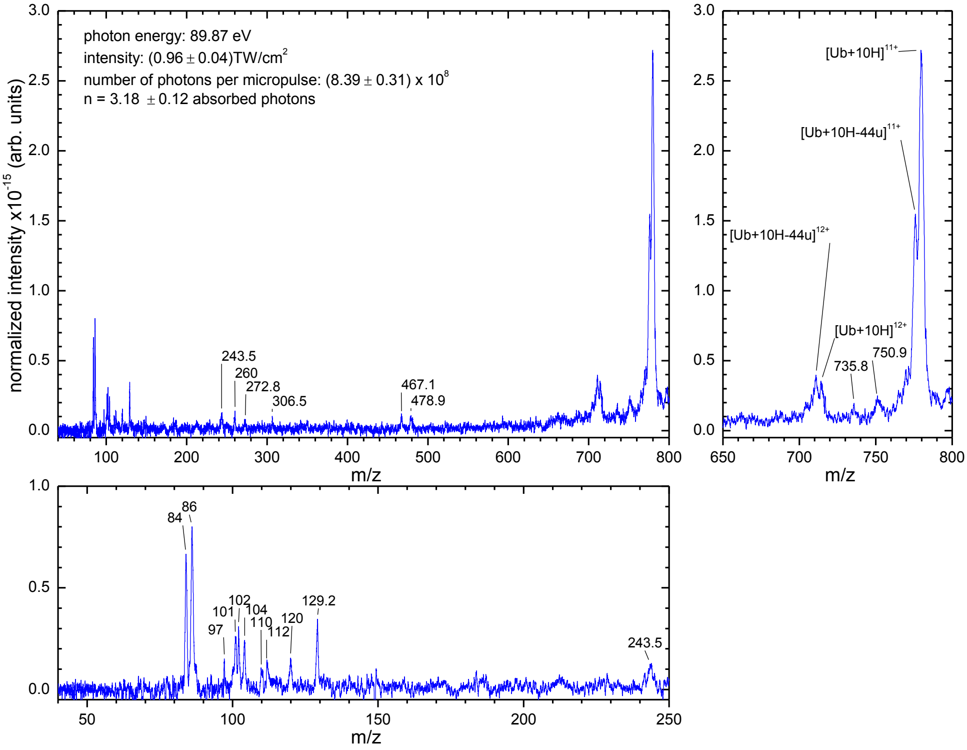

Figure 6.4: *Photofragmentation mass spectrum obtained after irradiation of tenfold protonated ubiquitin with (0.126±0.005) μJ pulses of (70±30) fs length. The photon energy is 89.87 eV. The panels at the bottom and at the right of the figure are zooms into the relevant mass ranges.*

6.3.1 Single-photon absorption in ultrashort XUV pulses of FLASH

Fig. 6.4 shows a normalized photofragmentation mass spectrum of [Ub+10H]$^{10+}$ obtained with (0.126±0.005) μJ XUV pulses of FLASH, i.e. under few photon absorption conditions. The energy of the XUV photons was 89.67 eV, which corresponds to a wavelength of 13.8 nm. The number of absorbed photons per protein generally follows a Poisson distribution, which in case of Fig. 6.4 has an average value of $\bar{n}$ = (3.18 ± 0.12) photons. The Poisson distributions for selected $\bar{n}$ values are depicted in Fig. 6.5. Two aspects in these Poisson distributions should be highlighted. First, note that the probability distribution at the $\bar{n}$ = 3.18(12) value allows for zero photon absorption to occur, and also note that the probability of only one photon absorption is relatively high. At this value, the Poisson distribution covers from 0 to 8 photons absorbed per single ubiquitin molecule. In conclusion, even though the average number of photons absorbed per ubiquitin molecule is greater that one ($\bar{n}$ = 3.18), one photon absorption does contribute to the experiment. A second aspect to highlight is

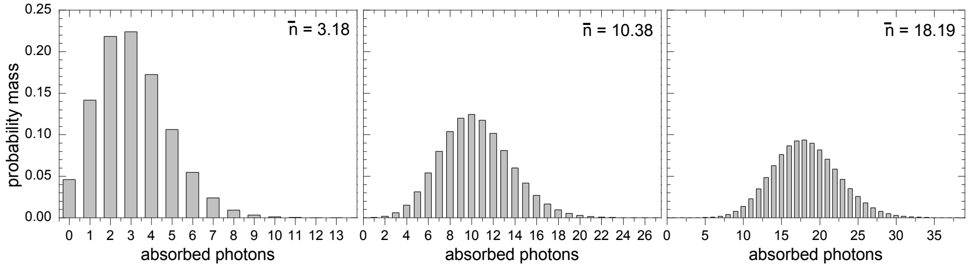

Figure 6.5: *Poisson distribution for selected $\bar{n}$ values.*

that when $\bar{n}$ increases, the distributions widen and become Gaussian shaped with its standard deviation equal to $\sqrt{\bar{n}}$. Therefore, at high $\bar{n}$ values, the probability is distributed over a large number of absorbed photons per ubiquitin molecule.

The spectrum in Fig. 6.4 is clearly dominated by non-dissociative single and double photoionization processes and those accompanied by loss of small neutrals. The strongest peaks correspond to the singly ionized molecules $[\mathrm{Ub+10H}]^{11+}$ and $[\mathrm{Ub+10H\text{-}44u}]^{11+}$, where the latter has lost a neutral fragment of mass around (44±2) u, which can most likely be assigned to CO_2. At slightly lower m/z, the $[\mathrm{Ub+10H}]^{12+}$ peak due to non-dissociative double ionization can be found. Also this peak is accompanied by loss of CO_2.

In the low m/z range, two peaks clearly dominate the spectrum. The strongest peak is found at m/z 86 and can be assigned to the immonium ions from the L (leucine) and I (isoleucine) residues. The second strongest peak at m/z 84 can be assigned to loss of an NH_3 group from the K (lysine) and Q (glutamine) immonium ions [24]. Fig. 6.4 reveals the presence of fragments with m/z larger than 86 but still in the low m/z range. Most of these peaks can be assigned to immonium ions (Q and K (m/z 101), E (m/z 102), M (m/z 104), H (m/z 110), F (m/z 120), and R (m/z 129)) and to immonium related ions (K and R (m/z 112), K and Q (m/z 129)). All these ions are marked bold in Table II. Due to the low-mass cutoff of the RF trap, no clear peaks can be observed on the low mass side of m/z 84. It is clear from Table II that a number of ubiquitin residues is associated with immonium ions of masses in the cutoff region or below. These ions are most probably formed as well but remain undetected.

Additional peaks are observed at m/z values exceeding those of the heaviest immonium ions. Because of the complexity of the ubiquitin sequence and the possibility of formation of internal fragments (possibly formed after rearrangement processes), it is extremely difficult to uniquely assign all these peaks. The situation is further complicated because a given fragment can occur in different charge states. The peak at m/z 260 may be assigned to the b_2^+ fragment and m/z 272.8 to z_3^+. The two prominent peaks in the intermediate mass range at m/z 467 and 479 could be due to a_8^{2+} and a_{13}^{3+}, respectively. The peaks around the single and double photoionization peaks, e.g at m/z 735.8 and 750.9 are too broad for an unambiguous assignment. These peaks could for instance be due to loss of neutral or singly charged fragments from the singly or doubly ionized precursor.

The immonium ions, however, play the central role in the fragmentation process. A quick look at the protein sequence shows that amino acids I and L (related to the immonium ions at m/z 86) occur 16 times and K and Q (related to the m/z 84 related fragments) occur 13 times. These four residues thus account for about 38% of the total number of residues (76) and are fairly equally distributed along the protein sequence (see Fig. 6.3). The formation of immonium ions requires the scission of two bonds in the protein backbone, namely an *a*-type scission of the C-C bond on the NH_2-terminal side of the residue and a *y*-type scission of the C-N bond on the COOH-terminal side of the residue (see Fig. 1.5 for nomenclature). The process should thus be accompanied by the formation of a multitude of different large *b* and *x* fragments which can show up in a variety of charge states. However, no clear evidence for these fragment ions is found in the mass spectrum (see Fig. 6.4).

A mass spectrum obtained by 45 eV single-photon absorption in $[Ub+10H]^{10+}$ is shown in Fig. 6.6. Qualitatively similar features to the ones observed at 89.8 eV are obvious. First of all, the strongest peaks are again due to non-dissociative single photoionization (NDSP) yielding $[Ub+10H]^{11+}$ and single photoionization accompanied by the loss of a neutral CO_2 molecule. In contrast to the 89.8 eV spectrum in Fig. 6.4, however, here the relative cross section for production of $[Ub+10H]^{11+}$ is about a factor of 4 higher, reflecting the larger photoabsorption cross section (Table I).

Furthemore, non-dissociative double ionization ($[Ub+10H]^{12+}$) and the accompanying CO_2 loss are observed. The relative yields with respect to the single ionization channel, are strongly reduced. In the low m/z range, small m/z fragments are observed. The same immonium related peaks are observed and again, relative intensities with respect to non-dissociative single ionization are clearly lower. As for Fig. 6.4, intermediate m/z ions are observed with small yields. The stronger predominance of NDSP at 45 eV as compared to 89.8 eV can be qualitatively explained by smaller excitation because photoionization is on average involving more weakly bound electrons. It is obvious from Table II, that at 45 eV, the photoabsorption cross section for (molecular) 2p orbitals is about a factor of three larger than the cross section for (atomic) 2s orbitals, whereas the cross sections are almost equal at 90 eV.

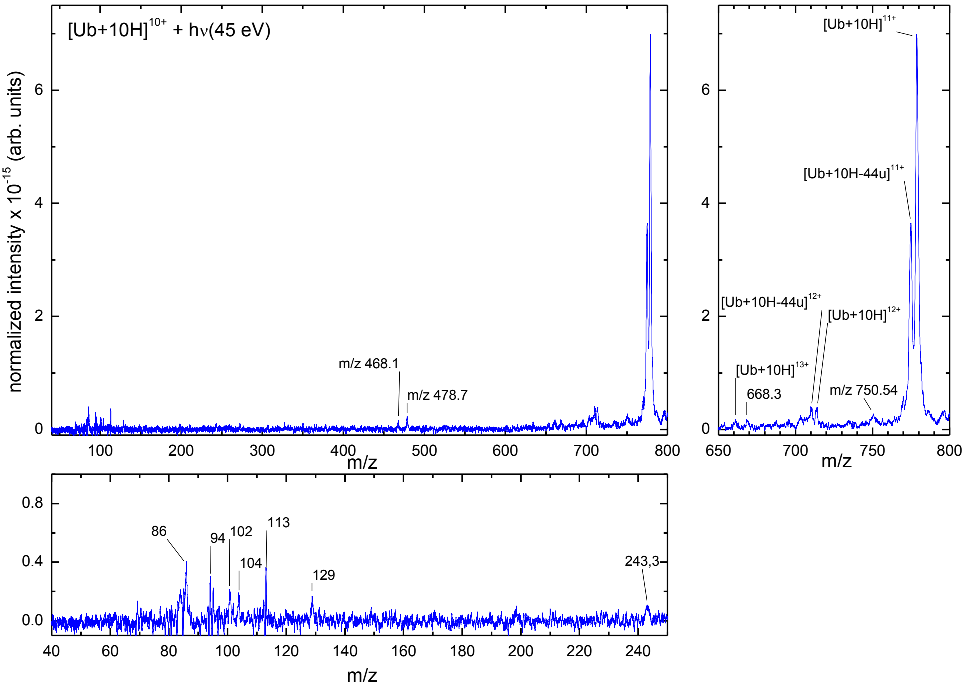

Figure 6.6: *Photofragmentation mass spectrum of [Ub+10H]$^{10+}$ with a 45 eV XUV photon beam provided by a synchrotron facility (MAXlab). The panels at the buttom and at the right of the figure are zooms into the relevant mass ranges.*

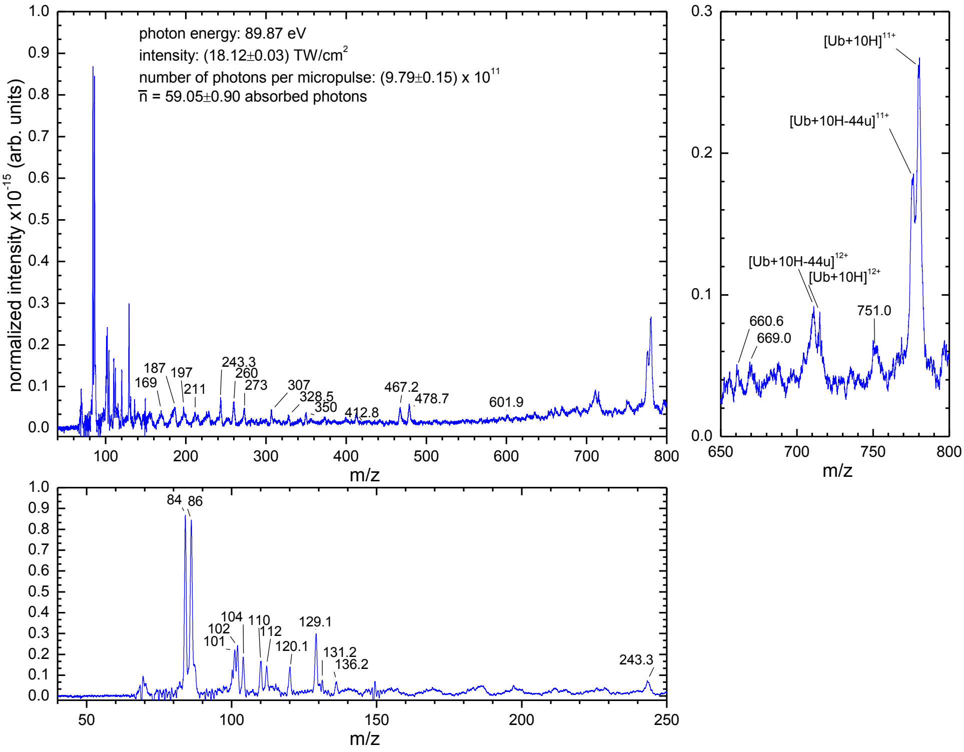

Figure 6.7: *Photofragmentation mass spectrum of [Ub+10H]$^{10+}$ in the massive photoabsorption regime. The energy of the (70±30) fs length micropulses was (2.34±0.04) μJ. The panels at the bottom and at the right of the figure are zooms into the relevant mass ranges.*

6.3.2 Multi-photon absorption

Fig. 6.7 shows a mass spectrum of tenfold protonated ubiquitin after irradiation with high intensity FEL micropulses. At a micropulse energy of (2.34±0.04) μJ, on average (59.05 ± 0.90) photons are absorbed by every protein cation present in the beam focus during a period of 70 fs. Note that the standard deviation of the Poissonian distribution with $\bar{n} = 59$ is ≈ 7.5 wich is much larger that the uncertainty associated with the pulse energy. One expects that moving into the regime of massive multi-photon absorption gives rise to dramatic changes in the fragmentation pattern. A period of 70 fs is much shorter than typical timescales for IVR or long-distance charge migration. The most obvious difference of the multi-photon absorption regime as compared to single-photon absorption is the fact that the peaks due to non-dissociative single and double ionization are not dominating the spectra anymore (see Fig. 6.7). This result is not surprising, since at such high photon fluence, single and double photon absorption is only possible in the "halo" of the focus, where massive multi-photon

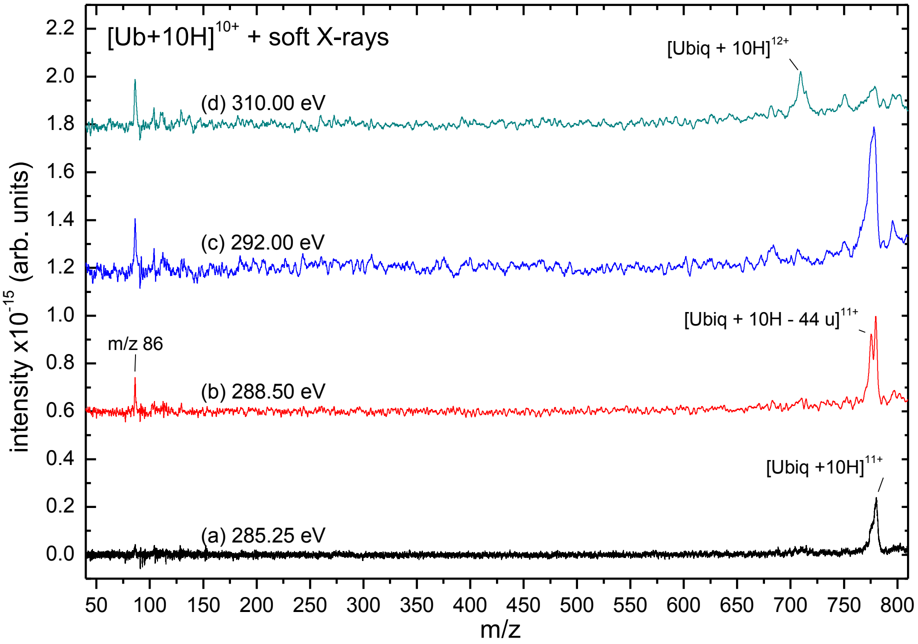

Figure 6.8: *Photofragmentation mass spectra of [Ub+10H]*$^{10+}$ *upon soft X-ray photons provided by a synchrotron facility (BESSY). The photon energies are/were? 284.5 eV (a), 288.5 eV (b), 292 eV (c) and 310 eV (d).*

absorption is not yet possible. Fragmentation spectra such as the shown in Fig. 6.7 are instead dominated by small m/z fragments which are again mainly due to immonium ions and related ions, with m/z 84 and 86 being the strong signals. In addition to the immonium ions, a large number of peaks at intermediate masses is distinguished. To some extent, this is due to the overall higher intensity of the fragment peaks, leading to a much better signal to noise ratio as present in Fig. 6.4. It is interesting to note that even though the parent [Ub+10H]$^{10+}$ cation absorbs a large number of photons rather than one, on a first glance the patterns of the small fragments are very similar for both cases. For a deeper analysis of the effect of XUV multi-photon absorption, it is clearly necessary to study the partial product ion yields as a function of photon flux. Before doing so, it is instructive to look into the transition region, i.e. at mass spectra resulting from different cases of well-defined double ionization processes, triggered by absorption of a single soft X-ray photon.

The absorption of a soft X-ray photon at the C K-edge leads to the excitation or ionization of a C 1s electron. Fig. 6.8 displays mass spectra obtained for single soft X-ray photoabsorption by [Ub+10H]$^{10+}$ at 4 different photon energies. Note, that in the photon energy range here, photoabsorption cross sections are markedly lower than in the XUV and VUV region, resulting in much lower partial ion yields. Clearly, as in the cases of single-photon absorption that were previously discussed in section 6.3.1, the strongest peaks in the mass spectra can be assigned to single ionization processes resulting in the double peaks $[\text{Ub+10H}]^{11+}$ and $[\text{Ub+10H - 44u}]^{11+}$.

Just below the C K-edge, the photoabsorption cross section is so low that the absorption is only possible in case of a resonance with an unoccupied valence orbital, leaving a 1s core hole behind (see Fig. 6.1). This hole is than filled by de-excitation of an electron from an occupied valence orbital. For low-Z atoms such as C, such transitions are typically radiationless. Instead, the excess energy liberates a valence shell electron from the molecule, i.e. a so-called Auger process takes place, thereby ionizing the target — This is discussed in detail in Ref. [25].

At 285.25 eV (a) almost solely $1s\rightarrow \pi^\star$ excitation in the aromatic rings of either phenylalanine (F) or tyrosine (Y) residues is induced [9, 13]. The spectrum is dominated by the non-dissociative single ionization peak with a low-mass shoulder due to CO_2 loss. Small m/z fragments are almost absent, and no evidence for non-dissociative double ionization $[\text{Ub+10H}]^{12+}$ or any other fragment is observed. At the energy 288.50 eV (b), C $1s \rightarrow \pi^\star$ excitation in the C=O bonds of the peptide groups of all residues [4, 26] is the transition dominating photoabsorption. Clearly, a fragment peak with m/z 86 appears, which can be attributed to both leucine (L) and isoleucine (I) immonium ions. Again, no evidence for double ionization peaks is found, which is in agreement with the results presented by the Milosavljević and coworkers [9] on multiply protonated cytochrome c.

Upon crossing of the C K-edge, the photon energy becomes sufficient for direct ionization of a C 1s electron, inducing a 1s core hole as shown in Fig. 6.1. The subsequent Auger de-excitation leads to the removal of a second electron. In Fig. 6.8 (c) obtained at 292.00 eV an intense and broad single ionization peak still dominates the spectrum. This is due to the fact, that even though direct 1s photoionization is energetically possible, at this photon energy, excitation processes into higher lying unoccupied valence orbitals, for instance of σ- or Rydberg-type, are still dominating. At 310 eV (see Fig. 6.8 (d)) almost exclusively direct photoionization of the C 1s electron contributes and accordingly, non-dissociative single photoionization is diminished. Instead, the non-dissociative double ionization channel $[\text{Ub+10H}]^{12+}$ becomes dominant and the peaks due to immonium ions (in particular the strongest peak at m/z 86) reach comparable relative intensities.

Two conclusions can be drawn from Fig. 6.8: i) single as well as double ionization induced by a single soft X-ray photon leads to relatively little fragmentation. ii) The transition from single to double ionization manifests in the spectra in a transition from a predominance of $[\text{Ub+10H}]^{11+}$ to a predominance of $[\text{Ub+10H}]^{12+}$. This is at variance with the results from the multi-photon absorption experiment, where fragmentation is dominating the mass spectrum even though $[\text{Ub+10H}]^{11+}$ is observed with much higher yield than $[\text{Ub+10H}]^{12+}$ (see Fig. 6.7).

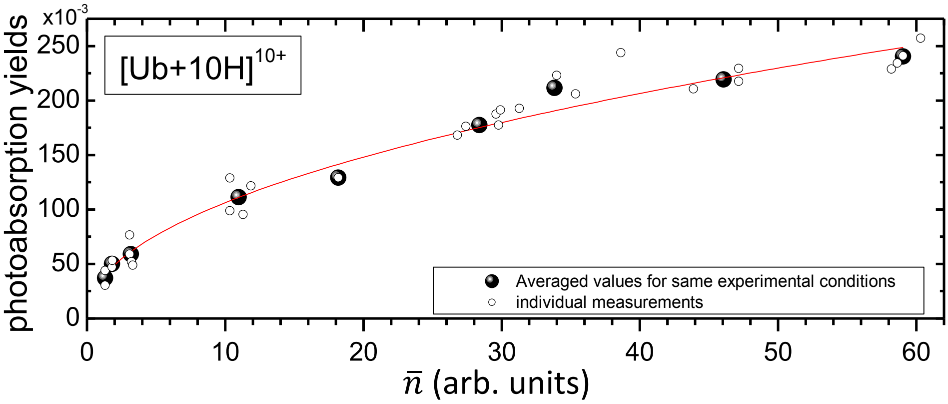

Figure 6.9: *Total photoabsorption yield as function of the average number of photons absorbed per molecule ($\bar{n}$). The line is the best fitting for the function, $y = ax^b$, with a = 0.035(4) and b = 0.48(3). The averaged values were calculated averaging the set of $\bar{n}$ and photoabsortion yields values, which in turn were measured at the same experimental FLASH attenuation conditions, i.e., the variation on the value $\bar{n}$ was only due to intrinsic fluctuations in the intensity of the FLASH beam.*

The reason for the prevalence of [Ub+10H]$^{11+}$ even in the case of ultra intense XUV pulses can be understood if we first discuss the Fig. 6.9, showing the total photoabsorption yield, i.e. the yield due to ubiquitin molecules which absorbed at least one photon and are thus lost from the trap, as a function of the average number of photons absorbed per ubiquitin molecule $\bar{n}$.

To understand the n-dependence of the total photoabsorption yield, it is necessary to discuss the geometric intensity profile of the beam focus. Ideally, the photon flux would be at the nominal value within the focus and negligible outside, i.e. the intensity profile of the beam would be rectangular. For a rectangular beam, the total photoabsorption yield would increase with $\bar{n}$ until the focus is fully saturated. Full saturation is reached, when all molecular ions in the focus have absorbed at least a single photon. As obvious from the Poisson distributions in Fig. 6.5, this is not the case for $\bar{n}$=3, where 5% of molecules do not absorb a photon (at the value $\bar{n} = 1$ this percentage is about 37%). However, at $\bar{n}$=5, this fraction already drops below 1%. Thus, for a rectangular beam profile, the total photoabsorption yield would increase with $\bar{n}$ only up to $\bar{n} \approx 5$ and stay constant for higher $\bar{n}$. However, the actual photon beam is expected to have more of a Gaussian type geometric profile [27]. This implies that with increasing $\bar{n}$ an increasing fraction of the low intensity "tails" of the beam outside the focus becomes sufficiently intense to induce photoabsorption in a substantial fraction of trapped molecules. The total photoabsorption yield increase can thus be explained by geometric effects.

The fragment yields for the non-dissociative single and double ionization channels are

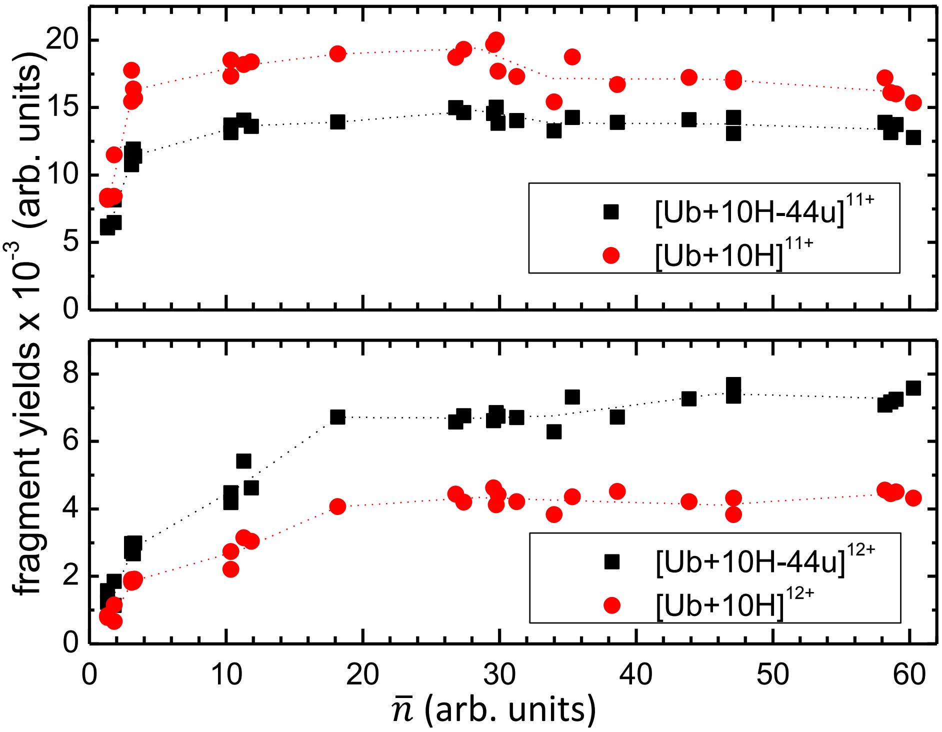

Figure 6.10: *Yields for non-dissociative single ionization (a) and double ionization (b) channels. A line through the averaged values is drawn to guide the eye (see caption of Fig. 6.9 for the definition of averaged values).*

depicted in Fig. 6.10. It can be seen in both cases that the signal saturates already for relatively small $\bar{n}$ values. In the case of single ionization (Fig. 6.10 (a)), there is a quick grown of the yield in the 1 to 4 $\bar{n}$ range. The value of the yield then remains almost constant. This can be understood in the following scenario.

For low $\bar{n}$ the yield increases strongly because the increasing flux of photons through the focus leads to an increase of photoabsorption yield (Fig 6.10). This increase is intuitively expected for $\bar{n} < 1$. From the Poisson distribution for $\bar{n} = 3.18$, it is clear that here the probability for single-photon absorption is still around 13% (see Fig. 6.5). At higher $\bar{n}$, this probability quickly becomes negligible. For instance, only about 0.02% absorption events with $n = 1$ occur for $\bar{n} = 10.97$ (see Fig. 6.10). In case of an ideal rectangular beam profile, the single photoionization related yields of the [Ub+10H]$^{11+}$ and [Ub+10H-44u]$^{11+}$ photoproducts should thus quickly drop to zero with increasing $\bar{n}$ after $\bar{n} = 5$. Clearly, this is not the case. As pointed out in the context of the total photoionization yield, the growing of the "halo" of the focus is preventing this decay. Different from the total photoinization yield,

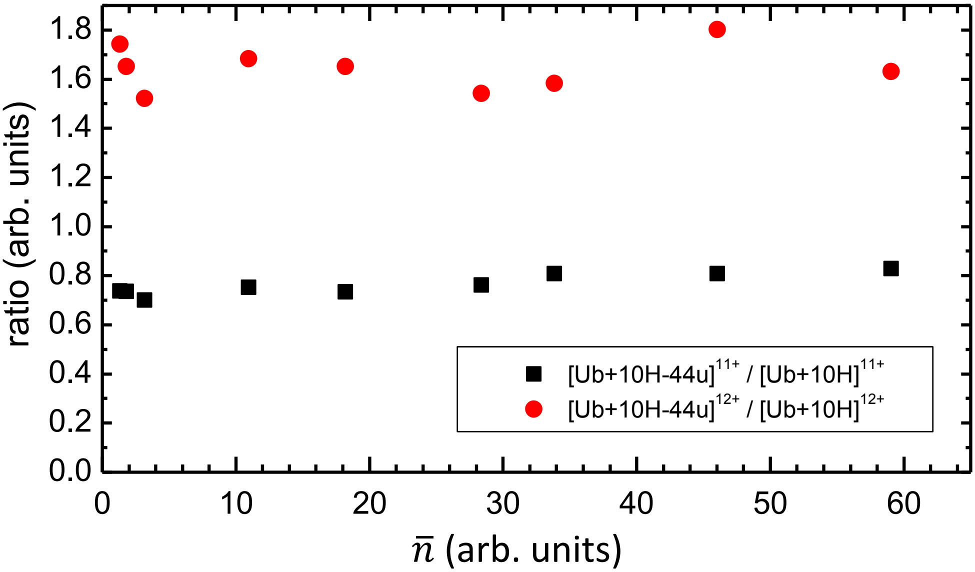

Figure 6.11: *Ratio of single (and double) non-dissociative ionization accompanied with* CO_2 *loss to non-dissociative ionization yields.*

however, here we are looking at the single photoabsorption channel only, which is competing with multiple photoabsorption channels. Clearly, both effects seem to cancel, leading to the observation of a very weak monotonic decrease in 6.10 (a).

A similar effect can be observed for the non-dissociative double ionization yields [Ub +10H]$^{12+}$ in Fig. 6.10 (b). In contrast to single ionization, here the strong increase with $\bar{n}$ leads to a saturation at markedly higher $\bar{n}$ around 20. With further increasing $\bar{n}$ the yield stays constant. Similar to the case of single ionization, the absence of a rapid decrease of the yield at high $\bar{n}$ can be explained by an increasing contribution of the focus "halo". It is interesting, however, that saturation only occurs at $\bar{n} = 20$ (a value 4 times higher than observed for single-photon absorption) even though the probability for two photon absorption is already down to 0.02% for $\bar{n} = 10.97$ (see Fig. 6.5). The reason for the discrepancy between single and double ionization could lie in the fact, that double photoionization can also be the result of single photoabsorption, e.g. through a variety of autoionization processes.

Beside the non-dissociative yields, figure 6.10 also shows the respective data for processes leading to neutral CO_2 loss ([Ub+10H-44u]$^{11+/12+}$). CO_2 loss has been observed before in photoionizaton studies [9]. This channel is not typically observed in CID studies. However, electron (impact) ionization of multiply protonated proteins cations leads to CO_2 loss as the dominant dissociation channel [28]. This pathway was tentatively explained by a hydrogen atom transfer from the COOH to the NH_2 terminal, followed by the loss of the

m/z	assigment	slope x 10^{-4}	yield at $\bar{n}$=3 x 10^{-4}	yield at $\bar{n}$=60 x 10^{-4}
84	$K_{related}$, $Q_{related}$	1.73(2)	8.0(7)	98.0±1.2
86	I,L	2.22(4)	10.9(6)	107.8±1.0
87	$R_{related}$	0.73(2)	4.0(2)	40.3(9)
91	$F_{related}$, $Y_{related}$	0.031(3)	–	1.9(8)
101	K, Q	0.54(1)	3.5(7)	29.4(8)
102	E	0.55(1)	3.3(6)	30.3(5)
104	M	0.42(1)	2.9(6)	22.0±1.1
110	H	0.43(7)	1.4(2)	21.3(5)
112	$K_{related}$, $R_{related}$	0.41(9)	1.7(1)	18.3(1)
120	F	0.35(6)	2.0(4)	17.4(6)
129	R	0.92(17)	4.0(4)	38.0(2)
136	Y	0.19(5)	0.3(4)	9.2(3)

Table III: *Yields and lineal-fitting parameters from selected fragments.*

remaining COO group. Clearly, CO_2 loss from hydrogen deficit protein cations seems to have the lowest activation energy of the feasible dissociation channels. To some extent, the loss of CO_2 from a ubiquitin cation can thus be viewed as an evaporation mechanism, which depends on the amount of energy deposited to the system. Clearly the absorption of two XUV photons leads to a hotter system than absorption of a single photon and in turn will be followed by relatively more " evaporation". The relative yields of non-dissociative ionization and ionization accompanied with CO_2 loss can therefore give insight into the internal energy of the system. The [Ub+10H-44u]$^{11+/12+}$ yields have very similar slopes as their respective non-dissociative counterparts (see Fig. 6.10). The respective ratios can be found in Fig. 6.11.

As can be seen, the value for both single and double ionization ratios remain almost constant at 0.7 and about 1.6 for [Ub+10H-44u]$^{11+}$/[Ub+10H]$^{11+}$ and [Ub+10H-44u]$^{12+}$/[Ub +10H]$^{12+}$, respectively. Two conclusion can be drawn from this result. First of all, the lack of a $\bar{n}$ dependence confirms, that single and double ionization primarliy take place in the "halo" of the focus. Secondly, as expected double photoionization is much more likely to trigger CO_2-loss than single photoionization.

In the context of fs multi-photon ionization, however, the most relevant channels are those leading to the formation of immonium and immonium related ions. Fig. 6.12 shows the yields for some selected fragments as a function of $\bar{n}$. The most striking result is the linear increase of the fragment yields with $\bar{n}$ over the full range under study. The linear fit parameters are presented in Table III. Note, that for the highest $\bar{n}$ values, hints of saturation are visible in the yields. The linearity of the fragment yields has very important consequences. Clearly, the bulk of these fragment ions is formed in the beam focus and under multi-photon

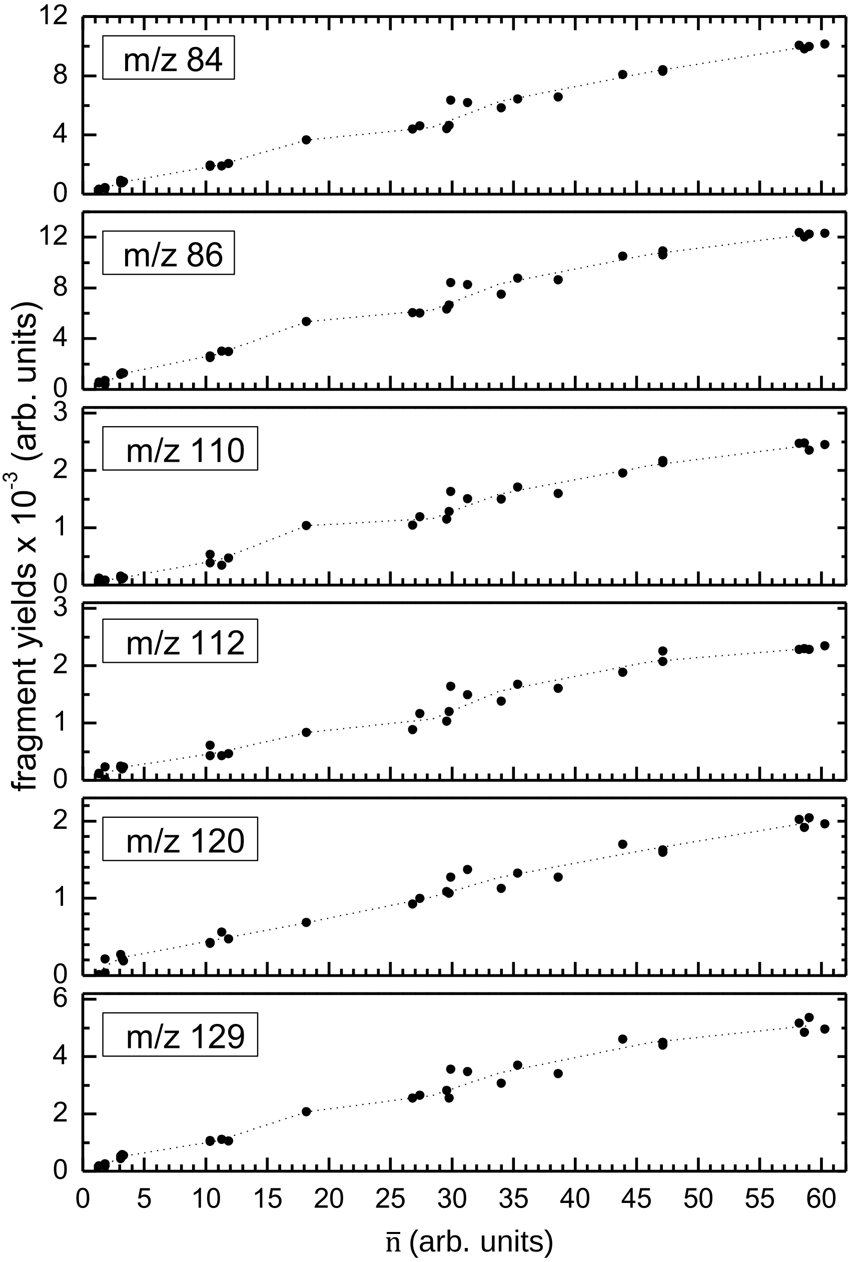

Figure 6.12: *Fragment yields for some of the more relevant immonium ions and small m/z fragments. A line through the averaged values is drawn to guide the eye (see caption of Fig. 6.9). The slope value obtained by a lineal fitting for every dataset are presented in Table III.*

absorption conditions. As already discussed, essentially all proteins ions in the focus volume are ionized already for $\bar{n} \approx 5$. The source for the linear increase with $\bar{n}$ therefore has to be *within* the protein ions. In principle, an immonium ion can be formed from any amino acid residue within a protein. During a micropulse, multi-photon absorption takes place within 70 fs and thus instantaneously with respect to long distance charge migration, energy transport and IVR. Clearly, the most plausible scenario for the process is the following: i) multiple photon absorption and thus ionization along the entire peptide chain. ii) bond scission leading to formation of an immonium (or immonium related) ion for every absorbed photon. For the highest pulse energies under study, $\bar{n} = 60$ which is of the order of the number of ubiquitin residues (76). For $\bar{n}$ = 60, the number of absorbed photons per molecule covers the range from 40 up to 80. This high degree of ionization has a remarkably weak influence on the linearity of the yields in Fig. 6.12. Most likely, the underlying process is therefore of localized nature, i.e. the immonium ion formation proceeds close to the respective photoabsorption site, possibly through a repulsive state. Even though such processes have been previously observed for single ionization of much smaller peptides [11–13], their prevalence in a protein under massive multi-photon absorption conditions is remarkable.

The largest fit parameters in Table III (1.73×10^{-4} and 2.22×10^{-4} for m/z 84 and m/z 86, respectively) are observed for the immonium ions of K and Q and those of L and I. Larger immonium ions have show a much weaker increase with $\bar{n}$. This implies a moderate change of the fragmentation pattern towards smaller masses with increasing $\bar{n}$. When assuming a weak overall increase of molecular excitation (electronic of vibrational) with $\bar{n}$, for instance due to the increase of Coulomb repulsion within the protein cation, then this shift towards smaller masses could for instance reflect a greater stability of the smaller immonium ions.

6.4 Conclusions

In this chapter the ionization and fragmentation of gas-phase tenfold protonated ubiquitin upon exposure to intense 70 fs XUV pulses has been investigated. Using the free electron laser FLASH, it was possible to study a wide range of photon pulse energies, ranging from single/few photon to massive multi-photon absorption per molecule on an ultrashort time scale. For comparison and interpretation of the FEL data, complementary single-photon ionization experiments have been performed at synchrotron facilities. In the single and few photon absorption range, non-dissociative single photoionization (NDSP) was found to be the dominant process. In addition, mainly immonium ions and related ions with relatively low m/z were observed. With increasing pulse energy (and number of absorbed photons $\bar{n}$), these yields were found to increase linearly. This increase can be understood when assuming “instantaneous” absorption of many photons, followed by fast and localized loss of an immonium ion, possibly through a repulsive molecular state. This implies that we not only observe fast sidechain loss occurring before IVR, as previous seen in small peptides [11–13].

The process is even particulary robust, ocurring in the presence of many additional photo-induced hole along the protein. Remarkably, even in the limit where the number of absorbed photons reaches the order of magnitude of amino acids available in the protein, only weak changes in fragmentation pattern were observed. With respect to multi-photon ionization, the protein thus resembles an ensemble of small peptides and possibly even amino acids.

It is envisioned to study the time-dependence of this process in future studies, using the ability of the split-mirror system to split ultrashort photon pulses into a pump and a probe component. Furthermore, it will be of particular interest to investigate the influence of tertiary protein structure on the fragmentation dynamics. To this end, proteins where the tertiary structure is dominated by the effect of disulfide bonds will be employed. Disulfide bonds are known to be able to survive the ESI process and the respective proteins can thus be brought into the gas phase in a compact geometric state which is close to their native structure. As a reference, the same proteins can be investigated with the disulfide bonds chemically cleaved.

BIBLIOGRAPHY

[1] Chapman, H. N., Barty, A., Bogan, M. J., Boutet, S., Frank, M., Hau-Riege, S. P., Marchesini, S., Woods, B. W., Bajt, S., Benner, W. H., London, R. A., Plonjes, E., Kuhlmann, M., Treusch, R., Dusterer, S., Tschentscher, T., Schneider, J. R., Spiller, E., Moller, T., Bostedt, C., Hoener, M., Shapiro, D. A., Hodgson, K. O., van der Spoel, D., Burmeister, F., Bergh, M., Caleman, C., Huldt, G., Seibert, M. M., Maia, F. R. N. C., Lee, R. W., Szoke, A., Timneanu, N., and Hajdu, J., Nature Phys., **2**, 839 (2006).

[2] Hahner, G., Chem. Soc. Rev., **35**, 1244 (2006).

[3] Lange, K. M. and Aziz, E. F., Chem. Soc. Rev., **42**, 6840 (2013).

[4] Stewart-Ornstein, J., Hitchcock, A. P., Hernández Cruz, D., Henklein, P., Overhage, J., Hilpert, K., Hale, J. D., and Hancock, R. E. W., J. Phys. Chem. B, **111**, 7691 (2007).

[5] Zubavichus, Y., Shaporenko, A., Grunze, M., and Zharnikov, M., J. Phys. Chem. B, **112**, 4478 (2008).

[6] Jahnke, T., Sann, H., Havermeier, T., Kreidi, K., Stuck, C., Meckel, M., Schoffler, M., Neumann, N., Wallauer, R., Voss, S., Czasch, A., Jagutzki, O., Malakzadeh, A., Afaneh, F., Weber, T., Schmidt-Bocking, H., and Dorner, R., Nature Phys., **6**, 139 (2010).

[7] Kaneko, F., Tanaka, M., Narita, S., Kitada, T., Matsui, T., Nakagawa, K., Agui, A., Fujii, K., and Yokoya, A., J. Electron Spectrosc. Relat. Phenom., **144**, 291 (2005).

[8] Ptasinska, S., Stypczynska, A., Nixon, T., Mason, N. J., Klyachko, D. V., and Sanche, L., J. Chem. Phys., **129**, 065102 (2008).

[9] Milosavljević, A. R., Canon, F., Nicolas, C., Miron, C., Nahon, L., and Giuliani, A., J. Phys. Chem. Lett., **3**, 1191 (2012).

[10] Martin, S., Ortega, C., Chen, L., Brédy, R., Vernier, A., Dugourd, P., Antoine, R., Bernard, J., Reitsma, González-Magaña, O., Hoekstra, R., and Schlathölter, T., Phys. Rev. A (submitted).

[11] González-Magaña, O., Reitsma, G., Tiemens, M., Boschman, L., Hoekstra, R., and Schlathölter, T., J. Phys. Chem. A, **116**, 10745 (2012).

[12] Bari, S., Hoekstra, R., and Schlathölter, T., Phys. Chem. Chem. Phys., **12**, 3360 (2010).

[13] González-Magaña, O., Reitsma, G., Bari, S., Hoekstra, R., and Schlathölter, T., Phys. Chem. Chem. Phys., **14**, 4351 (2012).

[14] Giuliani, A., Milosavljević, A. R., Hinsen, K., Canon, F., Nicolas, C., Réfrégiers, M., and Nahon, L., Angew. Chem. Int. Ed., **51**, 9552 (2012).

[15] Rose, I., Angew. Chem. Int. Ed., **44**, 5926 (2005).

[16] Ferguson, P. L. and Konermann, L., Anal. Chem., **80**, 4078 (2008).

[17] Purves, R., Barnett, D., Ells, B., and Guevremont, R., J. Am. Soc. Mass Spectrom., **11**, 738 (2000).

[18] Jiang, Y. H., Rudenko, A., Herrwerth, O., Foucar, L., Kurka, M., Kühnel, K. U., Lezius, M., Kling, M. F., van Tilborg, J., Belkacem, A., Ueda, K., Düsterer, S., Treusch, R., Schröter, C. D., Moshammer, R., and Ullrich, J., Phys. Rev. Lett., **105**, 263002 (2010).

[19] Jiang, Y. H., Pfeifer, T., Rudenko, A., Herrwerth, O., Foucar, L., Kurka, M., Kühnel K. U., Lezius, M., Kling, M. F., Liu, X., Ueda, K., Düsterer, S., Treusch, R., Schröter, C. D., Moshammer, R., and Ullrich, J., Phys. Rev. A, **82**, 041403 (2010).

[20] Yeh, J. J., *Atomic Calculation of Photoionization Cross-Sections and Asymmetry Parameters*, Gordon and Breach Science Publishers, Langhorne, PE (USA) (1993).

[21] Feng, R., Cooper, G., and Brion, C. E., J. El. Spectr. Rel. Phen., **123**, 199 (2002).

[22] Falick, A., Hines, W., Medzihradszky, K., Baldwin, M., and Gibson, B., J. Am. Soc. Mass Spectrom., **4**, 882 (1993).

[23] Papayannopoulos, I. A., Mass Spectrom. Rev., **14**, 49 (1995).

[24] Fenaille, F., Tabet, J.-C., and Guy, P. A., Rapid Commun. Mass Spectrom., **18**, 67 (2004).

[25] Svensson, S., J. Phys. B: At., Mol. Opt. Phys., **38** (2005).

[26] Gordon, M. L., Cooper, G., Morin, C., Araki, T., Turci, C. C., Kaznatcheev, K., and Hitchcock, A. P., J. Phys. Chem. A, **107**, 6144 (2003).

[27] Yumoto, H., Mimura, H., Koyama, T., Matsuyama, S., Tono, K., Togashi, T., Inubushi, Y., Sato, T., Tanaka, T., Kimura, T., Yokoyama, H., Kim, J., Sano, Y., Hachisu, Y., Yabashi, M., Ohashi, H., Ohmori, H., Ishikawa, T., and Yamauchi, K., Nature Photonics, **7**, 43 (2013).

[28] Zubarev, R., Nielsen, M., and Budnik, B., Eur. J. Mass Spectrom., **6**, 235 (2000).

Chapter 7

Summary

The response of complex biomolecules upon ionization by energetic photons and keV ions plays an important role in a number research fields, such as biological radiation damage, astrobiology or protein sequencing and structural analysis. In this context, cancer radiotherapy is undoubtedly of highest social relevance and at the same time of great complexity, comprising complementary knowledge from physics, chemistry, biology, and medicine. In contemporary radiotherapy, energetic photons (and electrons) are most often employed with the aim of eradicating tumors by killing the cancerous cells. More recently, the great potential of proton and heavy ion therapy led to an increased clinical activity also in this field.

To improve existing therapy lines, one of the main goals of fundamental research in the field is the understanding of the physical, chemical, and biological processes underlying the biological action of photon and particle beams in living cells. Although a general good understanding of the radiation induced dynamics of small biomolecular systems such as nucleobases and amino acids has been achieved over the last decade, this knowledge has not yet been transformed to molecular systems of true biological relevance, such as DNA or proteins. With the help of soft-ionizing techniques, such ESI, it has only very recently become possible to experimentally study radiation action on such molecules in the gas phase. A dream of the radiation damage community, namely the possibility to theoretically and experimentally study realistic biological systems such as DNA molecules and proteins at molecular levels of space and time is now within reach. In this thesis, a number of experimental steps towards the realization of this dream were presented.

The experiments were carried out with the tandem mass spectrometer Paultje, combining an electrospray ion source with a radiofrequency ion trap, for production and storage of gas-phase biomolecular ions, respectively. This apparatus was designed to reach the necessary amount of target density to perform mass spectroscopy studies of protonated gas-phase biomolecules upon ionizing radiation. By measuring the time-of-flight of the molecular fragments produced after ionizing radiation detailed information about the fragmentation process can be obtained. Furthermore, Paultje was designed to be flexible and portable. It can be interfaced with a wide range of ionizing radiation sources such as lasers, synchrotron facilities, free electron lasers and highly charged ion sources. Therefore, a wide variety of processes induced by all these mentioned sources can be studied and compared for any given biomolecular system.

In the pioneering experiment presented in chapter 3, ionization and fragmentation of doubly protonated oligonucleotides dGCAT upon interaction with keV C^{q+} ions, VUV photons and soft X-ray photons was studied. dGCAT contains the four nucleobases comprising the genetic code (guanine, cytosine, adenine, and thymine). As already stated in the introduction of this thesis, one of the most urging questions in the field today is, in how far is it possible to approximate photon and ion induced damage to DNA by the respective damage to DNA building blocks?

Remarkably, for keV ions and for energetic photons, mass spectra are always dominated by protonated and non-protonated nucleobases. Another prominent fragment with m/z 81 can be assigned to a fragmentation product of the deoxyribose group. The mass spectra thus confirm the prediction from earlier studies on gas-phase DNA building blocks, that the deoxyribose moiety is “the weakest link in tumour therapy" [N. Athey-Pollard, Chemical Biology, vol. **5**, (2006)][1], whereas nucleobases are comparably stable with respect to ionizing radiation. A careful extrapolation of data from isolated gas-phase DNA building blocks to radiobiologically more relevant systems seems therefore feasible.

A second question focused on the role of genuine chemical effects such as proton migration and charge migration in ionization and fragmentation of oligonucleotides. The experimental data proves that nucleobase protonation largely reflects the energetic ordering of the nucleobase proton affinities. The ratio between formation of protonated and non-protonated species depends strongly on ion velocity and photon energy. For the ion case, more energetic collisions seem to hinder proton migration towards guanine.

Last but not least, similarities and differences between ionization and fragmentation due to keV ions and due to energetic photons could be studied. In particular, absorption of VUV photons as well as interaction with keV ions predominantly involves ionization or excitation of molecular valence electrons and accordingly the observed fragmentation patterns exhibit qualitatively similar features. Soft X-ray absorption, on the other hand, induces ionization of core level electrons accompanied by subsequent emission of an Auger-electron and shifts the fragment distributions towards smaller masses.

The bulk of this thesis deals with photo-induced fragmentation dynamics of small peptides and proteins (chapter 4 to 6). Key aspects regarding molecular stability of peptides and proteins upon ionizing radiation are relevant for the field of biological radiation damage, because in the nuclei of living cells, DNA and proteins are closely intertwined. Also for the opposite perspective, the synthesis of life - for instance in extraterrestrial environments - peptide and protein stability upon irradiation is of utmost importance. Finally, the obtained data can be relevant for the field of mass spectrometry. Synchrotrons offer a wide range of photon energies, allowing to study fragmentation induced by molecular ionization from the highest occupied valence orbitals down to the core orbitals.

Earlier studies on protonated leucine enkephalin ($[YGGFL+H]^+$) had for instance indic-

---

[1] http://www.rsc.org/Publishing/Journals/cb/Volume/2006/5/Deoxyribose_tumour_therapy.asp

ated that charge migration and ultrafast fragmentation are the underlying processes leading to the formation of ions stemming from the sidechains of aromatic residues, which dominate the mass spectra[2]. Remarkably, this process seemed to be ultrafast, occurring before internal vibrational redistribution of the excitation energy within the molecule sets in on ps timescales. To gain deeper insight into this process, in chapter 4 VUV photofragmentation of protonated synthetic YG_nF peptides has been studied. Due to their low ionization potential, the two aromatic sidechains of the terminal amino acids (Y and F) are expected to act as the end points for charge migration from the peptide backbone. Determination of photoabsorption cross sections as a function of backbone length, i.e. the number $n = 0 - 10$ of sidechain-less G residues allows for a direct determination of the efficiency of hole migration. It was found that even though photoabsorption clearly occurs along the entire protonated peptide, for $n = 0 - 5$ the fragmentation patterns are dominated by ions from the (terminal) aromatic side chains, confirming the previously invoked fast charge migration towards these sidechains followed by ultrafast fragmentation. For $n = 10$ however, charge migration and/or fragmentation begins to get quenched and instead large dications and large singly charged fragments are observed. Based on the available data it was not possible to identify uniquely the exact mechanism of hole migration and its quenching for $n = 10$. Continuing studies, for instance based on pump–probe techniques with ultra short photon pulses such available at free electron laser facilities, are clearly needed.

A technique for the study of unoccupied molecular orbitals of intermediately sized and large gas-phase biomolecules has been introduced in chapter 5. Near-edge X-ray absorption mass spectrometry (NEXAMS) resembles well-established NEXAFS studies on condensed phase samples. The aim of chapter 5 was an investigation of the relative importance of non-dissociative processes as compared to fragmentation after soft X-ray absorption in smaller peptides. The previous experimental studies had indicated negligible fragmentation for the case of multiply charged proteins[3]. Remarkably, for $[YGGFL+H]^+$ and near C K-edge X-ray absorption the situation is clearly different. Here, non-dissociative processes are absent or weak and the fragmentation patterns are dominated by ions related to the sidechains of the amino acids. By recording the yields of photodissociation products as a function of the photon energy a NEXAMS spectrum is obtained. The obtained curves are very similar to NEXAFS spectra of peptides and proteins in the condensed phase. A comparison of gas-phase NEXAMS with available NEXAFS and XPS data on gas-phase amino acids allowed the identification of inner shell excitations and ionizations localized at different sites within the peptide. In particular, the two strong peaks at 285.40 eV and at 288.5 eV were assigned to localized and non-localized resonances in the residues. Most interestingly, a resonance at 284.4 eV which is solely due to C 1s $\rightarrow \pi^\star$ excitations in the aromatic rings leads mainly to formation of large fragments up to the intact protonated dication, and is thus apparently the

---

[2] S. Bari *et al.*, J. Chem. Phys., **134**, 024314 (2011).

[3] A. R. Milosavljević *et al.*, J. Phys. Chem. Lett., **3**, 1191 (2012).

softest X-ray absorption channel in the protonated molecule. Finally, C 1s ionization (above threshold) leads to very extensive fragmentation.

Chapter 6 is devoted to the question whether and if so why charge migration followed by fast sidechain loss is quenched in large proteins. To this end, multiphoton ionization of tenfold protonated ubiquitin cations was investigated using ultrashort intense XUV pulses from the free electron laser FLASH. Similar to all other peptide and protein related studies in this thesis, mainly fragmentation into immonium ions and related ions with relatively low m/z was observed. By reducing the FLASH beam intensity we were able to go from single/few photon absorption to multiphoton absorption within the protein. Under single and few photon absorption conditions, however, fragmentation was dominated by non-dissociative single and double ionization. With increasing pulse energy and thus with increasing number of photons, a linear increase of the partial immonium ion yields was observed. The most straightforward explanation for this increase is the “instantaneous" absorption of many photons, followed by fast and localized loss of an immonium ion, possibly through a repulsive molecular state. Essentially, this is the same process observed for single photon absorption in small peptides. The multiphoton ionization studies even prove the robustness of the process. The process clearly can occur in the presence of many additional photo-induced holes along the protein up to the limit where the number of absorbed photons becomes comparable to the number of residues in the protein. Apparently, a protein exposed to ultrashort intense XUV pulses can be viewed as an ensemble of small peptides and possibly even amino acids.

Samenvatting

De interactie tussen complexe biomoleculen en energetische fotonen of keV-ionen speelt een belangrijke rol in verschillende onderzoeksvelden zoals biologische stralingsschade, astrobiologie en radiotherapie. Onderzoek in de context van radiotherapie heeft de hoogste maatschappelijke relevantie. Het trekken van eenduidige conclusies vormt in onderzoek op gebied van biologisch stralingsschade een bijzondere uitdaging, mede omdat kennis van de fysica, chemie, biologie en geneeskunde gecombineerd moet worden. Conventionele radiotherapietechnieken maken gebruik van elektronen en röntgenstraling om tumoren op celniveau te bestrijden. Echter, het is reeds lang bekend, dat de dosisverdeling van protonen en zware ionen, zoals koolstofionen, zodanig is, dat zij de effectiviteit van radiotherapie significant zouden kunnen verhogen. Nauwkeurige bestudering van de interactie tussen complexe biomoleculen en protonen of zware ionen is daarom van cruciaal belang voor de verbetering van moderne radiotherapietechnieken gebaseerd op het gebruik van energetische deeltjes.

Één van de belangrijkste doelen van onderzoek in dit veld is het vergaren van informatie omtrent de fysische, chemisch en biologische processen die ten grondslag liggen aan de biologische respons van een levende cel op een fotonen- of ionenbundel. De laatste tien jaar heeft onderzoek naar kleine biologische bouwstenen, zoals nucleobasen en aminozuren, geweldige resultaten opgeleverd. Echter, de kennis over fundamentele processen in deze kleinste bouwsteenmoleculen kan nog niet vertaald worden naar systemen van daadwerkelijke biologische relevantie. Recent heeft de electrospray-ionisatietechniek het mogelijk gemaakt grote biologisch relevante systemen, zoals DNA en eiwitten, in de gasfase te bestuderen. Daardoor is de droom, het zowel theoretisch als experimenteel bestuderen van realistische biologische systemen op het niveau van een enkel molecuul binnen handbereik gekomen. In dit proefschrift worden enkele belangrijke experimentele stappen in de richting van de realisatie van deze droom gepresenteerd.

De experimenten zijn uitgevoerd met een zelfontwikkelde opstelling voor massaspectrometrische analyse met daarin geïntegreerd een electrospray-ionisatiebron en een elektromagnetische val voor de te bestuderen molecuulionen. Electrospray-ionisatie is een methode om grote biomoleculeculaire ionen in de gasfase te brengen zonder dat deze uit elkaar vallen.

De elektromagnetische val wordt gebruikt om moleculen te verzamelen zodat de dichtheid van moleculen hoog genoeg is om een bestralingsexperiment te doen. Nadat het wolkje moleculen bestraald is, wordt de inhoud van de val geanalyseerd met behulp van vluchttijdspectrometrie. De opstelling is zodanig ontworpen dat verschillende soorten straling, zoals ionen (KVI-RuG), synchrotronstraling (BESSY-II, MaxLab) en licht van een vrije-elektronenlaser (FLASH), kunnen worden gebruikt. Met behulp van deze verschillende stralingsbronnen kan een breed scala aan biomoleculaire processen worden geïnduceerd en met elkaar vergeleken.

In hoofdstuk drie wordt een experiment beschreven waarin dubbel geprotoneerde oligonucleotiden dGCAT worden bestraald met keV-koolstofionen, VUV-fotonen en zachteröntgenstraling. dGCAT bevat vier nucleobasen, namelijk guanine, cytocine, adenine en thymine. Een van de meest fundamentele vragen in de context van radiotherapie is: “In hoeverre is het mogelijk stralingsschade aan DNA te relateren aan schade aan de individuele bouwstenen (nucleobasen)?"

De fragmentatiemassaspectra van dGCAT zoals gemeten na bestraling met keV-ionen en energetische fotonen worden altijd gedomineerd door geprotoneerde en niet-geprotoneerde nucleobasen. Een ander fragment dat veel voorkomt is een fragmentatieproduct van de suikergroep in dGCAT. De massaspectra bevestigen dus voorspellingen gebaseerd op eerdere studies aan gasfase DNA-bouwstenen. De suikergroep is een zwakke zo niet de zwakste schakel, terwijl nucleobasen relatief stabiel zijn. De eerdere extrapolatie op basis van alleen nog maar gegevens van individule nucleobasen en suikermoleculen naar biologische relevante systemen lijkt daarom nog steeds gerechtvaardigd.

Een tweede belangrijke vraag omvat de rol van chemische effecten, zoals protonmigratie en ladingsmigratie tijdens de fragmentatie van oligonucleotiden. De experimentele gegevens laten zien dat de protonering van de verschillende nucleobasen hand-in-hand gaat met de protonenaffiniteit van deze nucleobasen. De verhouding tussen geprotoneerde en niet-geprotoneerde fragmenten hangt sterk af van de snelheid van de ionen of de energie van de fotonen. In het geval van ionen lijkt protonenmigratie naar guanine sterk te verminderen met toename van de energie van de ionen.

De experimentele data geven ook inzicht in de verschillen tussen ionisatie en fragmentatie door ionen enerzijds en fotonen anderzijds. Absorptie van een VUV-foton en interactie met keV ionen betreft voornamelijk ionisatie en excitatie van valentie-elektronen. Daarom vinden we kwalitatief vergelijkbare massaspectra. Echter, absorptie van een zachteröntgenfoton gebeurt voornamelijk door binnenschillenelektronen. Het ontstaan van een elektronisch gat in een binnenschil wordt gevolgd door een zogenoemd Auger-verval, waarbij nog een elektron wordt geëmitteerd. Daardoor wordt gemiddeld meer energie in het molecuul gestopt en zien we een verschuiving van het massaspectrum in de richting van de lagere massa’s, m.a.w. een sterkere fragmentatie.

Het grootste deel van dit proefschrift (hoofstukken 4 tot en met 6) is gewijd aan de ultrasnelle fragmentatiedynamica van kleine peptiden en eiwitten. Aspecten als moleculaire stabiliteit van peptiden en eiwitten na bestraling met fotonen zijn van belang in het kader van biologische stralingsschade omdat in kernen van levende cellen DNA en proteïnen nauw met elkaar zijn verweven. Ook in de context van de mogelijkheid van het ontstaan van leven vanuit en in de ruimte is de stabiliteit van peptiden en eiwitten van cruciaal belang.

Uit eerder werk aan geprotoneerd leucine-enkephaline weten we dat ladingsmigratie ten grondslag ligt aan de vorming van ionen die afkomstig zijn van aromatische zijketens van het molecuul. Deze zijketens domineren de massaspectra. Opvallend is dat deze ladingsmigratie ultrasnel is, dat wil zeggen dat het gebeurd voordat de excitatie-energie via intravibrationele relaxatie over het molecuul wordt uitgesmeerd. Om meer inzicht te verkrijgen in dit ultrasnelle proces van ladingsmigratie hebben we de VUV-fragmentatie van synthetische petiden van de vorm YGnF bestudeerd. Omdat de twee aromatische zijketens (Y en F) een lage ionisatiepotentiaal hebben, kunnen zij worden gezien als de eindpunten voor de ladingsmigratie langs de ruggegraat van de peptide. Door nu de lengte van de ruggegraat - het aantal G-aminozuren - te variëren van 1 tot 10 kan de efficiëntie van de ladingsmigratie bepaald worden. Voor n=0-5 vertoont de fragmentatie vergelijkbaar gedrag met het eerdere werk aan leucine-enkephaline: ultrasnelle ladingsmigratie naar de zijketens gevolgd door supersnelle fragmentatie. Dit resulteert in massaspectra die worden gedomineerd door geïoniseerde zijketen fragmenten. Echter, de massaspectra voor de langste peptide (n=10) laten een ander patroon zien: grote dubbelgeladen ionen en enkelvoudig geladen fragmenten. Dit betekent dat de ladingsmigratie hoe ultrasnel ook grotendeels is uitgedoofd voordat de eindketens worden bereikt. Een precieze bepaling van de migratiesnelheden en daaropvolgende processen is verder onderzoek met behulp van een vrije-elektronenröntgenlaser noodzakelijk.

In hoofdstuk 5 wordt een nieuwe techniek - NEXAMS - geïntroduceerd die onderzoek aan niet-bezette moleculaire orbitalen in grote gasfase biomoleculen mogelijk maakt. Hierdoor wordt de bestudering van niet-dissociatieve processen in vergelijking tot fragmentatie na bestraling met zachte röntgens mogelijk. Uit eerdere experimentele studies bleek fragmentatie verwaarloosbaar te zijn voor meervoudig geladen eiwitten. Het is daarom opvallend dat [YGGFL+H]+ na absorptie in de K-schil een heel ander gedrag vertoont. Hier komen juist bijna geen niet-dissociatieve processen voor en zien we veel fragmenten die te relateren zijn aan de aminozuurzijketens. Door de fragmentenopbrengst te meten als functie van de fotonenenergie zijn zogenoemde NEXAMS-spectra verkregen. Voor het onderhavige systeem zijn twee sterke pieken zichtbaar in de spectra die kunnen worden toegewezen aan gelokaliseerde en niet-gelokaliseerde resonanties in de residuën, waarvan de eersteafkomstig is van een elektronische aanslag in de aromatische ringen van het molecuul en leidt tot vorming van grote fragmenten en ook intacte ionen. Tenslotte leidt absorptie boven de koolstof-K-kant tot erg uitgebreide fragmentatiepatronen.

Hoofdstuk 6 is gewijd aan de vraag in hoeverre ladingsmigratie wordt verhinderd in grote proteïnen. Hiervoor is voor het eerst gebruik gemaakt van de ultrakorte en extreem intense XUV-pulsjes van de vrije-elektronenlaser FLASH in Hamburg. Specifiek hebben we gekeken naar de multifotonenionisatie van tienvoudig geprotoneerd ubiquitine. Vergelijkbaar met de meeste van de andere experimenten in dit proefschrift zien we veelal fragmentatie in kleine fragmenten. Door de bundelintensiteit van FLASH te variëren was het mogelijk om de transitie te maken van enkelvoudige fotonenabsorptie naar multifotonenabsorptie. Bij lage intensiteit, enkelvoudige fotonenabsorptie, wordt het spectrum gedomineerd door niet-dissociatieve enkelvoudige en dubbele ionisatie. Als het aantal geabsorbeerde fotonen wordt opgevoerd nemen we een lineaire toename van het aantal (kleine) immoniumionen waar. De meest voor-de-handliggende verklaring hiervoor is dat de gelijktijdige absorptie van meerdere fotonen leidt tot een gelokaliseerd verlies van een immoniumion, mogelijk via een dissociatieve moleculaire toestand. In essentie is dit hetzelfde ultrasnelle proces wat we ook zien in onze studies aan kleinere peptiden. Echter, deze FEL-experimenten bevestigen de robuustheid van dit proces. Namelijk, het proces kan zelfs plaatsvinden in de aanwezigheid van meerdere fotogeïnduceerde elektronische gaten in de proteïne, en wel totdat het aantal geabsorbeerde fotonen gelijk is aan het aantal beschikbare residuën. Klaarblijkelijk kan een proteïne dat wordt bestraald worden gezien als een verzameling van kleine peptiden en mogelijk zelfs aminozuren.

Resumen

La forma en que las biomoléculas responden a la ionización es primordial en el estudio de varias disciplinas. Por ejemplo, en el estudio del daño biológico producido por radiación ionizante, en la astrobiología o en el secuenciamiento y análisis estructural de las proteínas. Los procesos de ionización generados por fotones de onda corta o por iones con energías de varios keV interesan principalmente. En este contexto el estudio de métodos de radioterapia para combatir el cáncer es de gran relevancia para la sociedad. Aunque a su vez presenta un complicado reto, ya que requiere de la interacción y la aplicación de conocimientos de física, química, biología y medicina. La mayoría de las radioterapias existentes utilizan fotones de onda corta o electrones con el fin de matar las células cancerígenas y erradicar tumores. Recientemente se han incrementado el uso de radioterapias basadas en protones e iones pesados debido a su gran potencial clínico y sus pocos efectos secundarios.

En vista de mejorar la infraestructura actual para radioterapias, la investigación básica realizada en esta disciplina tiene como uno de sus principales objetivos el entender la acción biológica de haces de fotones y de iones en células vivas a partir de los procesos físicos, químicos y biológicos. Aunque durante las últimas décadas se ha alcanzado un adecuado conocimiento sobre la dinámica de la radiación inducida en pequeños sistemas biomoleculares, como las bases nitrogenadas y los aminoácidos, este conocimiento no se ha logrado aún en sistemas moleculares como el ADN o las proteínas. Recientemente ha sido posible experimentar con este tipo de biomoleculas aisladas en el estado gaseoso, utilizando técnicas de ionización suaves como la ionización por electrodispersión ESI (Electrospray Ionization).

Parte importante en el estudio de daño biológico por radiación son los experimentos y estudios teóricos de sistemas biológicos realistas, como moléculas de ADN y proteínas. En esta tesis se presentan experimentos diseñados para avanzar en su realización.

En el capítulo 2 se describe el dispositivo experimental llamado Paultje, cuyo nombre en español se traduce como *Pablito*. Este dispositivo consiste en un espectrómetro de masas en tándem, el cual combina una fuente de producción de iones con una trampa de radio frecuencia para iones. Los iones son producidos en la fuente por medio de la técnica de ionización por electrodispersión (ESI) mientras que la trampa de radio frecuencia sirve para colectar los iones. El diseño de este aparato experimental permite alcanzar la densidad de iones requerida para realizar espectroscopia de masas de biomoléculas protonadas en el estado gaseoso y sometidas a radiación ionizante. La información detallada acerca del proceso de fragmentación se obtiene midiendo el tiempo de vuelo de los fragmentos de la molécula que son producidos por la radiación ionizante. El dispositivo Paultje se construyó además para permitir el estudio del mismo sistema molecular bajo la accíon de una gran variedad de fuentes de radiación ionizante. Su diseño es transportable y flexible, y el dispositivo ha sido instalado en una gran variedad de fuentes de radiación ionizante tales como láseres, instalaciones de luz sincrotrón, láseres de electrones libres (Free Electron Laser) y fuentes de iones altamente ionizados (ECRIS).

En el capítulo 3 se presenta un experimento pionero sobre la ionización y fragmentación del oligonucleótido dGCAT doblemente protonado bajo la interacción de iones C^{q+} de energías en el orden de keV y de fotones de onda corta (VUV y rayos X suaves). Una de las cuestiones a responder es hasta donde es posible evaluar el daño producido por iones y fotones altamente energéticos sobre el ADN utilizando solo los resultados obtenidos para las moléculas que lo conforman, i.e. usando los resultados en bases nitrogenadas aisladas o en pequeños oligonucleótidos.

Todos los espectros de masas para iones (keV) y fotones de onda corta presentados en el capítulo 3 son dominados por la señal debida a nucleobases protonadas y no protonadas. Otro fragmento dominante en los espectros tiene una relación masa-carga m/z 81 y puede atribuirse a un subproducto de la fragmentación de la desoxirribosa (el azúcar en el ADN). Con estos espectros de masas se confirma la predicción formulada en estudios previos en componentes del ADN en estado gaseoso. Según la cual la desoxirribosa es “el eslabón más débil en terapias de tumores"[N. Athey-Pollard, Chemical Biology, vol. **5**, (2006)][4], mientras que las bases nitrogenadas son en comparación más estables a la radiación ionizante. Esto hace más plausible una extrapolación cuidadosa de datos provenientes de los componentes que conforman el ADN en estado gaseoso hacia sistemas radiobiológicos más complejos y biológicamente relevantes.

Una segunda cuestión estuvo enfocada en la migración de carga (huecos de electrón) y de protones debida a la ionización y fragmentación de oligonucleotidos. En los resultados experimentales se observa que el estado de protonación de las bases nitrogenadas esta ordenado energéticamente a partir de las afinidades electrónicas de las bases nitrogenadas. La razón entre la formación de especies protonadas y no protonadas depende fuertemente de la velocidad del ion o de la energía del fotón incidentes.

Por último, es posible estudiar las similitudes y diferencias entre la ionización y la fragmentación debida a iones y a fotones. Estos procesos involucran principalmente la excitación

---

[4] http://www.rsc.org/Publishing/Journals/cb/Volume/2006/5/Deoxyribose_tumour_therapy.asp

o ionización de electrones en la banda de valencia molecular y como consecuencia los espectros de masas presentan cualitativamente un patrón de fragmentación similar. Por otro lado, la absorción de rayos X suaves induce ionización de los electrones localizados en los niveles internos que es acompañada por la subsecuente emisión de un electrón Auger, y que desplaza la distribución del espectro hacia los valores m/z más pequeños.

La mayor parte de esta tesis (capítulos 4 a 6) estudia la dinámica de la fragmentación inducida por fotones de onda corta en péptidos pequeños y en proteínas. La estabilidad molecular de péptidos y proteínas sometidas a radiación ionizante es un aspecto clave en la disciplina de daño biológico por radiación. Esto debido a que el ADN y las proteínas están fuertemente interconectados dentro del núcleo de las células vivas. Desde la perspectiva de la síntesis de vida en ambientes extraterrestres, por ejemplo, la estabilidad de péptidos y proteínas sometidas a radiación ionizante es de suma importancia. Finalmente, los datos que se presentan pueden ser relevantes para la disciplina de espectrometría de masas. Los sincrotrones producen fotones en un amplio rango de energía, lo que permite estudiar la fragmentación molecular inducida por ionización empezando desde los últimos orbitales de valencia ocupados y hasta los orbitales más internos.

En estudios previos con el oligopéptido protonado leucina-encefalina ($[\mathrm{YGGFL+H}]^+$) se ha observado que los procesos fundamentales para la formación de iones provenientes de las cadenas aromáticas de los aminoácidos son la migración ultra rápida de carga quel sucede en femtosegundos, y su posterior fragmentación. La fragmentacion parece ocurrir antes de que la energía de excitación pueda redistribuirse en los modos internos vibracionales de la molecula, lo cual típicamente ocurre en picosegundos. Para observar más detenidamente este proceso, en el capítulo 4 se presenta un estudio sobre la fotofragmentación de péptidos protonados sintéticos $\mathrm{YG}_n\mathrm{F}$.

Los potenciales de ionización de las cadenas laterales (sidechain) de los aminoácidos Y y F son pequeños por lo cual se espera que estas dos cadenas laterales actúen como puntos finales para la migración de carga en la cadena peptídica. La determinación de las secciones eficaces de fotoabsorción como función de la longitud de la cadena peptídica, es decir del número de cadenas laterales del aminoácido G ($n = 0 - 10$), permite una determinación directa de la eficiencia de la migración de huecos de electrón. En el caso de $n = 0 - 5$ se encontró que los patrones de fragmentación son dominados por iones de las cadenas laterales de los aminoácidos (especialmente de los que están en los extremos) y que esto sucede a pesar de que la fotoabsorción puede ocurrir a lo largo de todo el péptido protonado. Esto confirma la idea previa de una rápida migración de carga hacia estas cadenas laterales seguida por fragmentación ultra rápida. Sin embargo en el caso de $n = 10$ la migración de carga y/o la fragmentación empiezan a ser suprimidas y en su lugar se forman grandes fragmentos iónicos positivos de una o dos cargas. Los resultados obtenidos no permiten identificar inequívocamente los mecanismos exactos de la migración de huecos y de la subsecuente supresión en el caso $n = 10$. Para esto son necesarios nuevos estudios de espectroscopia de resolución de tiempo basados en técnicas “pump-probe” que utilizan pulsos ultra cortos de fotones disponibles en laboratorios con láseres de electrones libres como FLASH.

En el capítulo 5 se introduce una técnica para el estudio de orbitales moleculares desocupados de biomoléculas de tamaño intermedio a grande y en estado gaseoso. Esta técnica, conocida como NEXAMS (*Near-Edge X-ray Absorption Mass Spectrometry*), se asemeja a la bien establecida técnica NEXAFS utilizada en muestras en fase condensada. El objetivo de este capítulo fue investigar la importancia de los procesos no disociativos en comparación con la fragmentación en pequeños péptidos debida a la absorción de rayos X suaves. Estudios experimentales previos encontraron una fragmentación despreciable en el caso de proteínas multiplemente cargadas [5]. La situación es diferente para la absorción de rayos X en $[\mathrm{YGGFL+H}]^+$ en el rango de energías de la capa K del carbono. Aquí los procesos no disociativos están ausentes o son débiles y los patrones de fragmentación son dominados por iones relacionados con las cadenas laterales de los aminoácidos. Cada espectro NEXAMS fue obtenido al graficar los rendimientos de producción de iones por fotodisociación en función de la energía de los fotones incidentes. La curva que se obtiene es muy similar a los espectros NEXAFS de péptidos y proteínas en fase condensada. Es posible identificar excitaciones e ionizaciones en las capas atómicas internas localizadas en diferentes partes dentro del péptido comparando los resultados del espectro NEXAMS con espectros NEXAFS y XPS para aminoácidos en estado gaseoso. En particular los dos picos más intensos con energías 285.40 y 288.5 eV han sido atribuidos a resonancias localizadas y no localizadas en los residuos de los aminoácidos. La resonancia a 284.4 eV, debida solamente a excitaciones C 1s $\rightarrow \pi\star$ en los anillos aromáticos, provoca principalmente la formación de fragmentos de gran tamaño o aún de un catión intacto de la molécula protonada. Esta resonancia es aparentemente el canal menos disociativo para la absorción de rayos X en la molécula.

En el capítulo 6 se estudia si la migración de carga producida en proteínas es responsable de la rápida pérdida de sus cadenas laterales y además el por qué esta pérdida es suprimida en el caso de proteínas de gran tamaño. Para ello se realizo un experimento en el laser de electrones libres FLASH localizado en la ciudad de Hamburgo, Alemania. De una manera similar a los péptidos y proteínas estudiadas en esta tesis, se observaron principalmente fragmentos con valores m/z relativamente pequeños que corresponden a iones “immoniu’m’y a sus fragmentos. Los iones “immonium” son fragmentos de aminoacidos formados por solo una cadena lateral.

Al cambiar la intensidad del haz de fotones en FLASH fue posible estudiar la absorción simultanea en la proteína desde uno y hasta un “gran” número de fotones. En el caso de la absorción simultanea de un fotón (o unos pocos de ellos) el espectro de fragmentación fue dominado por ionizaciones simples y dobles, ambas no disociativas . Al incrementar la energía del pulso y por ende el número de fotones, se encontró un incremento lineal de los rendimientos de producción del ion “immonium". La explicación más directa para describir

---

[5] A. R. Milosavljević *et al.*, J. Phys. Chem. Lett., **3**, 1191 (2012).

este incremento es la absorción “instantánea"de muchos fotones, seguida por una rápida y localizada pérdida de un ion “immonium", posiblemente a través de un estado molecular repulsivo. Este mismo proceso es observado en la absorción de un fotón en pequeños péptidos. Los estudios de ionización por múltiples fotones muestran la robustez de este proceso. Este proceso puede ocurrir en la presencia de muchos huecos (de electrón) adicionales inducidos por fotones a lo largo de la proteína y hasta el límite donde el número de fotones absorbidos se hace comparable al número de residuos en la proteína. Así, una proteína expuesta a pulsos XUV ultra cortos puede ser vista como un conjunto de pequeños péptidos y posiblemente de aminoácidos.

Esta tesis contribuye al entendimiento del daño biológico por radiación al presentar estudios un poco más realistas de sistemas biomoleculares en fase gaseosa. Se estudio la dinámica de fragmentación debida a fotones de onda corta y iones de energias de keV en pequeñas proteínas y componentes de ADN y se encontró que la fragmentación depende de la cantidad de energía depositada en la molécula y de su conformación. Un estudio detallado de este proceso mostró que la fragmentacion en el caso de péptidos pequeños está dominada por una pérdida ultra rápida de iones de cadenas laterales de los aminoacidos y que esta pérdida disminuye en péptidos más largos. Nuevos estudios son necesarios para entender este proceso.

Acknowledgments

I would like to thank everyone who help me throughout my PhD.

First of all, I will always be grateful to my supervisor Thomas Schlathölter for all his help and support. Thank you for giving me the opportunity to participate in so many great experiments, for your patience when answering my questions, and for teaching me how to do (and how not to do) experimental physics. Also, thank you for sharing your always enthusiastic approach to solve all kind of technical and scientific problems.

Furthermore, I would like to thank Ronnie Hoekstra for giving me the opportunity to join the atomic and molecular physics group, and for supporting my academic activities during my PhD. Thank you for the painstaking reading of my manuscript. Finally, thank you for organizing the unique dutch-type barbecues.

I wish to acknowledge my fellow (ex)colleagues of the atomic and molecular physics group for their help: Thank you Corine Meinema, Dorine de Jong, Dmitrii Egorov, Erwin Bodewits, Geert Reitsma, Hồng Đặng, Ina Blank, Jos Postma, Leon Boschman, Marcel Tiemens, Mart Johan Deuzeman, Meike Door, and Sadia Bari. In addition, I would like to thank Geert for translating my Samenvatting and Sadia for patiently teaching me all the details of Paultje.

I would like to thank the members of my reading committee for carefully reading the manuscript and providing me with useful comments and corrections.

I wish to express my gratitude to all the people at the KVI. In particular to Hilde van de Meer for helping me trough all the paperwork and for patiently answering all my questions. To Miranda, Carla and Robert from the financial department for helping me with complex travel declarations and shopping forms. To Marjan Koopmans for organizing the FANTOM schools and for helping me with all kind of academic issues. Also, I would like to thank Harry Kiewiet and Jan Mulder for helping me with the setup alignment. In addition, this work was only possible with the help of the members of the mechanic, the electronic, and the vacuum departments. Bedankt. Last but not least, I wish to thank all my fellow KVI PhD students, and wish them all the best in their careers.

In the course of my PhD I had the possibility to collaborate with several international research groups.

- Michael Huels, Richard J. Wagner, Pierre Lahaie, and Maxim Tchaplyguine: thank you for your help during the MAXLab beamtimes. In particular, I wish to thank Michael for encouraging me to cook a dinner for the team, even if my cooking skills are limited to microwave techniques. And thank you for cooking the best beamtime-food ever.
- Ana García, Martina Fuss, and Gustavo García: thank you for your warm hospitality throughout my visit to your laboratory in Madrid. Muchas gracias.
- Serge Martin, Richard Brédy, Arnaud Vernier, Philippe Dugourd, Rodolphe Antoine: thank you for the collaboration on the cytochrome C experiment at the KVI. Merci beaucoup.
- Edgar Hernández, Alex Aguilar, Antonio Juárez, Alejandro Morales, Armando Antillón, David Macaluso, Dag Hanstorp, and Guillermo Hinojosa: thank you for your invitation to participate in a beamtime at the ALS.
- Roland Wester, Thorsten Best, Rico Otto, Alexander von Zastrow, Sebastien Jézouin, Jonathan Brox, and Martin Stei: thank you for the collaboration on the water cluster experiment at the KVI.
- Robert Moshammer, Bettina Fischer, and Nicolas Camus: thank you for all your help during the fs-laser experiment at the MPIK Heidelberg.
- Gerd Reichardt, Peter Baumgärtel, Helmut Pfau, and Antje Vollmer from BESSY: thank you for all your help throughout several beamtimes. Dankeschön.
- Kirsten Schnorr, Claus Dieter Schröter, and Robert Moshammer: thank you for all your help during the beamtime at FLASH .

Thanks to my paranimf Sofia and her husband Thomas for the beautiful time that we shared in Groningen. Thank you for your friendship, and for teaching me how to repair, paint, and (un-)furnish a new apartment. Success.

I wish to thank all my friends for their support. Rut, Mayerlin, Nelly, Claudia, Oscar, Olmo, Enrique, Hugo, Marta, and Emiliano.

I am very grateful to Remigio Cabrera, Luz Díaz, and Leonardo for all your support over the last years, and for sharing your time and expertise with me. Thank your for all your advice over academic and personal questions. Muchas gracias.

A special place is reserved to Guillermo Hinojosa and his beautiful family: Gabriela, Laura, Eduardo and Mariana. Thank you for all your support over the years, for teaching me experimental physics and trusting in me. I wish all of you all the best. Muchas gracias.

Finally, thank you with all of my heart to my family, who has always supporting me.

List of publications

This thesis

(Chapter 3)

1. *Fragmentation of protonated oligonucleotides by energetic photons C^{q+} ions*
   Olmo González-Magaña, Marcel Tiemens, Geert Reitsma, Leon Boschman, Meike Door, Sadia Bari, Pierre Olivier Lahaie, Richard J. Wagner, Michael A. Huels, Ronnie Hoekstra, and Thomas Schlathölter.
   Phys. Rev. A, **87**, 032702 (2013)

(Chapter 4)

2. *Length effects in VUV photofragmentation of protonated peptides*
   Olmo González-Magaña, Geert Reitsma, Sadia Bari, Ronnie Hoekstra, and Thomas Schlathölter.
   Phys. Chem. Chem. Phys., **14**, 4351 (2012)

(Chapter 5)

3. *Near-Edge X-ray Absorption Mass Spectrometry of a Gas-Phase Peptide*
   Olmo González-Magaña, Geert Reitsma, Marcel Tiemens, Leon Boschman, Ronnie Hoekstra, and Thomas Schlathölter.
   J. Phys. Chem. A, **116**, 10745 (2012).

(Chapter 6)

4. *Ionization and stability of a small protein in ultrashort XUV free electron laser pulses*
   Olmo González-Magaña, Geert Reitsma,Sadia Bari, Leon Boschman, Erwin Bodewits, Kirsten Schnorr, Claus Dieter Schröter, Robert Moshammer, Ronnie Hoekstra, and Thomas Schlathölter
   In preparation

5. *Hydrogenation of PAH cations: a first step toward H_2 formation*
   L. Boschman, G. Reitsma, S. Cazaux, T. Schlathölter, R. Hoekstra, M. Spaans, and O. González-Magaña
   ApJL, **761**, L33 (2012)

6. *Dissociation of a free protonated peptide by VUV photons*
   S. Bari, O. González-Magaña, G. Reitsma, J. Werner, S. Schippers, R. Hoekstra, and T. Schlathölter.
   J. Chem. Phys., **134**, 024314 (2011)

7. *Multi electron capture and deprotonation processes observed in Xe^{8+} - Cytochrome C^{q+} (q=15-19) collisions*
   S. Martin, C. Ortega, L. Chen, R. Brédy, A. Vernier, P. Dugourd, R. Antoine, J. Bernard, O. González-Magaña, M. Tiemens, G. Reitsma, R. Hoekstra, and T. Schlathölter.
   submitted to Phys. Rev. A

8. *Cross-sections for energetic heavy-ion impact on protonated water clusters.*
   A. von Zastrow, R. Otto, S. Jezouin, J. Brox, M. Stei, O. González-Magaña, G. Reitsma, T. Schlathölter, R. Hoekstra, T. Best, and R. Wester
   accepted in Applied Physics B

9. *Photoionization cross sections for Cl II in the photon energy range of 19.5 eV to 28 eV*
   E. Hernández, A. M. Júarez, A. Aguilar, O. González-Magaña, A. Antillón, A. Morales-Mori, D. Hanstorp, D. Macaluso, and G. Hinojosa.
   to be submitted to Astronomy & Astrophysics